MAGNETIC RESONANCE IMAGING OF SHORT T_2 MATERIALS:

FROM DETECTION TO QUANTIFICATION

by

LUNING WANG

(Under the Direction of Qun Zhao)

ABSTRACT

Magnetic resonance imaging (MRI) is a cutting-edge imaging technique that has been widely and successfully used in clinical diagnoses and biological researches. However, challenges usually arise when using conventional MRI pulse sequences to image short T_2 tissues or materials, such as cortical bone, teeth, tendon, iron oxide nanoparticles, and etc., since these materials are associated with fast-decaying MR signals. Meanwhile, there exists an enormous demand to overcome these challenges to improve detection and quantification of short T_2 materials. For example, improvement of detection specificity of cells labeled by iron oxide nanoparticles is crucial for researchers to in vivo track cells and to understand the behaviors of cells. Another example is that quantification of water components in cortical bone is of critical importance to understand and diagnose bone diseases, such as osteoporosis. The objectives of this dissertation are to propose novel approaches of MRI to qualitatively and quantitatively study the short T_2 materials, with main focus placed on iron oxide nanoparticles and cortical bone.

INDEX WORDS: Magnetic Resonance Imaging, Iron Oxide Nanoparticles, Cortical Bone, SWIFT Sequence, Long T_2 Suppression, T_1 Mapping, Phase Gradient, Susceptibility.

MAGNETIC RESONANCE IMAGING OF SHORT T_2 MATERIALS: FROM DETECTION TO QUANTIFICATION

by

LUNING WANG

B.S., Zhengzhou University, Zhengzhou, China, 2008

A Dissertation Submitted to the Graduate Faculty of The University of Georgia in Partial Fulfillment of the Requirements for the Degree

DOCTOR OF PHILOSPHY

ATHENS, GEORGIA

2013

MAGNETIC RESONANCE IMAGING OF SHORT T_2 MATERIALS:

FROM DETECTION TO QUANTIFICATION

by

LUNING WANG

Major Professor: Qun Zhao

Committee: William Dennis

James Prestegard

Electronic Version Approved:

Maureen Grasso
Dean of the Graduate School
The University of Georgia
December 2013

DEDICATION

Dedicated to my parents, Kefei Wang and Hualing Lu, for their endless love and support.

ACKNOWLEDGEMENTS

I would like to thank my academic advisor, Dr. Qun Zhao, for his guidance and support throughout my graduate study, and to express my gratitude to my committee members, Dr. William Dennis and Dr. James Prestegard, for their help and advices on my dissertation. I also want to thank Dr. Michael Garwood, Dr. Curtis Corum, and Dr. Djaudat Idiyatullin from the University of Minnesota for their help on the SWIFT sequence, and thank my colleagues in our MRI lab, Dr. Jason Langley, Dr. William Potter, Dr. Joonsang Lee, and Ms. Qingying Meng for their helpful discussions on MRI. Finally, I want to thank the Department of Physics and Astronomy at the University of Georgia.

TABLE OF CONTENTS

Page

LIST OF TABLES

Page

LIST OF FIGURES

Page

CHAPTER 1

INTRODUCTION AND LITERATURE REVIEW

1.1 Brief history

Magnetic resonance imaging (MRI) is a cutting-edge, noninvasive imaging technology that has been widely implemented in clinical diagnoses and biological research. The development of MRI is also the development of our knowledge of small atoms that contribute to MR signals and the quantum theory that describes behaviors of these small atoms.

Two German scientists, O. Stern and W. Gerlach, had first designed an experiment, the Stern-Gerlach experiment, to study the angular momentum of the silver atom in 1922. They had shown that both the intrinsic angular and magnetic momentums of silver were quantized (1). In 1929, the American scientist, Isidor Rabi, studied atoms, including hydrogen and deuterium, by improving the Stern-Gerlach experiment to further precision (2). His experiment indicated that the magnetic moments of the atoms would align either parallel or anti-parallel to the external, static magnetic field, which could be described and derived using the Schrodinger equation and Boltzmann distribution. In 1937, Isidor Rabi theoretically predicted that the magnetic moment of a nucleus could be excited by absorption of an electromagnetic wave at the resonant frequency characterized by the gyromagnetic ratio. And in 1938, he observed such a phenomenon using lithium chloride molecules (3). In 1946, two scientists, Felix Bloch and Edward Purcell, discovered the nuclear magnetic resonance phenomena separately, which could be described by an empirical equation, the Bloch equation (4,5). In 1973, the door of MRI was opened by Paul

Lauterbur and Peter Mansfield, who proposed their ideas in seminal papers that if the external magnetic field is spatially varying, the Larmor frequencies also become spatially varying. In 1975, Richard Ernst proposed a reconstruction method of MR images using Fourier transformation. In 1977, the first MR images of a living human were acquired and published (6). Since then, MRI has been increasingly applied in research and clinical practices.

1.2 Background of MRI and short T_2 materials

Magnetic resonance phenomenon requires existence of spin half materials, such as ^{1}H, ^{23}Na, ^{31}P, etc. MRI focuses on protons from water, tissues, lipid, organs, and etc. Based on the classic view in physics, the MRI scanner provides a main magnetic field, B_0, in the scale of a few Tesla, and the protons align with the main magnetic field either parallel or anti-parallel, resulting in a net magnetization. When applying a radio-frequency (RF) electromagnetic pulse perpendicular to the main magnetic field, the frequency of which matches the Larmor frequency of protons, the protons, as vectors, will start to process about the applied RF pulse in the Larmor frequency. Therefore, the RF pulse generates magnetization perpendicular to the main magnetic field, or the so-called transverse magnetization. The behavior of the net magnetization can be described by the Bloch equation:

$$\frac{d\vec{M}}{dt} = \vec{M} \times \gamma\vec{B} - \frac{\vec{M}_{xy}}{T_2} - \frac{M_z - M_0}{T_1}\hat{z} \qquad [1.1]$$

In Equation 1.1, M is the net magnetization, γ is the gyromagnetic ratio of the proton, B is the external magnetic field, M_{xy} is the transverse magnetization, M_z is the z-component of the net magnetization, also referred to as longitudinal magnetization, and M_0 is the initial magnetization before the application of the RF pulse. T_1 is called the longitudinal relaxation time or the spin-lattice relaxation time. T_2 is called the transverse relaxation time or spin-spin relaxation time. By

solving the Bloch equation for longitudinal and transverse components, the dynamic behavior of the magnetization in the laboratory frame is given by the following equations:

$$M_z(t) = M_0(1 - e^{-t/T_1}) \quad [1.2]$$

$$M_{xy}(t) = M_{xy}(0)e^{-i\gamma B_0 t}e^{-t/T_2} \quad [1.3]$$

After the RF pulse, Equation 1.2 describes the recovery of the longitudinal magnetization to the initial magnetization, where T_1 determines how fast this procedure is. In Equation 1.3, the term $M_{xy}(0)$ represents the transverse magnetization just after the applied RF pulse. And the term $e^{-i\gamma B_0 t}$ is known as the accumulated phase, indicating the angle between the transverse magnetization and the positive x-axis. The third term e^{-t/T_2} states that the transverse magnetization, or equivalently the MR signal, decays exponentially after the signal excitation, determined by T_2.

In principle, the signal reception has to be fast and finish before significant attenuation of the signal. In general, materials can be classified into two different types based on their T_2 values: long T_2 materials and short T_2 materials. The long T_2 materials, such as brain tissues, muscles and lipids, usually have T_2 values from a few milliseconds to hundreds of milliseconds. Therefore, when scanning the long T_2 materials, the above requirement of signal reception can be achieved by using regular pulse sequences. In contrast, short T_2 materials are associated with T_2 values that can be as short as a few microseconds. The short T_2 materials include, but are not limited to, tissues like cortical bone, teeth, tendon, etc Table 1.1 provides the approximate T_2 values of some short T_2 tissues under a 1.5 T field (7). For example, the T_2 value of cortical bone is about 0.5 ms under a 1.5 T field. Besides the short T_2 tissues, various contrast agents have also been introduced to reduce T_2 values and increase contrast. A good example is the iron oxide nanoparticles, which can effectively shorten local T_2 values of the scanned subject, especially at

high concentrations. For example, Wang et al. has reported that the T_2 of a suspension of 7 mM iron oxide nanoparticles could be about 1 ms under a 7 T field (8). As a result of the short T_2 values, it becomes a challenge to image short T_2 materials using regular clinical pulse sequences, such as the fast spin echo (FSE) sequence and the spoiled gradient echo (SPGR) sequence, because the fastest reception time of these pulse sequences is usually longer than a few milliseconds. Thus, short T_2 materials, such as cortical bone and tissues with accumulated iron oxide nanoparticles, are usually "invisible" in most of MR images.

However, bone diseases, such as osteoporosis, affect millions of people in the USA (9-11), so assessment of cortical bone using MRI is of significance for biological research and clinical diagnoses. Additionally, iron oxide nanoparticles have been widely used in various applications, such as visualization of vasculature, cell labeling and tracking, drug delivery, etc (12-26). These applications provide attractive benefits in both scientific research and clinical diagnoses. But challenges arise when one attempts to, for example, quantify iron oxide nanoparticles based on the MR magnitude images that suffer severe signal loss. As a consequence, there exists a high demand to develop MRI based methods to investigate short T_2 materials.

1.3 Detection and quantification of short T_2 materials using magnetic resonance imaging

In recent years, many remarkable approaches have been proposed for qualitative and quantitative studies of short T_2 materials, and they can be mainly classified into the following three categories.

1.3.1 Imaging based on post-processing and off-resonance effect

The first category concentrates on designing deliberate post-processing algorithms, some of which may require assistance of magnetization preparation pulses, to enhance image contrast of the short T_2 materials. Haacke et al. has proposed the susceptibility weighted imaging (SWI) method (27,28), which allows contrast enhancement of short T_2 materials. The SWI method first applies a high-pass filter to raw MR phase images that are obtained using the gradient echo sequence, and by multiplying the filtered phase images, negative contrast can be created for short T_2 materials. The SWI method has been implemented in studies of angiographic applications, iron deposition in organs, cartilage canals, and tracking of iron oxide nanoparticles (29-39). Liu et al. proposed the susceptibility gradient mapping (SGM) method by calculating the echo-shift of a complex gradient echo dataset to achieve a positive contrast of iron oxide nanoparticles (40). Bakker et al. and Zhao et al. have independently proposed the phase gradient mapping (PGM) method to produce positive contrast of iron oxide nanoparticles (23,41-43). This method has an advantage that the MR phase gradients can be directly calculated from wrapped MR phase images, without any phase unwrapping procedure.

By exploiting the field off-resonance, Stuber et al. proposed the inversion recovery on-resonance water suppression (IRON) method to highlight iron oxide nanoparticles by suppressing on-resonance water signals (44). In order to conserve signals surrounding the iron oxide nanoparticles, Seppenwoolde et al. utilized the white marker method to compensate the off-resonance magnetic field by a slice-selection gradient (45).

1.3.2 Quantification based on magnetic field off-resonance effect

Short T_2 materials are usually associated with signal loss in MRI, so quantification based on the signal intensity of short T_2 materials becomes difficult by using conventional pulse sequences. Fortunately, the MR phase surrounding the short T_2 materials includes information, such as the magnetic field off-resonance, that can be used for quantification methods. The quantitative susceptibility mapping (QSM) method is one of these methods. This method is based on Maxwell's equations, which indicate that an inhomogeneous susceptibility distribution in a region can result in magnetic field perturbation, or equivalently MR phase perturbation, both inside and outside the region. Therefore, the susceptibility of the region can be quantified by solving an inverse problem of Maxwell's equations, usually in Fourier domain. The QSM method has been applied to estimate susceptibilities of blood vessels, calcification in brains, brain tissues, iron oxide nanoparticles used for cell labeling, etc. (46-57).

1.3.3 Imaging and quantification based on special pulse sequences

This category of methods focuses on designing special pulse sequences that allow an extremely fast acquisition of the short T_2 signal before it decays, so that signal loss can be eliminated and short T_2 materials become detectable in the MR magnitude images. Furthermore, quantitation of short T_2 materials can be achieved. This type of pulse sequence includes the ultra-short echo time (UTE) sequence, the zero echo time sequence (ZTE), the sweep imaging with Fourier transformation (SWIFT) sequence, which allows the time interval between signal excitation and reception to go down to only several microseconds, and thus enables MRI to image materials with short T_2 values, such as cortical bone and iron oxide nanoparticles (7,58-61). The UTE sequence utilizes a short, rectangular pulse for signal excitation with a small flip angle (usually

less than 30˚), during which the phase encoding gradients are off. Immediately after the signal excitation, phase encoding gradients are turned on, followed by a radial k-space data sampling. The shortest gap between signal excitation and reception is limited by the hardware, such as the transmission-reception (T/R) switch and gradient coils, and the gap is usually in the scale of a few microseconds. The UTE sequence has been widely used to image cortical bones, iron oxide nanoparticles, and other types of short T_2 materials for both qualitative and quantitative studies (7,60,62-74). The ZTE sequence is similar with the UTE sequence, but the gradients are on during the excitation pulse, and signal acquisition immediately starts, eliminating the time cost on gradient ramps. The ZTE sequence has been used for imaging bones, teeth, etc (75-78). The SWIFT sequence was first proposed by Idiyatullin et al. (58,59) in 2006. This pulse sequence utilizes the gapped hyperbolic secant function, so that the signal excitation and reception are conducted almost simultaneously. The gradients are on and adjusted to allow a radial k-space data sample during the pulse sequence. Dummy scans are conducted to force the spins to a steady state. The SWIFT sequence has been used in various researches and applications. For example, Zhou et al. proposed to detect IONP labeled stem cells grafted in the myocardium using the SWIFT sequence (79). Idiyatullin et al. utilized the SWIFT sequence to visualize morphological structures of teeth in MRI (80). Lehto et al. successfully detected calcifications in injured brains using the SWIFT sequence (81). Nelson et al. applied the SWIFT sequence to breast imaging (82). And Wang et al. quantified highly concentrated IONP suspensions using the variable flip angle SWIFT sequence (8). However, in order to reconstruct the MR image by using fast Fourier transforms, the radial k-space has to be converted to a Cartesian k-space for sequences like UTE, ZTE, and SWIFT (83). Since the influence of the transverse relaxation is

minimized, images acquired using this type of sequences is usually weighted by the proton density or the T_1 value of the scanned material.

1.4 Objective and structure of this dissertation

Because of the significance of magnetic resonance imaging of short T2 materials, the objective of this dissertation is to propose new approaches that can extend the capabilities of MRI in qualitative (Chapters 2 and 3) and quantitative (Chapters 4 and 5) studies of short T_2 materials, particularly iron oxide nanoparticles and cortical bone. Chapter 2 introduces a method to improve detection specificity of iron oxide nanoparticles using the SWIFT sequence together with suppression of long T_2 tissues and fat. Chapter 3 presents a preliminary study of water and fat contained in swine humerus bones using the FSE and the SWIFT sequences. Chapter 4 demonstrates an MR phase gradient approach to quantification of iron oxide nanoparticles, which were used for labeling C6 glioma cells. Chapter 5 shows a novel method dealing with quantification of highly-concentrated aqueous iron oxide nanoparticle suspensions. Chapter 6 summarizes the works and provides the conclusions of this dissertation.

1.5 References

1. Gerlach W, Stern O. Das magnetische moment des silberatoms. Zeitschrift für Physik A Hadrons and Nuclei 1922;9(1):353-355.
2. Rabi I. Refraction of beams of molecules. Nature 1929;123:163-164.
3. Rabi I, Millman S, Kusch P, Zacharias J. The Molecular Beam Resonance Method for Measuring Nuclear Magnetic Moments. Phys. Rev 1938;53(495):318.
4. Bloch F, Packard, M. Nuclear infraction. Phys rev 1946;69:127.

5. Purcell E, Pound, R. Resonance absorption by nuclear magnetic moments in a solid. Phys rev 1946;69:37-8.

6. Damadian R, Goldsmith M, Minkoff L. NMR in cancer: XVI. FONAR image of the live human body. Physiol. Chem. Phys. **9** (1): 97–100.

7. Robson MD, Gatehouse PD, Bydder M, Bydder GM. Magnetic resonance: an introduction to ultrashort TE (UTE) imaging. Journal of computer assisted tomography 2003;27(6):825-846.

8. Wang L, Corum CA, Idiyatullin D, Garwood M, Zhao Q. T(1) estimation for aqueous iron oxide nanoparticle suspensions using a variable flip angle SWIFT sequence. Magnetic resonance in medicine : official journal of the Society of Magnetic Resonance in Medicine / Society of Magnetic Resonance in Medicine 2013;70(2):341-347.

9. Schneider EL, Guralnik JM. The aging of America. Impact on health care costs. JAMA : the journal of the American Medical Association 1990;263(17):2335-2340.

10. Kanis JA. Assessment of fracture risk and its application to screening for postmenopausal osteoporosis: synopsis of a WHO report. WHO Study Group. Osteoporosis international : a journal established as result of cooperation between the European Foundation for Osteoporosis and the National Osteoporosis Foundation of the USA 1994;4(6):368-381.

11. NIH Consensus Development Panel on Osteoporosis Prevention, Diagnosis, and Therapy, March 7-29, 2000: highlights of the conference. Southern medical journal 2001;94(6):569-573.

12. Kotek G, van Tiel ST, Wielopolski PA, Houston GC, Krestin GP, Bernsen MR. Cell quantification: evolution of compartmentalization and distribution of iron-oxide particles and labeled cells. Contrast media & molecular imaging 2012;7(2):195-203.

13. Suh JS, Lee JY, Choi YS, Yu F, Yang V, Lee SJ, Chung CP, Park YJ. Efficient labeling of mesenchymal stem cells using cell permeable magnetic nanoparticles. Biochemical and biophysical research communications 2009;379(3):669-675.

14. Kustermann E, Himmelreich U, Kandal K, Geelen T, Ketkar A, Wiedermann D, Strecker C, Esser J, Arnhold S, Hoehn M. Efficient stem cell labeling for MRI studies. Contrast media & molecular imaging 2008;3(1):27-37.

15. Yoshikawa T, Mitchell DG, Hirota S, Ohno Y, Oda K, Maeda T, Fujii M, Sugimura K. Gradient- and spin-echo T2-weighted imaging for SPIO-enhanced detection and characterization of focal liver lesions. Journal of magnetic resonance imaging : JMRI 2006;23(5):712-719.

16. Xie J, Wang J, Niu G, Huang J, Chen K, Li X, Chen X. Human serum albumin coated iron oxide nanoparticles for efficient cell labeling. Chemical communications 2010;46(3):433-435.

17. Wang Y, Zhu MT, Wang B, Wang M, Wang HJ, OuYang H, Feng WY. In vitro cytotoxicity of transparent yellow iron oxide nanoparticles on human glioma cells. Journal of nanoscience and nanotechnology 2010;10(12):8550-8555.

18. Ying E, Hwang HM. In vitro evaluation of the cytotoxicity of iron oxide nanoparticles with different coatings and different sizes in A3 human T lymphocytes. The Science of the total environment 2010;408(20):4475-4481.

19. Chen YC, Hsiao JK, Liu HM, Lai IY, Yao M, Hsu SC, Ko BS, Chen YC, Yang CS, Huang DM. The inhibitory effect of superparamagnetic iron oxide nanoparticle (Ferucarbotran) on osteogenic differentiation and its signaling mechanism in human mesenchymal stem cells. Toxicology and applied pharmacology 2010;245(2):272-279.

20. Cengelli F, Voinesco F, Juillerat-Jeanneret L. Interaction of cationic ultrasmall superparamagnetic iron oxide nanoparticles with human melanoma cells. Nanomedicine 2010;5(7):1075-1087.

21. McFadden C, Mallett CL, Foster PJ. Labeling of multiple cell lines using a new iron oxide agent for cell tracking by MRI. Contrast media & molecular imaging 2011;6(6):514-522.

22. Kim MJ, Kim JH, Choi JY, Park SH, Chung JJ, Kim KW, Mitchell DG. Optimal TE for SPIO-enhanced gradient-recalled echo MRI for the detection of focal hepatic lesions. AJR American journal of roentgenology 2006;187(3):W255-266.

23. Zhao Q, Langley J, Lee S, Liu W. Positive contrast technique for the detection and quantification of superparamagnetic iron oxide nanoparticles in MRI. NMR in biomedicine 2011;24(5):464-472.

24. Himmelreich U, Hoehn M. Stem cell labeling for magnetic resonance imaging. Minimally invasive therapy & allied technologies : MITAT : official journal of the Society for Minimally Invasive Therapy 2008;17(2):132-142.

25. Wu X, Tan Y, Mao H, Zhang M. Toxic effects of iron oxide nanoparticles on human umbilical vein endothelial cells. International journal of nanomedicine 2010;5:385-399.

26. van Tiel ST, Wielopolski PA, Houston GC, Krestin GP, Bernsen MR. Variations in labeling protocol influence incorporation, distribution and retention of iron oxide nanoparticles into human umbilical vein endothelial cells. Contrast media & molecular imaging 2010;5(5):247-257.

27. Haacke EM, Mittal S, Wu Z, Neelavalli J, Cheng YC. Susceptibility-weighted imaging: technical aspects and clinical applications, part 1. AJNR American journal of neuroradiology 2009;30(1):19-30.

28. Haacke EM, Xu Y, Cheng YC, Reichenbach JR. Susceptibility weighted imaging (SWI). Magnetic resonance in medicine : official journal of the Society of Magnetic Resonance in Medicine / Society of Magnetic Resonance in Medicine 2004;52(3):612-618.

29. Haacke EM, Makki M, Ge Y, Maheshwari M, Sehgal V, Hu J, Selvan M, Wu Z, Latif Z, Xuan Y, Khan O, Garbern J, Grossman RI. Characterizing iron deposition in multiple sclerosis lesions using susceptibility weighted imaging. Journal of magnetic resonance imaging : JMRI 2009;29(3):537-544.

30. Ishizaka K, Kudo K, Fujima N, Zaitsu Y, Yazu R, Tha KK, Terae S, Haacke EM, Sasaki M, Shirato H. Detection of normal spinal veins by using susceptibility-weighted imaging. Journal of magnetic resonance imaging : JMRI 2010;31(1):32-38.

31. Wang Y, Butros SR, Shuai X, Dai Y, Chen C, Liu M, Haacke EM, Hu J, Xu H. Different iron-deposition patterns of multiple system atrophy with predominant parkinsonism and idiopathetic Parkinson diseases demonstrated by phase-corrected susceptibility-weighted imaging. AJNR American journal of neuroradiology 2012;33(2):266-273.

32. Haacke EM, Garbern J, Miao Y, Habib C, Liu M. Iron stores and cerebral veins in MS studied by susceptibility weighted imaging. International angiology : a journal of the International Union of Angiology 2010;29(2):149-157.

33. Kirsch W, McAuley G, Holshouser B, Petersen F, Ayaz M, Vinters HV, Dickson C, Haacke EM, Britt W, 3rd, Larseng J, Kim I, Mueller C, Schrag M, Kido D. Serial

susceptibility weighted MRI measures brain iron and microbleeds in dementia. Journal of Alzheimer's disease : JAD 2009;17(3):599-609.

34. Barnes SR, Haacke EM. Susceptibility-weighted imaging: clinical angiographic applications. Magnetic resonance imaging clinics of North America 2009;17(1):47-61.

35. Nissi MJ, Toth F, Zhang J, Schmitter S, Benson M, Carlson CS, Ellermann JM. Susceptibility weighted imaging of cartilage canals in porcine epiphyseal growth cartilage ex vivo and in vivo. Magnetic resonance in medicine : official journal of the Society of Magnetic Resonance in Medicine / Society of Magnetic Resonance in Medicine 2013.

36. Cheng JL, Yang YJ, Li HL, Wang J, Wang MH, Zhang Y. In vivo tracing of superparamagnetic iron oxide-labeled bone marrow mesenchymal stem cells transplanted for traumatic brain injury by susceptibility weighted imaging in a rat model. Chinese journal of traumatology = Zhonghua chuang shang za zhi / Chinese Medical Association 2010;13(3):173-177.

37. Chen X, Zeng C, Luo T, Ouyang Y, Lv F, Rumzan R, Wang Z, Li Q, Wang J, Hou H, Huang F, Li Y. Iron deposition of the deep grey matter in patients with multiple sclerosis and neuromyelitis optica: a control quantitative study by 3D-enhanced susceptibility-weighted angiography (ESWAN). European journal of radiology 2012;81(4):e633-639.

38. Eibofner F, Steidle G, Kehlbach R, Bantleon R, Schick F. Positive contrast imaging of iron oxide nanoparticles with susceptibility-weighted imaging. Magnetic resonance in medicine : official journal of the Society of Magnetic Resonance in Medicine / Society of Magnetic Resonance in Medicine 2010;64(4):1027-1038.

39. Wang D, Zhu D, Wei XE, Li YH, Li WB. Using susceptibility-weighted images to quantify iron deposition differences in amnestic mild cognitive impairment and Alzheimer's disease. Neurology India 2013;61(1):26-34.

40. Liu W, Dahnke H, Jordan EK, Schaeffter T, Frank JA. In vivo MRI using positive-contrast techniques in detection of cells labeled with superparamagnetic iron oxide nanoparticles. NMR in biomedicine 2008;21(3):242-250.

41. de Leeuw H, Bakker CJ. Correction of gradient echo images for first and second order macroscopic signal dephasing using phase derivative mapping. NeuroImage 2012;60(1):818-829.

42. Bakker CJ, de Leeuw H, Vincken KL, Vonken EJ, Hendrikse J. Phase gradient mapping as an aid in the analysis of object-induced and system-related phase perturbations in MRI. Physics in medicine and biology 2008;53(18):N349-358.

43. Langley J, Zhao Q. Quantification of SPIO nanoparticles using phase gradient mapping. Conference proceedings : Annual International Conference of the IEEE Engineering in Medicine and Biology Society IEEE Engineering in Medicine and Biology Society Conference 2009;2009:3605-3608.

44. Stuber M, Gilson WD, Schar M, Kedziorek DA, Hofmann LV, Shah S, Vonken EJ, Bulte JW, Kraitchman DL. Positive contrast visualization of iron oxide-labeled stem cells using inversion-recovery with ON-resonant water suppression (IRON). Magnetic resonance in medicine : official journal of the Society of Magnetic Resonance in Medicine / Society of Magnetic Resonance in Medicine 2007;58(5):1072-1077.

45. Seppenwoolde JH, Viergever MA, Bakker CJ. Passive tracking exploiting local signal conservation: the white marker phenomenon. Magnetic resonance in medicine : official

journal of the Society of Magnetic Resonance in Medicine / Society of Magnetic Resonance in Medicine 2003;50(4):784-790.

46. Liu T, Xu W, Spincemaille P, Avestimehr AS, Wang Y. Accuracy of the morphology enabled dipole inversion (MEDI) algorithm for quantitative susceptibility mapping in MRI. IEEE transactions on medical imaging 2012;31(3):816-824.

47. Xu B, Liu T, Spincemaille P, Prince M, Wang Y. Flow compensated quantitative susceptibility mapping for venous oxygenation imaging. Magnetic resonance in medicine : official journal of the Society of Magnetic Resonance in Medicine / Society of Magnetic Resonance in Medicine 2013.

48. Liu J, Liu T, de Rochefort L, Ledoux J, Khalidov I, Chen W, Tsiouris AJ, Wisnieff C, Spincemaille P, Prince MR, Wang Y. Morphology enabled dipole inversion for quantitative susceptibility mapping using structural consistency between the magnitude image and the susceptibility map. NeuroImage 2012;59(3):2560-2568.

49. de Rochefort L, Brown R, Prince MR, Wang Y. Quantitative MR susceptibility mapping using piece-wise constant regularized inversion of the magnetic field. Magnetic resonance in medicine : official journal of the Society of Magnetic Resonance in Medicine / Society of Magnetic Resonance in Medicine 2008;60(4):1003-1009.

50. Langkammer C, Schweser F, Krebs N, Deistung A, Goessler W, Scheurer E, Sommer K, Reishofer G, Yen K, Fazekas F, Ropele S, Reichenbach JR. Quantitative susceptibility mapping (QSM) as a means to measure brain iron? A post mortem validation study. NeuroImage 2012;62(3):1593-1599.

51. Deistung A, Schweser F, Wiestler B, Abello M, Roethke M, Sahm F, Wick W, Nagel AM, Heiland S, Schlemmer HP, Bendszus M, Reichenbach JR, Radbruch A. Quantitative

susceptibility mapping differentiates between blood depositions and calcifications in patients with glioblastoma. PloS one 2013;8(3):e57924.

52. Li W, Wu B, Liu C. Quantitative susceptibility mapping of human brain reflects spatial variation in tissue composition. NeuroImage 2011;55(4):1645-1656.

53. Chen W, Zhu W, Kovanlikaya I, Kovanlikaya A, Liu T, Wang S, Salustri C, Wang Y. Intracranial Calcifications and Hemorrhages: Characterization with Quantitative Susceptibility Mapping. Radiology 2013.

54. Liu T, Spincemaille P, de Rochefort L, Kressler B, Wang Y. Calculation of susceptibility through multiple orientation sampling (COSMOS): a method for conditioning the inverse problem from measured magnetic field map to susceptibility source image in MRI. Magnetic resonance in medicine : official journal of the Society of Magnetic Resonance in Medicine / Society of Magnetic Resonance in Medicine 2009;61(1):196-204.

55. Shmueli K, de Zwart JA, van Gelderen P, Li TQ, Dodd SJ, Duyn JH. Magnetic susceptibility mapping of brain tissue in vivo using MRI phase data. Magnetic resonance in medicine : official journal of the Society of Magnetic Resonance in Medicine / Society of Magnetic Resonance in Medicine 2009;62(6):1510-1522.

56. Liu S, Neelavalli J, Cheng YC, Tang J, Mark Haacke E. Quantitative susceptibility mapping of small objects using volume constraints. Magnetic resonance in medicine : official journal of the Society of Magnetic Resonance in Medicine / Society of Magnetic Resonance in Medicine 2013;69(3):716-723.

57. Langley J, Liu W, Jordan EK, Frank JA, Zhao Q. Quantification of SPIO nanoparticles in vivo using the finite perturber method. Magnetic resonance in medicine : official journal

of the Society of Magnetic Resonance in Medicine / Society of Magnetic Resonance in Medicine 2011;65(5):1461-1469.

58. Idiyatullin D, Corum C, Park JY, Garwood M. Fast and quiet MRI using a swept radiofrequency. Journal of magnetic resonance 2006;181(2):342-349.

59. Idiyatullin D, Corum C, Moeller S, Garwood M. Gapped pulses for frequency-swept MRI. Journal of magnetic resonance 2008;193(2):267-273.

60. Tyler DJ, Robson MD, Henkelman RM, Young IR, Bydder GM. Magnetic resonance imaging with ultrashort TE (UTE) PULSE sequences: technical considerations. Journal of magnetic resonance imaging : JMRI 2007;25(2):279-289.

61. Weiger M, Pruessmann KP, Hennel F. MRI with zero echo time: hard versus sweep pulse excitation. Magnetic resonance in medicine : official journal of the Society of Magnetic Resonance in Medicine / Society of Magnetic Resonance in Medicine 2011;66(2):379-389.

62. Horch RA, Gochberg DF, Nyman JS, Does MD. Clinically compatible MRI strategies for discriminating bound and pore water in cortical bone. Magnetic resonance in medicine : official journal of the Society of Magnetic Resonance in Medicine / Society of Magnetic Resonance in Medicine 2012;68(6):1774-1784.

63. Reichert IL, Robson MD, Gatehouse PD, He T, Chappell KE, Holmes J, Girgis S, Bydder GM. Magnetic resonance imaging of cortical bone with ultrashort TE pulse sequences. Magnetic resonance imaging 2005;23(5):611-618.

64. Portman O, Flemming S, Cox JP, Johnston DG, Bydder GM. Magnetic resonance imaging of the normal pituitary gland using ultrashort TE (UTE) pulse sequences (REV 1.0). Neuroradiology 2008;50(3):213-220.

65. Nyman JS, Ni Q, Nicolella DP, Wang X. Measurements of mobile and bound water by nuclear magnetic resonance correlate with mechanical properties of bone. Bone 2008;42(1):193-199.

66. Girard OM, Du J, Agemy L, Sugahara KN, Kotamraju VR, Ruoslahti E, Bydder GM, Mattrey RF. Optimization of iron oxide nanoparticle detection using ultrashort echo time pulse sequences: comparison of T1, T2*, and synergistic T1- T2* contrast mechanisms. Magnetic resonance in medicine : official journal of the Society of Magnetic Resonance in Medicine / Society of Magnetic Resonance in Medicine 2011;65(6):1649-1660.

67. Du J, Carl M, Bydder M, Takahashi A, Chung CB, Bydder GM. Qualitative and quantitative ultrashort echo time (UTE) imaging of cortical bone. Journal of magnetic resonance 2010;207(2):304-311.

68. Du J, Bydder GM. Qualitative and quantitative ultrashort-TE MRI of cortical bone. NMR in biomedicine 2013;26(5):489-506.

69. Bae WC, Chen PC, Chung CB, Masuda K, D'Lima D, Du J. Quantitative ultrashort echo time (UTE) MRI of human cortical bone: correlation with porosity and biomechanical properties. Journal of bone and mineral research : the official journal of the American Society for Bone and Mineral Research 2012;27(4):848-857.

70. Springer F, Martirosian P, Schwenzer NF, Szimtenings M, Kreisler P, Claussen CD, Schick F. Three-dimensional ultrashort echo time imaging of solid polymers on a 3-Tesla whole-body MRI scanner. Investigative radiology 2008;43(11):802-808.

71. Biswas R, Bae W, Diaz E, Masuda K, Chung CB, Bydder GM, Du J. Ultrashort echo time (UTE) imaging with bi-component analysis: bound and free water evaluation of bovine cortical bone subject to sequential drying. Bone 2012;50(3):749-755.

72. Li S, Chang EY, Bae WC, Chung CB, Gao S, Bao S, Bydder GM, Hua Y, Du J. Ultrashort echo time bi-component analysis of cortical bone-a field dependence study. Magnetic resonance in medicine : official journal of the Society of Magnetic Resonance in Medicine / Society of Magnetic Resonance in Medicine 2013.

73. Du J, Hamilton G, Takahashi A, Bydder M, Chung CB. Ultrashort echo time spectroscopic imaging (UTESI) of cortical bone. Magnetic resonance in medicine : official journal of the Society of Magnetic Resonance in Medicine / Society of Magnetic Resonance in Medicine 2007;58(5):1001-1009.

74. Kokabi N, Bae W, Diaz E, Chung CB, Bydder GM, Du J. Ultrashort TE MR imaging of bovine cortical bone: the effect of water loss on the T1 and T2* relaxation times. Magnetic resonance in medicine : official journal of the Society of Magnetic Resonance in Medicine / Society of Magnetic Resonance in Medicine 2011;66(2):476-482.

75. Weiger M, Stampanoni M, Pruessmann KP. Direct depiction of bone microstructure using MRI with zero echo time. Bone 2013;54(1):44-47.

76. Weiger M, Pruessmann KP, Bracher AK, Kohler S, Lehmann V, Wolfram U, Hennel F, Rasche V. High-resolution ZTE imaging of human teeth. NMR in biomedicine 2012;25(10):1144-1151.

77. Weiger M, Brunner DO, Dietrich BE, Muller CF, Pruessmann KP. ZTE imaging in humans. Magnetic resonance in medicine : official journal of the Society of Magnetic Resonance in Medicine / Society of Magnetic Resonance in Medicine 2013;70(2):328-332.

78. Sun Y, Ventura M, Oosterwijk E, Jansen JA, Walboomers XF, Heerschap A. Zero echo time magnetic resonance imaging of contrast-agent-enhanced calcium phosphate bone defect fillers. Tissue engineering Part C, Methods 2013;19(4):281-287.

79. Zhou R, Idiyatullin D, Moeller S, Corum C, Zhang H, Qiao H, Zhong J, Garwood M. SWIFT detection of SPIO-labeled stem cells grafted in the myocardium. Magnetic resonance in medicine : official journal of the Society of Magnetic Resonance in Medicine / Society of Magnetic Resonance in Medicine 2010;63(5):1154-1161.

80. Idiyatullin D, Corum C, Moeller S, Prasad HS, Garwood M, Nixdorf DR. Dental magnetic resonance imaging: making the invisible visible. Journal of endodontics 2011;37(6):745-752.

81. Lehto LJ, Sierra A, Corum CA, Zhang J, Idiyatullin D, Pitkanen A, Garwood M, Grohn O. Detection of calcifications in vivo and ex vivo after brain injury in rat using SWIFT. NeuroImage 2012;61(4):761-772.

82. Nelson MT, Benson JC, Prescott T, Corum CA, Snyder A, Garwood M. Breast MRI using SWeep Imaging with Fourier Transform (SWIFT). European journal of radiology 2012;81 Suppl 1:S109.

83. Jackson JI, Meyer CH, Nishimura DG, Macovski A. Selection of a convolution function for Fourier inversion using gridding [computerised tomography application]. IEEE transactions on medical imaging 1991;10(3):473-478.

Table

Table 1.1: Approximate T_2 values of short T_2 materials

Tissue	T_2
Ligament	4 – 10 ms
Knee menisci	5 – 8 ms
Cortical bone	0.4 – 0.5 ms
Dentine	0.15 ms
Dental enamel	70 μs
Periosteum	5 – 11 ms

Table 1.1 provides the approximate T_2 values of some tissues estimated under 1.5 T.

CHAPTER 2

IMPROVING DETECTION SPECIFICITY OF IRON OXIDE NANOPARTICLES (IONPS) USING THE SWIFT SEQUENCE WITH LONG T_2 SUPPRESSION[1]

[1] Wang, L., Tang, W., Zhen, Z., Chen, H., Xie, J., and Zhao, Q. Submitted to Magnetic Resonance Imaging on 09/18/2013.

2.1 Abstract

In order to improve the detection specificity of iron oxide nanoparticles (IONPs) delivered to tumors, we embedded saturation pulses into the SWeep Imaging using Fourier Transformation (SWIFT) sequence to suppress long T_2 tissues and fat. Simulation of the Bloch equation was first conducted to study behavior of the saturation pulses of various lengths under different T_2 and off-resonance conditions. MR experiments were then conducted using in vivo mouse xenografts and a phantom consisting of IONPs, vegetable oil, and explanted tumor specimen, without and with long T_2 suppression under a 7 T magnetic field. For the in vivo study, Arginine-Glycine-Aspartate coated 10nm IONPs (RGD-IONPs) were delivered to tumors implanted in nude mice through both intra-tumor and intravenous injections. Histological studies confirmed that RGD-IONPs efficiently homed to tumors through RGD-integrin interaction. Compared to conventional SWIFT, the proposed method suppressed long T_2 species successfully, but had less influence on short T_2 species. For both the in vivo and ex vivo studies, significantly improved contrast-to-noise ratio (CNR) was achieved between the IONPs and the long T_2 species.

2.2 Introduction

Iron oxide nanoparticles (IONPs) have been widely used as a T_2/T_2*-shortening contrast agent in magnetic resonance imaging (MRI) for various applications, such as cell labeling and tracking, and drug delivery [1-8]. IONPs are usually recognized as a negative contrast agent, inducing hypointensities or signal void on MR images acquired with regular pulse sequences, such as the fast spin echo (FSE) and spoiled gradient echo (SPGR) sequences. A major challenge arises when one attempts to differentiate IONPs from tissues with short T_2/T_2* values, air cavities, or susceptibility artifacts, especially when the signal-to-noise ratio (CNR) is very low.

These problems can be mitigated with the use of recently developed pulse sequences such as ultra-short echo time (UTE) and sweeping imaging using Fourier transforms (SWIFT) sequences [9-13]. These sequences shorten the time interval between radiofrequency (RF) transmission and reception, and reduce data sampling down to only a few microseconds. These sequences take advantage of the T_1-shortening effect of IONPs and induce hyper-intensities or signal increase on MR images. This development is important for improving both the detection specificity of IONPs as well as the image SNR. For example, the SWIFT sequence has been successfully applied to detect IONP-labeled stem cells grafted in the myocardium [14], while the UTE has been used to enhance IONP-based tumor detection [5,15]. However, long T_2 species (such as fluids) and fat also appear bright in the UTE and SWIFT images, posing a challenge to detect the IONPs among these tissues. Therefore, suppressions of long T_2 species and fat are crucial for improving the contrast and detection specificity of IONPs.

Various suppression approaches have been developed and they can be mainly classified into two categories. The first strategy is focused on distinguishing changes of image contrast, when different scan parameters are applied. For example, one widely used approach is to scan an object using the UTE sequence with dual echo times [15-18]. The signal void of short T_2 species is more severe in the second echo acquisition than that in the first one, while neither images show obvious changes for long T_2 species. The subtraction of the two acquisitions consequently suppresses the signal from long T_2 species to achieve the enhancement of short T_2 species.

The second strategy is to implement RF saturation pulses. Because long T_2 species have a narrow spectrum in the frequency domain and are sensitive to a long RF pulse (with short bandwidth), hence they can be suppressed by using a long RF pulse, with little influence on short T_2 species [16,19]. An early study utilized a long rectangular $\pi/2$ pulse to excite long T_2 species

at the water resonant frequency, followed by a gradient spoiler to dephase the excited long T_2 species, while leaving short T_2 species minimally affected [20]. With the consideration of fat saturation, Du et al. shifted the central frequency of the suppression pulse between water and fat to suppress both components and improve the detection specificity of short T_2 species using the UTE sequence at a 3 T magnetic field strength [21]. Instead of using a single banded pulse, an alternative method implemented either two separated RF pulses or a single dual-banded RF pulse focused at water and fat frequencies [19,22-24]. For example, Luhach et al. have investigated the prostate-to-bone tumor in ex vivo specimens using the SWIFT sequence inserted with a dual band Gaussian pulse [25].

In this work, we propose to suppress long T_2 and fatty species in order to improve the detection specificity of the delivered IONPs to tumors in vivo and ex vivo using the SWIFT sequence. In order to achieve the goal, we proposed to embed two Gaussian pulses into the SWIFT sequence, referred to as SWIFT-2sat. Similar with the UTE based saturation method [21], the SWIFT sequence embedded with only one Gaussian pulse, referred to as SWIFT-1sat, was also conducted to provide a comparison. To increase the amount of delivered IONPs, Arginine-Glycine-Aspartate coated 10 nm IONPs (RGD-IONPs) were injected into 4T1 tumor xenograft models for the in vivo study. Ex vivo scans were also performed with explanted tumors. Finally, histological studies were performed to verify the results of the MR studies.

2.3 Materials and method

Bloch Equation Simulation

The Bloch equation simulation was performed to calculate the ratio between z-component of magnetization, M_z, and the initial magnetization, M_0, after Gaussian pulses are applied with

various pulse durations in the absence of any off-resonance effect [26]. The T_2 of the magnetization varied from 10^{-2} to 10^2 ms, while the T_1 was set to a large value (10^3 s) to minimize the influence of longitudinal relaxation. The amplitude of the Gaussian pulses was determined by the assumption that a perfect 90° flip angle can be achieved with an infinite long T_2.

Then, the off-resonance behavior of the Gaussian pulses was investigated using the Bloch equation simulation [26], assuming T_1 and T_2 of the magnetization to be 10^3 s and 50 ms, respectively. The frequency offset varied from -500 Hz to 500 Hz.

Arginine-Glycine-Aspartate (RGD) coated IONPs

cyclo(Arg-Gly-Asp-DTyr-Lys) or cyclo(RGDyK) is an RGD derivative. The water-soluble IONPs (Fe_3O_4) with carboxyl groups on the surface (10 nm, from Ocean Nanotech, Inc.) were mixed with N-(3-Dimethylaminopropyl)-N′-ethylcarbodiimide hydrochloride (EDC) and N-Hydroxysuccinimide (NHS) (100×) in the borate buffer (pH 8.3). After incubating at room temperature for 30 minutes, the activated particles were collected by centrifugation, washed 3 times by Phosphate-Buffered Saline (PBS) (pH = 7.4), and re-dispersed in PBS. c(RGDyK) (200×) in Dimethyl Sulfoxide (DMSO) was added to the particles solution and the mixture was incubated at room temperature for 2 hours. The resulting RGD conjugated IONPs were collected by centrifugation, washed, and re-dispersed in PBS.

Animal Preparations

Animal studies were performed according to a protocol approved by the Institutional Animal Care and Use Committee (IACUC) of University of Georgia. Mouse breast cancer cell line 4T1

was cultured in 1640 medium supplemented with 10% fetal bovine serum (FBS) at 37°C in 5% CO_2 humidified condition. For tumor inoculation, a total of ~10^6 cells were subcutaneously injected to the right hind leg of three nude mice. The tumor size was inspected every three days, and was computed using the following equation: volume (mm^3) = length × $(width)^2/2$. MRI and histological studies were conducted about one week later when the average tumor size reached about 200 mm^3. In detail, to first demonstrate the proposed approaches, intra-tumor injection of 0.1 mL aqueous suspensions of non-conjugated IONPs (5 mM Fe^{3+} in concentration) was conducted to one mouse to induce an area of highly concentrated IONPs inside the tumor. In vivo MR scans were conducted before and immediately after the injection. Secondly, the RGD-modified IONPs (10 mg Fe/Kg) were intravenously injected to the tail veins of two mice, and allowed 24 hours to target and accumulate in the tumors. Then, different approaches (in vivo MRI, ex vivo MRI and histology) were applied to examine the distribution of the RGD-IONPs inside the tumors.

Tumor specimen phantom

To visualize the detailed distribution of the RGD-IONPs, the tumor was harvested by surgery after the in vivo MR scans, and fixed in formalin for 72 hours before the tumor specimen was immerged into 1% agar gel inside a cylindrical glass container. To provide referential materials of different T_2 values and resonant frequencies, two 0.3 mL plastic vials, filled with vegetable oil and aqueous suspensions of 1 mM IONPs, were also inserted into the agar gel to make a phantom.

MR Experiments

All MR experiments were performed on a 7 T Varian Magnex small animal scanner (Agilent Technologies, Santa Clara, CA) with a maximum gradient strength of 440 mT/m. A high-pass birdcage coil (3.8 cm diameter) was used for both RF transmission and signal reception.

In vivo MR scans

A 2D FSE sequence was utilized to generate T_2 weighted anatomical axial images of the tumor-bearing mice with the following parameters: TR/TE = 2 s/30 ms, echo train length = 8, spectral width of acquisition (sw) = 100 kHz, field-of-view (FOV) = 3.5 cm, slice thickness (thk) = 1 mm, image size = 256^2. However, to minimize the image distortion due to intra-tumor injection of IONPs, a shorter TE was set to 12 ms rather than 30 ms, while keeping the same TR of 2 s.

Both 3D SPGR and SWIFT sequences were implemented to generate T_1 weighted images. For the SPGR sequence, we utilized the shortest achievable TE for the scanner, and the scan parameters are listed in the following: flip angle = 6°, TR/TE = 6.5/3.15 ms, sw = 62.5 kHz, FOV = 50^3 mm^3, image size = 256^3.

For the SWIFT sequence, a gapped hyperbolic secant pulse, with the dimensionless shape factor n = 1 and truncation factor β = 7.6, was implemented to excite a 6° flip angle. The pulse was divided into 256 segments, and each segment consisted of 4 μs pulse element and 12 μs free induction decay for data sampling. The dead time between the end of a pulse element and the beginning of data sampling was set to 3.9 μs, referred to as the effective TE for SWIFT. The TR of SWIFT was set to 6 ms. The pulse bandwidth (bw) and the spectral width were both set to 62.5 kHz in this study. The entire 3D radial k-space consisted of 64,000 spokes, and covered a

spherical FOV with the radius equal to 50 mm. For both of the SPGR and SWIFT sequences, 512 dummy scans were implemented to achieve a steady state at the beginning of the scans.

Additionally, the SWIFT-2sat sequence, as illustrated in Figure 2.1, was conducted to further enhance contrast and detection specificity of IONPs. Specifically, the magnetization preparation was performed using two 90º Gaussian pulses placed at water and fat frequencies under 7 T magnet. Although the magnetic field was carefully shimmed before the experiment, the in vivo scan might still suffer poor field homogeneity. So in order to improve the tolerance of field inhomogeneity, a relatively short pulse length (8 ms) was selected for the two Gaussian pulses, according to the simulation result (shown in Figure 2.2). Gradient spoilers were then presented immediately after each Gaussian pulse to dephase the excited long T_2 species and fat.

As a comparison, the SWIFT-1sat sequence used a single 90º Gaussian pulse, centered at the mid-point between water and fat frequencies, to suppress the long T_2 tissues and fat simultaneously, followed by a gradient spoiler. By setting the pulse duration to 2 ms and 4 ms, two situations were investigated to study how the pulse width influences the saturation performance for the SWIFT-1sat sequence. Note that for the above two methods, 16 radial spokes in the k-space were sampled using the SWIFT sequence after every saturation procedure.

Ex vivo MR scans

To further conduct quantitative measurement of IONP contrast improvement, the tumor of the mouse with systematic injection of RGD-IONPs was harvested by surgery. A phantom was made containing a vial of aqueous IONPs suspensions (1 mM Fe^{3+}), a vial of vegetable oil, and the tumor specimen harvested. Both T_2 and T_2^* maps of the specimen were measured using spin echo and spoiled gradient echo sequences with five echo times: TE = 10, 20, 30, 40, and 50 ms

for the spin echo sequence, and TE = 2.64, 6.74, 10.84, 14.94, and 19.04 ms for the spoiled gradient echo sequence. The rest scan parameters of both sequences were listed in the following: TR = 2.5 s, sw = 100 kHz, FOV = 35^2 mm^2, thk = 1 ms, image size = 256^2, 16 axial slices.

Additionally, 3D images were acquired by using the SPGR, SWIFT, and SWIFT-1sat sequences with the same scan parameters as that of the in vivo experiment. Compared with the in vivo experiment, a much better field homogeneity could be achieved for the phantom. Therefore, several longer durations (8, 16, 24, and 32 ms) of the Gaussian pulse at the water frequency were implemented to investigate the resulted performance of the SWIFT-2sat sequence on the long T_2 suppression. The fat saturation was fulfilled by using a fixed 8 ms Gaussian pulse with the flip angle of 135°.

Histological studies

Except using the MRI scans, the existence of RGD-IONPs inside the tumor was also verified using double staining of Prussian blue and murine β_3. In detail, the snap-frozen tumor tissues were cut into slices of 8 μm thickness and mounted on glass slides. After dried at room temperature for 20 minutes, the slices were fixed in 10% formalin (w/v) for 30 minutes.

For the immunochemistry staining of murine β_3, the fixed slices were incubated with 0.3% H_2O_2 solution in PBS for 10 minutes to block endogenous peroxidase activity and then gently washed by flowing water for 5 minutes 3 times. The slices were incubated with goat serum (5%, w/v) for 1 hour at room temperature and then washed with PBS. Primary antibody (ab75872) was then added and incubated with the slices overnight at 4 ˚C. After gently washing by PBS (1x, pH 7.4) for 5 minutes 3 times, the slices were incubated with the second antibody (ab6721)

for another 1 hour at room temperature. The slices were washed by PBS and then developed with 3, 3'-diaminobenzidine (DAB) substrate solution until desired color intensity was reached.

Following the staining of murine β_3, the resulting slices were immersed in Prussian blue staining working solution (a mixture of equal volume of 20% hydrochloric acid and 10% potassium ferrocyanide solution) for 40 minutes at room temperature. After being gently washed by PBS, the slices were dehydrated in a concentration gradient of ethanol (75%, 90%, and 100%). Subsequently, xylene was applied and the tissues were mounted with Canada balsam. The images were acquired on a Nikon Eclipse 90i microscope.

Data processing

Images acquired using Cartesian sampling were obtained directly from fast Fourier transforms of the k-space data using Matlab (MathWorks, Natick, MA). The raw data of the SWIFT scans were first processed using house-developed code written in LabVIEW (National Instruments, Austin, TX), and then interpolated with a Kaiser-Bessel function onto a Cartesian grid utilizing compiled Matlab mex code, resulting in the image size = 256^3 [27]. Fast Fourier transforms of the post-processed raw data were performed to generate the complex SWIFT images at last.

Regarding the phantom images, the agar gel and the two vials containing IONPs and vegetable oil were segmented simply based on the difference of their image intensities [28], so that their mean intensities could then be calculated within the segmented regions. Noise standard deviation was estimated using regions outside the phantom. The SNRs of the IONPs, oil, and agar gel were derived as a ratio of the corresponding mean intensities over the noise standard

deviation. The contrast-to-noise ratio (CNR) was calculated as a subtraction between the corresponding SNRs, respectively.

2.4 Results

Figure 2.2 gives results of the Bloch equation simulation, illustrating the ratio of M_z over M_0 as functions of T_2 (Figure 2.2a) and off-resonance frequency (Figure 2.2b), respectively. Figure 2.2a indicates that during the long Gaussian pulses, the short T_2 species are barely affected and a smaller flip angle is resulted due to loss of coherence. For example, a 90° Gaussian pulse with the duration of 32 ms can only excite components with T_2 of 1 ms to a flip angle about 30° ($M_z/M_0 \sim 0.85$). However, even though a long Gaussian pulse has less influence on short T_2 components, it is more susceptible to field off-resonance effects. As shown in Figure 2.2b, the same 32 ms Gaussian pulse only has a full width at half maximum (FWHM) about 100 Hz, but the FWHM of a 2 ms Gaussian pulse is close to 1 kHz, which is more tolerant to field inhomogeneity. The latter was therefore selected for the SWIFT-1sat sequence to cover the frequency gap between water and fat under a 7 T magnetic field.

For the mouse received intra-tumor injection of IONPs, T_2 weighted pre-injection FSE image was acquired and shown in Figure 2.3a, where the tumor appears brighter than the surroundings muscles. Compared to the pre-injection image, two post-injection MR images acquired using FSE and SPGR sequences showed significant signal loss inside the tumors in Figures 2.3b and 2.3c, which are attributed to IONP-induced T_2 shortening. With a much shorter TE of 3.9 μs, almost 3 orders of magnitude smaller than that used in the SPGR, signal void was significantly mitigated inside the tumor in the SWIFT image, as shown in Figure 2.3d. By regarding the muscles as a long T_2 material in this study, Figure 2.3e shows an image taken by using the

SWIFT-2sat sequence, for which two 8 ms suppression pulses were selected to improve its tolerance to the off-resonance effect. In Figure 2.3e, we observed significantly enhanced tumor-to-tissue contrast, mainly owing to suppressed signals from long T_2 species. As a comparison, the SWIFT-1sat sequence was conducted with a single 2 ms Gaussian pulse to suppress both long T_2 components and fat, and the result shown in Figure 2.3f was comparable to Figure 2.3e, with similar positive contrast from the IONPs. However, an increase of pulse duration to 4 ms (not shown in the Figure 2.3) narrowed the FWHM about half of the frequency shift between water and fat at 7 T, and the single Gaussian pulse failed to suppress both the long T_2 species and fat.

Figure 2.4 presents the in vivo T_2 weighted MR images for the mouse with systematic delivery of RGD-IONPs through tail vein injection. Compared with the surrounding muscles, the tumor shows a positive contrast in Figure 2.4a, indicating that the tumor tissue had a longer T_2 in the absence of RGD-IONPs. A presumable tumor necrotic core was observed and indicated by an arrow. After 24 hours post-injection, signal void in the T_2-weighted FSE image (Figure 2.4b) and T_1-weighted SPGR image (Figure 2.4c) was observed inside the tumor, especially surrounding the necrotic core, which is attributable to the delivered RGD-IONPs. Benefiting from the extremely short TE of the SWIFT sequence, no significant signal void was seen in Figure 2.4d, but no significant contrast enhancement for the IONPs was observed either within the tumor region. An image taken by using the SWIFT-2sat method to suppress tissues and fat surrounding the tumor is shown in Figure 2.4e, and as a result, it highlighted the delivered RGD-IONPs. Although an 8 ms Gaussian pulse was utilized to improve tolerance of field inhomogeneity, the off-resonance effect was still presented at the left side of Figure 2.4e, where mouse tissues were not completely suppressed at the air-tissue boundary. Figure 2.4f was

acquired using the SWIFT-1sat sequence with a 2 ms Gaussian pulse, which seemed to indicate an over-saturation of the RGD-IONPs by reducing its signal, while suppressing the long T_2 components.

For the ex vivo experiment, Figure 2.5 presents MR images of the phantom, consisting of two vials of aqueous IONPs suspension and vegetable oil, as well as the tumor specimen harvested from the mouse shown in Figure 2.4. IONP-induced signal loss inside the vial was observed in both T_2 and T_2^* weighted images (Figures 2.5a-b). By using a 3D SPGR sequence with the shortest TE of 3.15 ms, the IONPs showed similar image intensity with the surrounding agar gel (Figure 2.5c). Attributed to an extremely short TE, the SWIFT sequence is able to present the IONP suspension as positive contrast relative to the agar gel in Figure 2.5d. Based on the negative contrast in Figures 2.5a-b, the distribution of the delivered RGD-IONPs could be fairly specified in the tumor, but with long echo times, the signal void led to a poor signal-to-noise ratio (SNR). In Figure 2.5a, the presumable necrotic core, firstly founded in Figure 2.4, was indicated by the arrow. In Figures 2.5c-d of the T_1 weighted SPGR and SWIFT images, the tumor region is associated with a better SNR but a poor image contrast, making it hard to specify the RGD-IONPs.

To further investigate the properties of the RGD-IONPs distributed regions, both the T_2 and T_2^* maps of the phantom were derived and presented in Figures 2.6a and 2.6b, respectively. Due to inhomogeneous distribution of IONPs in the tumor, the T_2 values of the area containing RGD-IONPs in the tumor are approximately between 20 ms to 30 ms, while the T_2^* values are generally shorter than 10 ms. As a reference, the T_2 and T_2^* values of the 1 mM IONP suspension are about 23 ms and 5.5 ms, respectively.

In order to improve detection specificity of IONP, different pulse widths for long T_2 and fat suppressions were implemented for the SWIFT-1sat and SWIFT-2sat methods. Figure 2.7a was obtained using the SWIFT-1sat sequence with a 2ms Gaussian pulse. Inhomogeneous distribution of the RGD-IONPs in the tumor is clearly revealed, highlighted as positive contrast. The center area remained dark, likely a necrotic core. Noticeable suppressions of agar gel and oil were observed, but the SWIFT-1sat also caused undesired suppression of IONPs both in the tumor and the vial. A further increase of the pulse width to 4 ms caused inefficient suppression of the long T_2 species, leading to suboptimal contrast of the IONPs (Figure 2.7b). This is probably because the FWHM, about 500 Hz for the 4 ms Gaussian pulse, is too narrow to cover the frequency gap between water and fat. According to the Bloch equation simulation in Figure 2.2b, for SWIFT-2sat, we compared the performance of different pulse lengths (8, 16, 24, and 32 ms) for long T_2 suppression, with a fixed 8 ms pulse length for fat suppression. As shown in Figures 2.7c-f, the tumor tissue, agar gel, and oil were better suppressed compared with Figure 2.7a, and the RGD-IONPs were clearly delineated inside the tumor, indicating a better performance of the SWIFT-2sat sequence. Consistent with the simulation result in Figure 2.2a, these ex vivo results also confirmed that a short pulse might decrease the signal from IONPs. For example, details of the distribution of the delivered RGD-IONPs in the tumor region shown in Figure 2.7c were suppressed compared with that in Figure 2.7f. But on the other hand, Figure 2.7f suffered the field off-resonance effect, when using a 32 ms Gaussian pulse with a narrow FWHM, resulting in that the agar gel located at lower half of the phantom was not fully suppressed.

To further compare the performance of the SWIFT-1sat and SWIFT-2sat, the SNRs of the aqueous IONP suspension (SNR_{IONP}), the vegetable oil (SNR_{oil}), and the agar gel (SNR_{gel}) were

derived using Figure 2.5d and Figure 2.7 and presented in Table 2.1. For all of the three different imaging methods listed in the table, the IONP suspension has higher SNR values than those of the agar gel. Using the SWIFT-2sat method, the SNR_{gel} was decreased to about one-third (from 21.2 down to 7.4) compared to that using the regular SWIFT method. Similarly, the oil signal was also suppressed about half (from 32 down to 13.6) by the SWIFT-2sat method. With a 2 ms Gaussian pulse, the SWIFT-1sat method also approximately reduced the SNRs of agar gel by 50% and oil by 30%, but not as good as the SWIFT-2sat method. When the Gaussian pulse was increased to 4 ms for the SWIFT-1sat sequence, the SNR values of the three materials were almost the same as that resulted from the regular SWIFT method.

In addition to SNR, the CNR between the IONP suspensions and the agar gel (referred to as $CNR_{IONP\text{-}gel}$) as well as that between the IONP suspensions and the vegetable oil (referred to as $CNR_{IONP\text{-}oil}$) were also derived. Unlike the T_2 or T_2^* weighted scans, the SWIFT sequence was able to generate positive $CNR_{IONP\text{-}gel}$. About 40% increase of $CNR_{IONP\text{-}gel}$ was reached using the SWIFT-1sat method with a 2 ms Gaussian pulse length. When using the SWIFT-2sat sequence, the highest $CNR_{IONP\text{-}gel}$ and $CNR_{IONP\text{-}oil}$ were about 3 times larger than that obtained with the regular SWIFT sequence. Both the $CNR_{IONP\text{-}gel}$ and $CNR_{IONP\text{-}oil}$ became larger along with the increase of the pulse length, which again implies that short pulse duration may partially suppress the signal from IONPs.

To further investigate the tumor targeting, we performed histological studies with the dissected tumor tissues (Figure 2.8). Specifically, Prussian blue and integrin β_3 double staining were conducted. Prussian blue staining is a sensitive histochemical test for Fe and has been widely used to study distribution of iron-containing nanoparticles both ex vivo and in vivo. In the current tumor tissues, a high level of iron deposit (blue) was found in the masses, suggesting

good accumulation in the tumor. This is consistent to the signal loss shown in the post-injection MR images before suppression, and indicates that the highlighted regions by using SWIFT-2sat and SWIFT-1sat are more likely due to the IONPs in the tumor. An anti-integrin β_3 antibody was used to reveal the distribution of integrin $\alpha_v\beta_3$ in the tissue samples. Integrin $\alpha_v\beta_3$ is known to be overexpressed on neoplastic vasculatures and also, on cancer cells of various types, such as U87MG cells. Indeed, positive β_3 staining (brown) was found across the tumor tissues. Overall good correlation was found between the two stainings, indicating that the particle accumulation was mainly mediated by RGD-integrin interaction.

2.5 Discussion

In this study, both in vivo and ex vivo experiments were conducted using various pulse sequences to acquire MR images for detection of IONPs deposited in the implanted tumors. Generally, T_2 and T_2^* weighted images are usually associated with a poor SNR, which is attributed to the signal incoherence caused by IONPs due to the T_2-shortening effect. Such an effect is manifested by negative contrast of IONPs, which compromises the detection of IONPs as a contrast agent. The SWIFT sequence can improve the SNR of the IONP deposited regions, however, the contrast between IONPs and surrounding tissues is improved only marginally. In order to further improve the detection specificity of IONPs, we introduced herein the SWIFT-2sat sequence, which combines the SWIFT sequence with magnetization preparation. The two Gaussian pulses target the frequencies of water and fat, respectively. It is expected that fat and long T_2 species, such as tumor tissues, can be efficiently saturated in the acquired SWIFT-2sat images. On the other hand, short T_2 species, mainly IONPs in this study, are minimally influenced due to their insensitivity to the long RF pulses.

SWIFT-2sat was demonstrated on a 7 T MR scanner, and compared with the SWIFT-1sat method. Since the SWIFT-1sat method only used one saturation pulse with its central frequency placed at the mid-point of the water and fat, the FWHM of the implemented pulse has to be set wide enough to cover the frequency gap between water and fat. This corresponds to a 2-ms pulse duration under 7 T according to the Bloch equation simulation (the red curve in Figure 2.2b). Because short T_2 species are also subjective to RF pulses with wide FWHM, the signals from IONPs were partially saturated by the 2 ms Gaussian pulse as well. Longer pulse duration of 4 ms, on the other hand, failed to achieve the saturation result, as shown in Figure 2.7b.

Highly concentrated IONPs appear bright in the T_1-weighted SWIFT images. With an intra-tumor delivery, the IONPs in the tumor could be easily delineated from the surrounding tissues in Figure 2.3d, even though the contrast was further improved in Figures 2.3e and 3f by using the SWIFT-2sat and SWIFT-1sat sequences. However, it is practically impossible to deliver such a high concentration of IONPs to the areas of interest, such as tumors. At a low iron concentration, the spectral profile of the IONPs could become narrow and close to that of regular tissues [29], so that saturation using a short RF pulse may downgrade the image SNR and reduce the contrast between IONPs and surrounding tissues, as demonstrated in Table 2.1. Another example can be found in Figure 2.4f that utilization of a 2 ms Gaussian pulse led to an over-saturation of all the species, including RGD-IONPs.

Both the simulation and the experimental results suggest that the pulse duration should be neither too short, nor too long. Otherwise off-resonance effect may comprise the image quality with the remaining long T_2 signal unsuppressed. This is crucial especially for an in vivo scan, since a homogeneous field shimming is usually harder to achieve compared with a phantom scan. For example, with an 8 ms Gaussian pulse, long T_2 signals were suppressed around the

center area of the mouse body but they still existed at the peripheral air-tissue boundary in Figure 2.4e. However, for the ex vivo scan, insufficient suppression only happened when a 32 ms Gaussian pulse was applied (as shown in Figure 2.7f). Therefore, a proper selection of the pulse duration is required to optimize image contrast and improve the detection specificity of IONPs.

In addition to optimization of the pulse length, we also tried to minimize the inhomogeneous signal suppression from possible sources, such as inhomogeneous B_0 and B_1 fields. In this study, a careful shimming procedure of the B_0 magnetic field was conducted before all the scans. And a birdcage coil, instead of a surface coil, was used in order to provide a more homogeneous B_1 field. One of potential drawbacks of our approach is that if the concentration of IONPs is too low in the target site to make the local T_2 values lower enough than those of the surrounding tissues, the proposed method will be unable to sufficiently suppress the surrounding tissues and consequently detect the accumulated IONPs. Thus, to solve such an issue, future work will be conducted not only on optimizing pulse duration, designing tailored RF pulses using the Shinnar-Le Roux algorithm [30,31], but also on improving the delivery efficiency of IONPs using more robust coating materials. Another drawback is that the number of mice used in this study was not statistically very large, although this work consisted of in vivo, ex vivo, and histological experiments. During the experiments, we did find that the image quality and contrast for different mice were not solely affected by the saturation pulses, but also by many other factors, such as field shimming and anatomical variations among individual mice. Therefore, repetitions of both in vivo and ex vivo experiments will also be included in the further work to make the results more statistically sound. Nevertheless, in addition to improving detection specificity of IONPs, our method is potentially useful in clinical scans to enhance image contrast of short T_2 materials, such as cortical bones, teeth, and calcifications in various bio-tissues.

2.6 Conclusions

In conclusion, the SWIFT sequence in combination with two Gaussian pulses for suppression of long T_2 components can successfully enhance the contrast of RGD-IONP and therefore improve its detection specificity. Compared with the original SWIFT and SWIFT-1sat sequences, the SWIFT-2sat effectively suppressed long T_2 species while generating minimum influence on short T_2 species, including the RGD-IONPs inside the tumor.

2.7 Reference:

1. Mills PH, Hitchens TK, Foley LM, Link T, Ye Q, Weiss CR, Thompson JD, Gilson WD, Arepally A, Melick JA, Kochanek PM, Ho C, Bulte JW, Ahrens ET. Automated detection and characterization of SPIO-labeled cells and capsules using magnetic field perturbations. Magnetic resonance in medicine 2012;67(1):278-289.

2. Liu W, Frank JA. Detection and quantification of magnetically labeled cells by cellular MRI. European journal of radiology 2009;70(2):258-264.

3. Richards JM, Shaw CA, Lang NN, Williams MC, Semple SI, Macgillivray TJ, Gray C, Crawford JH, Alam SR, Atkinson AP, Forrest EK, Bienek C, Mills NL, Burdess A, Dhaliwal K, Simpson AJ, Wallace WA, Hill AT, Roddie PH, McKillop G, Connolly TA, Feuerstein GZ, Barclay GR, Turner ML, Newby DE. In vivo mononuclear cell tracking using superparamagnetic particles of iron oxide: feasibility and safety in humans. Circulation Cardiovascular imaging 2012;5(4):509-517.

4. Ramaswamy S, Schornack PA, Smelko AG, Boronyak SM, Ivanova J, Mayer JE, Jr., Sacks MS. Superparamagnetic iron oxide (SPIO) labeling efficiency and subsequent MRI tracking of native cell populations pertinent to pulmonary heart valve tissue engineering studies. NMR Biomed 2012;25(3):410-417.

5. Zhang LJ, Zhong XD, Wang LY, Chen HW, Wang YA, Yeh JL, Yang L, Mao H. T1 Weighted Ultrashort Echo Time Method for Positive Contrast Imaging of Magnetic Nanoparticles and Cancer Cells Bound With the Targeted Nanoparticles. Journal of Magnetic Resonance Imaging 2011;33(1):194-202.

6. Hasenpusch G, Geiger J, Wagner K, Mykhaylyk O, Wiekhorst F, Trahms L, Heidsieck A, Gleich B, Bergemann C, Aneja MK, Rudolph C. Magnetized aerosols comprising superparamagnetic iron oxide nanoparticles improve targeted drug and gene delivery to the lung. Pharmaceutical research 2012;29(5):1308-1318.

7. Singh I, Rana V. Iron oxide induced enhancement of mucoadhesive potential of Eudragit RLPO: formulation, evaluation and optimization of mucoadhesive drug delivery system. Expert opinion on drug delivery 2013.

8. Ji C, Miller PA, Miller MJ. Iron transport-mediated drug delivery: practical syntheses and in vitro antibacterial studies of tris-catecholate siderophore-aminopenicillin conjugates reveals selectively potent antipseudomonal activity. Journal of the American Chemical Society 2012;134(24):9898-9901.

9. Tyler DJ, Robson MD, Henkelman RM, Young IR, Bydder GM. Magnetic resonance imaging with ultrashort TE (UTE) PULSE sequences: technical considerations. Journal of magnetic resonance imaging : JMRI 2007;25(2):279-289.

10. Robson MD, Gatehouse PD, Bydder M, Bydder GM. Magnetic resonance: an introduction to ultrashort TE (UTE) imaging. Journal of computer assisted tomography 2003;27(6):825-846.

11. Idiyatullin D, Corum C, Park JY, Garwood M. Fast and quiet MRI using a swept radiofrequency. Journal of magnetic resonance 2006;181(2):342-349.

12. Idiyatullin D, Corum C, Moeller S, Garwood M. Gapped pulses for frequency-swept MRI. Journal of magnetic resonance 2008;193(2):267-273.

13. Garwood M. MRI of fast-relaxing spins. J Magn Reson 2013;229:49-54.

14. Zhou R, Idiyatullin D, Moeller S, Corum C, Zhang H, Qiao H, Zhong J, Garwood M. SWIFT detection of SPIO-labeled stem cells grafted in the myocardium. Magnetic resonance in medicine 2010;63(5):1154-1161.

15. Girard OM, Du J, Agemy L, Sugahara KN, Kotamraju VR, Ruoslahti E, Bydder GM, Mattrey RF. Optimization of iron oxide nanoparticle detection using ultrashort echo time pulse sequences: comparison of T1, T2*, and synergistic T1- T2* contrast mechanisms. Magnetic resonance in medicine 2011;65(6):1649-1660.

16. Rahmer J, Blume U, Bornert P. Selective 3D ultrashort TE imaging: comparison of "dual-echo" acquisition and magnetization preparation for improving short-T 2 contrast. Magma 2007;20(2):83-92.

17. Martirosian P, Schraml C, Springer F, Schwenzer NF, Wurslin C, Schick F, Deimling M. Positive Contrast MR Imaging of Tendons, Ligaments, and Menisci by Subtraction of

Signals From a Double Echo Steady State Sequence (Sub-DESS). Magnetic resonance in medicine 2013. DOI: 10.1002/mrm.24651

18. Rahmer J, Bornert P, Groen J, Bos C. Three-dimensional radial ultrashort echo-time imaging with T2 adapted sampling. Magnetic resonance in medicine 2006;55(5):1075-1082.

19. Larson PE, Gurney PT, Nayak K, Gold GE, Pauly JM, Nishimura DG. Designing long T2 suppression pulses for ultrashort echo time imaging. Magnetic resonance in medicine 2006;56(1):94-103.

20. Pauly JM, Conolly SM, Macovski A. Suppression of long T2 components for short T2 imaging. 1992; Proceedings of the 10th annual meeting of SMRI. New York, USA. p 330.

21. Du J, Bydder M, Takahashi AM, Carl M, Chung CB, Bydder GM. Short T2 contrast with three-dimensional ultrashort echo time imaging. Magnetic resonance imaging 2011;29(4):470-482.

22. Du J, Carl M, Bae WC, Statum S, Chang EY, Bydder GM, Chung CB. Dual inversion recovery ultrashort echo time (DIR-UTE) imaging and quantification of the zone of calcified cartilage (ZCC). Osteoarthritis and cartilage / OARS, Osteoarthritis Research Society 2013;21(1):77-85.

23. Du J, Carl M, Bydder M, Takahashi A, Chung CB, Bydder GM. Qualitative and quantitative ultrashort echo time (UTE) imaging of cortical bone. J Magn Reson 2010;207(2):304-311.

24. Springer F, Steidle G, Martirosian P, Grosse U, Syha R, Schabel C, Claussen CD, Schick F. Quick water-selective excitation of fast relaxing tissues with 3D UTE sequences. Magnetic resonance in medicine 2013. DOI: 10.1002/mrm.24684

25. Luhach I, Idiyatullin D, Lynch C, Corum C, Martinez G, Garwood M, and Gillies G. Rapid ex vivo imaging of PAIII prostate to bone tumor with SWIFT-MRI. 2013; Proceedings of the 21st annual meeting of ISMRM, Salt Lake City, UT.

26. Murase K, Tanki N. Numerical solutions to the time-dependent Bloch equations revisited. Magnetic resonance imaging 2011;29(1):126-131.

27. Jackson JI, Meyer CH, Nishimura DG, Macovski A. Selection of a Convolution Function for Fourier Inversion Using Gridding. Ieee T Med Imaging 1991;10(3):473-478.

28. Gonzalez RC, Woods RE, Eddins SL. Digital Image processing using MATLAB. Upper Saddle River, N. J.: Pearson Prentice Hall; 2004.

29. Larson PE, Gurney PT, Nayak K, Gold GE, Pauly JM, Nishimura DG. Designing long-T2 suppression pulses for ultrashort echo time imaging. Magnetic resonance in medicine 2006;56(1):94-103.

30. Lee KJ. General parameter relations for the Shinnar-Le Roux pulse design algorithm. J Magn Reson 2007;186(2):252-258.

31. Pauly J, Le Roux P, Nishimura D, Macovski A. Parameter relations for the Shinnar-Le Roux selective excitation pulse design algorithm. IEEE Trans Med Imaging 1991;10(1):53-65.

Table

Table 2.1: SNR and CNR for the phantom study

		Regular SWIFT	SWIFT-1sat		SWIFT-2sat			
			2 ms	4 ms	8 ms	16 ms	24 ms	32 ms
SNR	IONPs	27.5±2.8	21.5±2.3	27.8±3.2	14.0±1.5	21.7±2.1	24.4±2.4	26.8±2.6
	Gel	21.2±2.0	11.1±1.2	22.0±2.1	6.1±0.8	6.0±0.8	5.8±0.8	7.4±1.0
	Oil	32.0±5.3	20.7±3.4	28.6±5.2	17.1±1.7	15.5±1.4	14.0±1.3	13.6±1.4
CNR	IONPs-Gel	6.3	10.4	5.8	7.9	15.7	18.6	19.4
	IONPs-Oil	-4.5	0.8	-0.8	-3.1	6.2	10.4	13.2

Table 2.1 presents the mean and standard deviation of the SNR as well as the resulted CNR of the IONP suspension, the agar gel, and the vegetable oil in the phantom, acquired by using different scan protocols. For the SWIFT-2sat sequence, the fat saturation was fulfilled by using a fixed 8 ms Gaussian pulse with the flip angle of 135°.

Figures

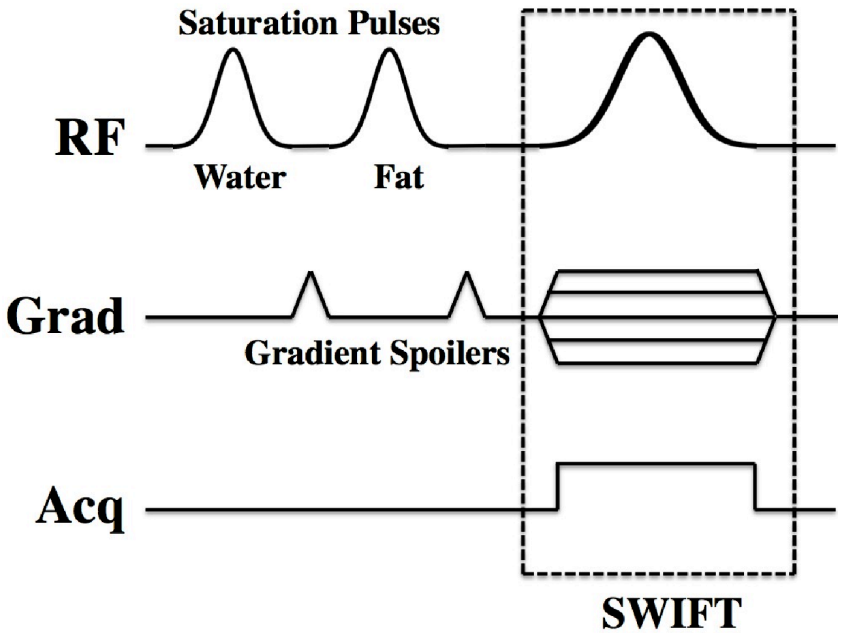

Figure 2.1. This figure illustrates the proposed SWIFT-2sat sequence. Two saturation pulses, placed at the water and fat resonant frequencies, are embedded in the regular SWIFT sequence to suppress long T_2 and fat signals. Gradient spoilers follow each saturation pulse to dephase the excited signals.

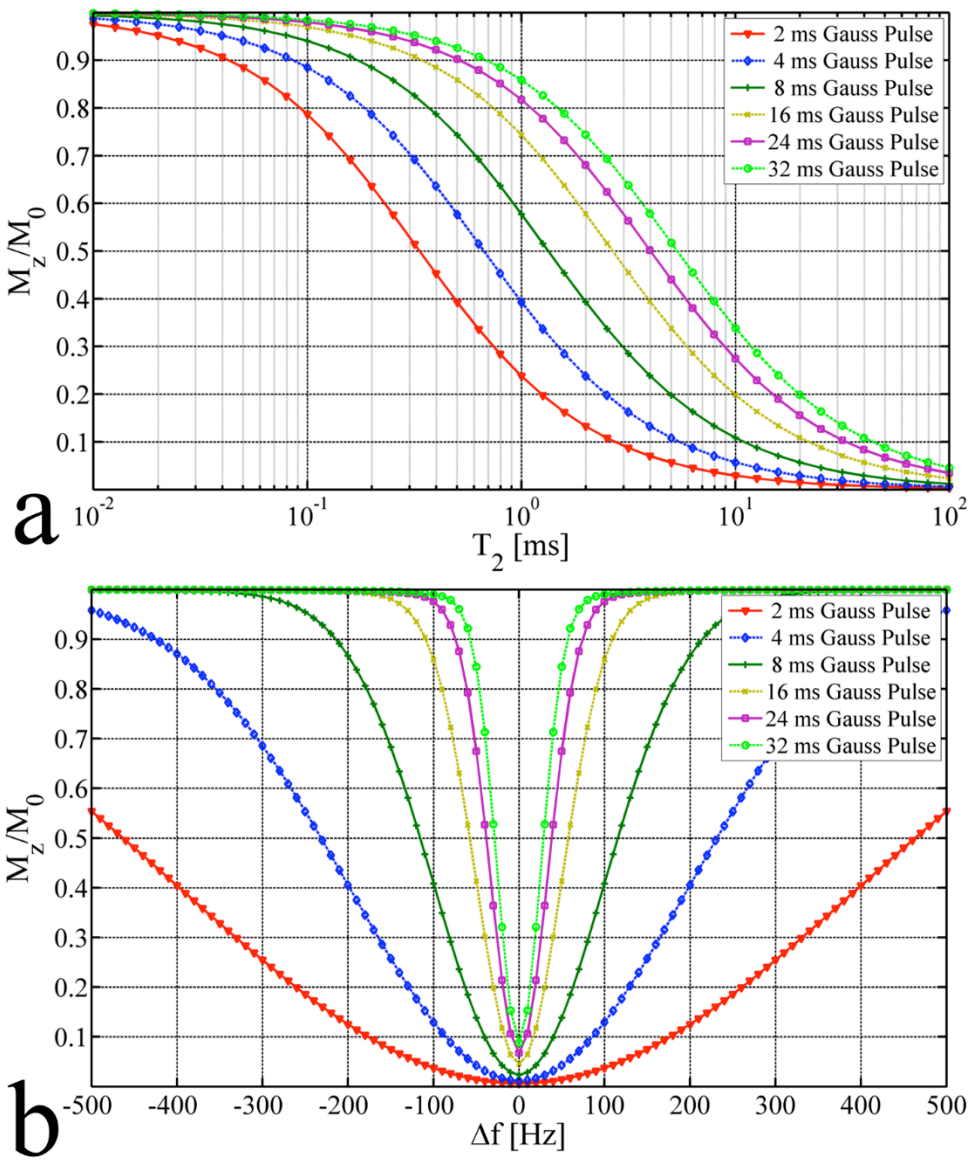

Figure 2.2. The ratios of the longitudinal magnetization, M_z, and the initial magnetization, M_0, were calculated after a 90° Gaussian pulse using the Bloch equation simulation. (a) Without any off-resonance effect, the ratio was plotted as a function of T_2 for different pulse lengths. (b) By setting T_2 to 50 ms, the ratio was plotted as a function of frequency offset for different pulse lengths. For all the two situations, T_1 is set as 1000 s.

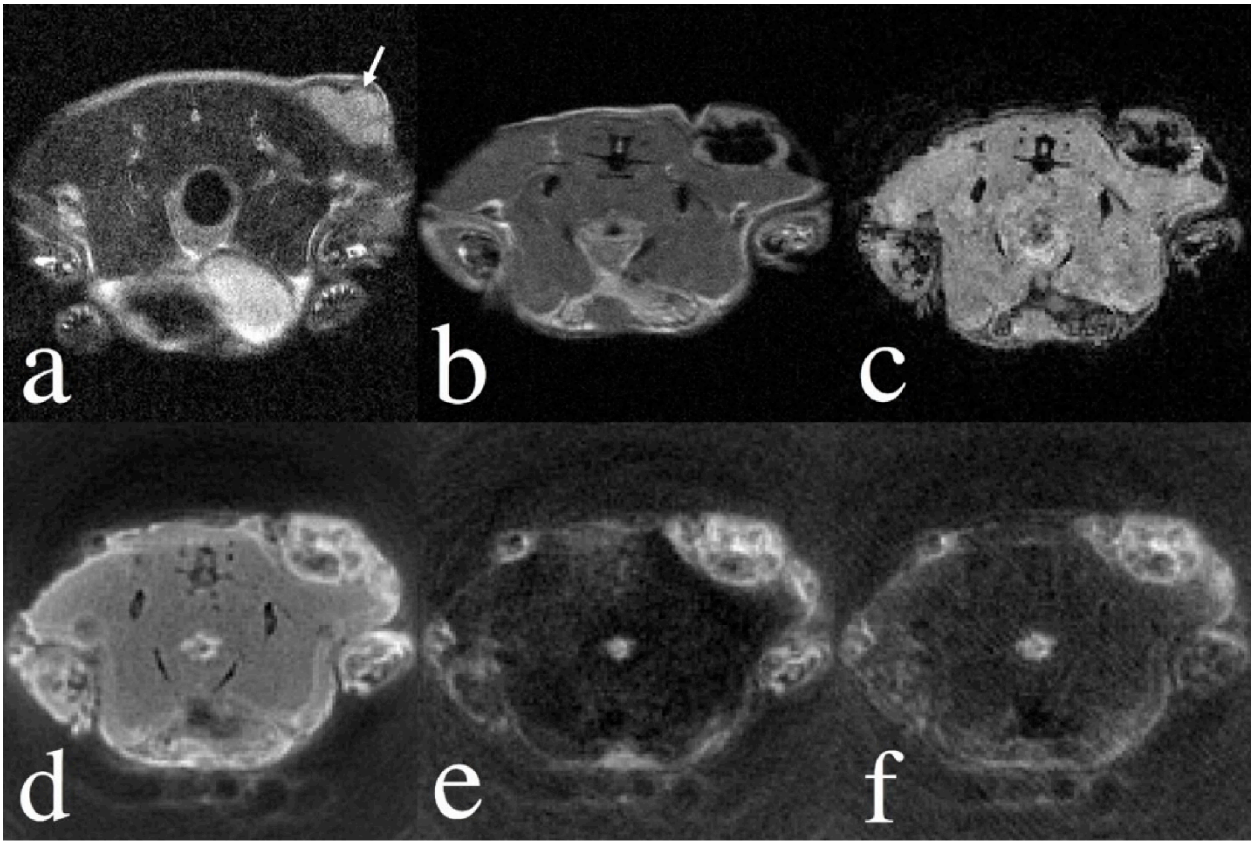

Figure 2.3. This figure presents the in vivo MR images before and after intra-tumor injection of the aqueous IONP suspension. (a) The pre-injection image was acquired using the fast spin echo sequence with TE = 30 ms. The tumor is indicated by the arrow. Immediately after the injection, the mouse was scanned using (b) the fast spin echo sequence with TE = 12 ms, (c) the spoiled gradient echo sequence with TE = 3.15 ms, (d) the SWIFT sequence with TE = 3.9 μs, (e) the SWIFT-2sat sequence with two 8 ms Gaussian pulses, and (f) the SWIFT-1sat sequence with one 2 ms Gaussian pulse.

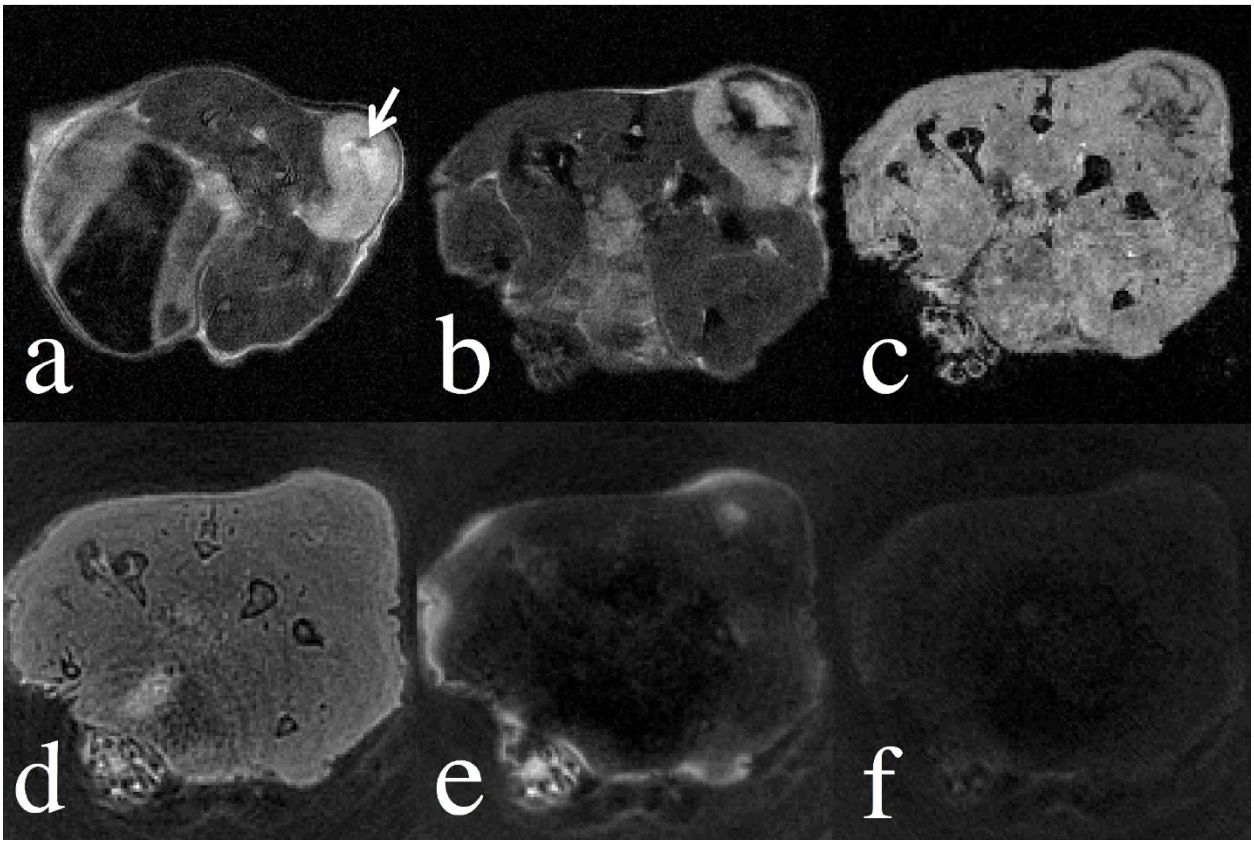

Figure 2.4. This figure presents in vivo MR images of the mouse before and after the intravenous injection of the RGD-IONPs. (a) The pre-injection was acquired using the fast spin echo sequence with TE = 30 ms. The arrow indicates a presumably necrotic core inside the tumor. After 24 hours of the intravenous injection, the mouse was scanned using (b) the fast spin echo sequence with TE = 30 ms, (c) the spoiled gradient echo sequence with TE = 3.15 ms, and (d) the SWIFT sequence with TE = 3.9 μs. To suppress tissues with long T_2, (e) the SWIFT-2sat sequence with two 8 ms Gaussian pulses and (f) the SWIFT-1sat sequence with one 2 ms Gaussian pulse were implemented.

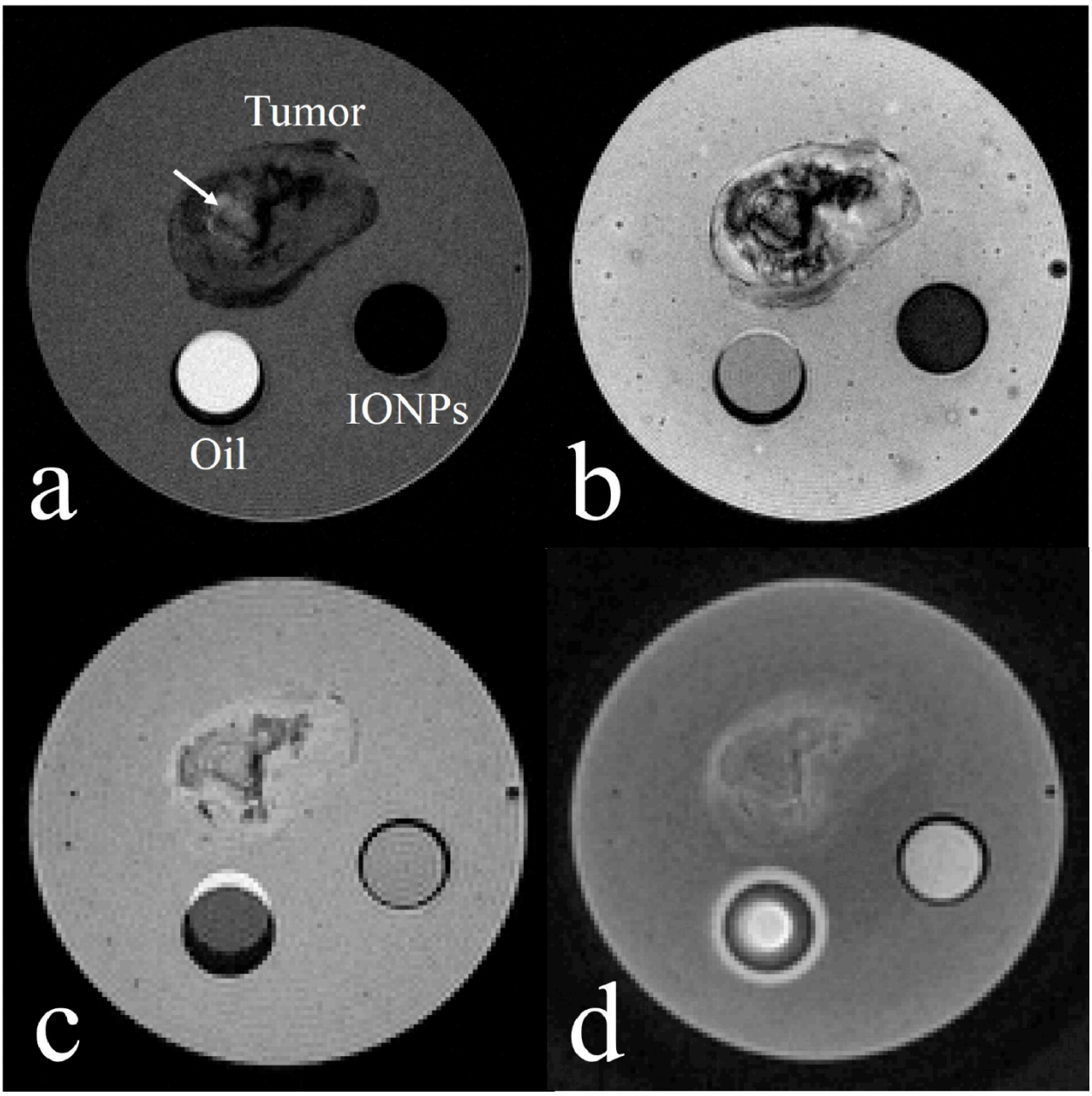

Figure 2.5. This figure shows the MR images of the phantom using different scan protocols. The phantom consists of a vial of aqueous suspensions of 1 mM IONPs, a vial of vegetable oil, and the tumor specimen with the delivered RGD-IONPs. The images were acquired using (a) the spin echo sequence with TE = 30 ms, (b) the spoiled gradient echo sequence with TE = 10.84ms, (c) the fast spoiled gradient echo sequence with TE = 3.15 ms, and (d) the SWIFT sequence with TE = 3.9 μs.

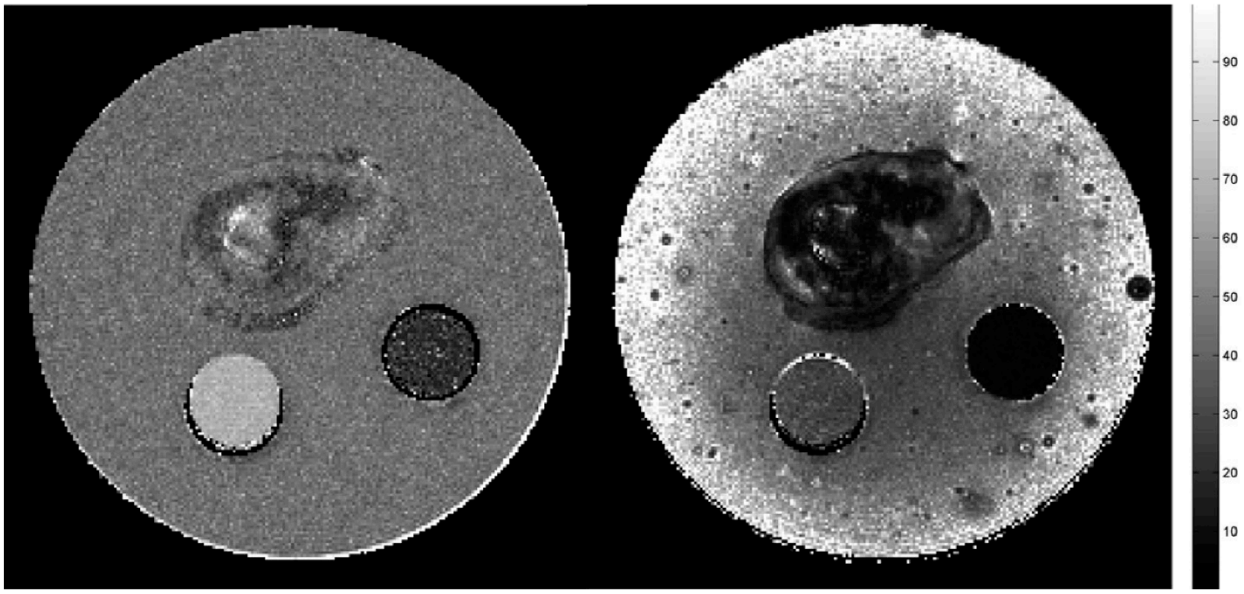

Figure 2.6. This figure shows the (a) T_2 and (b) T_2^* maps of the phantom. The scale bar is in the unit of [ms].

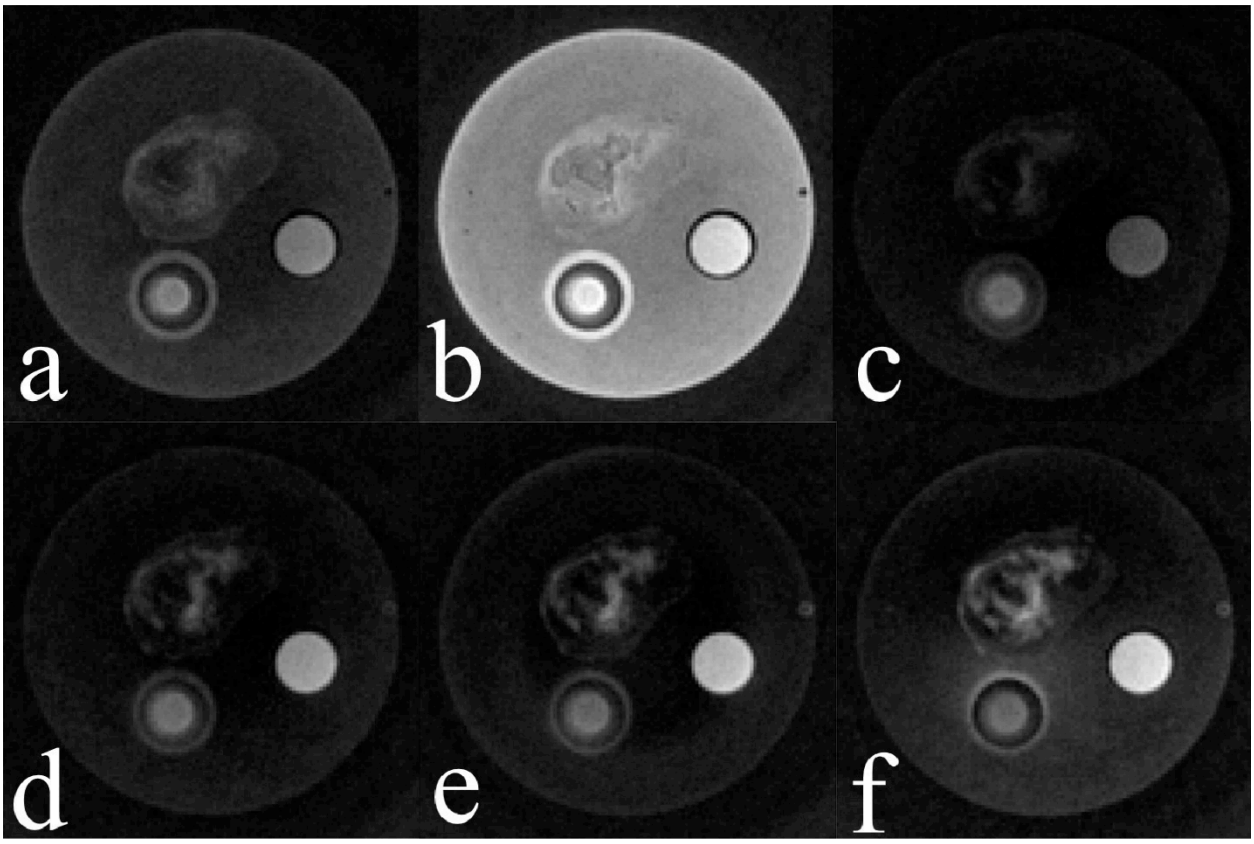

Figure 2.7. This figure shows the phantom images obtained by using different suppression methods. (a) and (b) were acquired using the SWIFT-1sat sequence with 2 ms and 4 ms Gaussian pulses, respectively. For the images acquired using the SWIFT-2sat sequence, the first Gaussian pulse was set to (c) 8 ms, (d) 16 ms, (e) 24 ms, (f) and 32 ms to suppress long T_2 species, respectively. And the second Gaussian pulse was fixed to 8 ms for fat suppression.

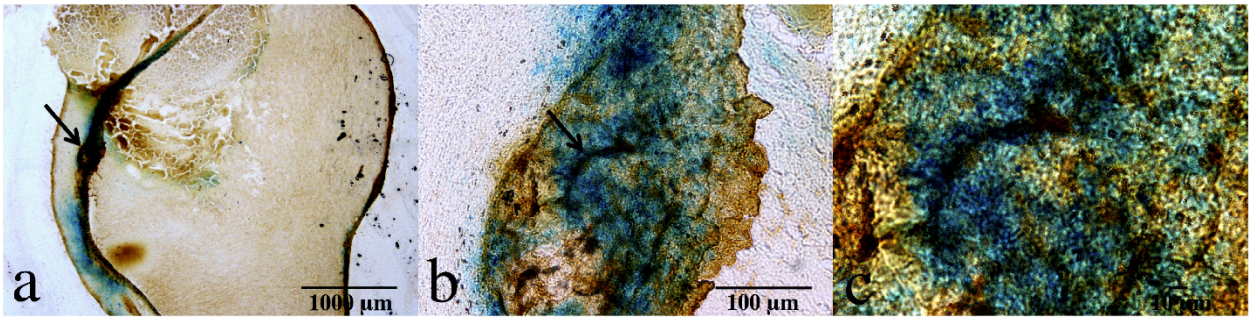

Figure 2.8. This figure presents the histological studies of the tumor tissues with the delivered RGD-IONPs. Figures (b) and (c) show magnified areas of the arrow-pointed regions in (a) and (b), respectively. The results of the Prussian blue staining and the murine β_3 staining indicates that the tumor targeting was mainly mediated by RGD-integrin interactions, and the highlighted regions in the MR images acquired by using SWIFT-2sat and SWIFT-1sat are more likely due to the IONPs in the tumor.

CHAPTER 3

MR IMAGING OF WATER AND FAT IN CORTICAL BONE: A PRELIMINARY STUDY[2]

[2] Wang, L., Meng, Q., and Zhao, Q. To be submitted to Magnetic Resonance in Medicine.

3.1 Abstract

Bone diseases have influenced millions of patients' lives. However, diagnostic MR imaging of bones still remains a challenge, as the bone, especially cortical bone, has a relatively short T_2 or T_2* values, which results in a fast MR signal decay. In this work, we aim to conduct a preliminary study to image free water and fat stored in a sample of a swine humerus bone by using the fast spin echo (FSE) sequence and the sweep imaging using Fourier transformation (SWIFT) sequence. To get a qualitative mapping of free water distribution in the bone, MR scans were performed before and after dehydration of the bone sample, with fat and water saturation applied. The results demonstrate that the SWIFT sequence has an advantage on visualizing cortical bone compared with the FSE sequence, especially on visualizing bound water component in cortical bone.

3.2 Introduction

Cortical bone is a hierarchically organized biomaterial that consists of mineral (about 43% by volume), organic matrix (about 35%) and water (about 22%) (1). Bone diseases, such as osteoporosis, affect millions of patients in the USA (2-4), so it is of critical importance to assess cortical bone for clinical diagnoses. As one of advanced imaging technologies, magnetic resonance imaging (MRI) has been widely used for this purpose. However, because of its short T_2 and T_2* values, cortical bone is usually regarded as 'invisible' for MRI, when conventional clinical pulse sequences are implemented (5). It has been reported that the water component in cortical bone can be classified into two types: free water and bound water, which have different contributions to the mechanical properties of cortical bone (6). It remains a big challenge to image bound water, however, free water in cortical bone has a short T_2* value but a relatively

long T_2 value, traditional fast spin echo sequences have been successfully applied to visualize this fraction of water by using a short echo time (TE) (6-9). Additionally, fat in cortical bone has long T_2 and T_2* values, which allows the usage of conventional pulse sequences for imaging. But the chemical shift between water and fat may result in partial volume artifact and blurred images.

In recent years, the development of the ultrashort echo time (UTE) sequence and the sweep imaging with Fourier transformation (SWIFT) sequence (10-12) enables the capability of MRI to image materials with very short T_2* values, which can't be fulfilled by conventional pulse sequences. For example, cortical bone, as one of short T_2* materials, has been studied using the UTE sequence to visualize the bound water and measure the T_1 and T_2* values of cortical bone (13-20). Furthermore, with the help of magnetization preparation, different types of components in cortical bone, such as water and fat, have been visualized separately using the UTE sequence to improve detection specificity of the different components (13-20).

In this work, we aimed to demonstrate the capability of the SWIFT sequence with magnetization preparation to visualize water and fat in a swine cortical bone. The fast spin echo (FSE) sequence, which has been widely used in clinical applications, was also applied for comparison.

3.3 Materials and method

3.3.1 Sample preparation

A 2 cm-in-length bone segment was cut from a fresh swine humerus bone and used in this study. In order to visualize the water and fat components in the cortical bone, the fresh bone segment was immerged into a 2% agar gel to prevent water loss, and then MRI scans were followed

immediately after the agar gel became solid. After the MRI scans, the bone segment was removed from the agar gel and the bone marrow was removed. To remove free water from the bone, dehydration was conducted by first immersing the humerus bone into 99% ethanol for 24 hours, and then air-dried at about 500˚C for 20 minutes. The dehydrated bone segment was placed into Fomblin solution (California vacuum technology, Fremont, CA) to reduce susceptibility effect and improve field homogeneity for the following MRI scans.

3.3.2 MR experiments

All MR scans were conducted using a 7 T Varian Magnex small animal scanner (Agilent Technologies, Santa Clara, CA) at the Bio-imaging Research Center, the University of Georgia. The scanner has a maximum gradient strength of 440 mT/m. High-pass birdcage coils (3.8 cm / 7.2 cm diameter) were used for both RF transmission and signal reception. During imaging, the fresh bone was placed vertically (with its long axis perpendicular to the B_0 field) at the iso-center of magnet bore. The dehydrated bone was placed in a plastic container filled with Fomblin with the bone's long axis parallel to the B_0 field.

A 2D FSE sequence was first utilized to generate morphologic images of the fresh swine humerus bone with the following parameters: TR/TE = 3 s / 10.25 ms, echo train length = 8, spectral width of acquisition (sw) = 100 kHz, field-of-view (FOV) = 7 cm, slice thickness (thk) = 1 mm, image size = 512^2, 10 coronal slices, 4 averages. Then the bone was scanned with the SWIFT sequence: a gapped hyperbolic secant pulse, with the dimensionless shape factor n = 1 and truncation factor $\beta = 7.6$, was implemented to excite an 8° flip angle. The pulse was divided into 256 segments, and each segment consisted of 3 μs pulse element and 9 μs free induction decay for data sampling. The dead time between the end of a pulse element and the beginning of

data sampling was set to 2.9 μs, referred to as the effective TE for SWIFT. The TR of SWIFT was set to 4 ms. And the pulse bandwidth (bw) and the spectral width were both set to 83.3 kHz in this study. The entire 3D radial k-space consisted of 64,000 spokes, and covered a spherical FOV with the radius equal to 70 mm. Three averages were used to increase the signal-to-noise ratio (SNR). At the beginning of the SWIFT sequence, 512 dummy scans were implemented to achieve a steady state. For both the FSE and SWIFT sequences, in order to discriminate water and fat components in the fresh humerus bone, fat and water suppressions were performed using a 4 ms Gaussian pulse with 120° / 90° flip angles, followed by a 2 ms gradient crusher, respectively.

After dehydration, the humerus cortical bone was scanned again using the FSE and SWIFT sequences with the same scan parameters. During the scans, a vial of water (0.3 mL) was attached to the container that held the bone as a reference. Fat and water saturations were also implemented to differentiate water and fat components.

3.3.3 Data processing

Images acquired using Cartesian sampling were obtained directly from fast Fourier transforms of the k-space data using Matlab (MathWorks, Natick, MA). The raw data of the SWIFT scans were first processed using house-developed code written in LabVIEW (National Instruments, Austin, TX), and then interpolated with a Kaiser-Bessel function onto a Cartesian grid utilizing compiled Matlab mex code, resulting in the image size = 256^3 (21). Fast Fourier transforms of the post-processed raw data were performed to generate the complex SWIFT images at last.

3.4 Results

Figure 3.1 shows the original, fat- and water-suppressed MR images of the fresh humerus bone. Figure 3.1(a) is a coronal image acquired by using the regular FSE sequence. Because of chemical shift between water and fat, image artifacts, such as the voxel shift of the canals in the bone marrow and indicated by the arrows, can be observed along the frequency encoding (vertical) direction in Figure 3.1(a). In Figure 3.1(b), fat signal was suppressed by a RF pulse. Because the echo time of the FSE sequence was too long to acquire the signal from bound water, the T_2 of which was usually less than 1 ms (14,19), only the free water signal can be observed in Figure 3.1(b). Inside the bone marrow, the cross-section of the canals was highlighted with positive contrast, indicating the canals mainly contained free water components. And it also has been noticed that artifacts caused by chemical shift were removed in this image, resulting in clear boundaries of the canals and other components. With fat saturation, the distribution of free water, represented as white dots, in the cortical bone can now be determined in Figure 3.1(b) in the area enclosed by the dashed curve, but the signal intensity is weak. Figure 3.1(c) shows the fat distribution in the humerus bone by using water suppression. The bone marrow canals are now shown as dark or black holes in the image, and the fat component in the cortical bone is surrounded by the dashed curve. Figures 3.1(d) and 3.1(g) are the coronal and axial images of the humerus bone obtained using the regular SWIFT sequence. Their relative positions are indicated by the horizontal, dashed lines in the two figures. Since the SWIFT sequence utilizes the radial k-space sampling, the artifacts caused by chemical shift exist in all directions surrounding the canals and bone marrow, resulting in more blurring artifact compared with Figure 3.1(a). Figures 3.1(e) and 3.1(h) illustrates the water distribution in the humerus bone with fat suppression. In contrast to Figures 3.1(d) and 3.1(g), the image blurring effect was removed, and clear

boundaries of different components can be depicted. For example, in Figure 3.1(h), as indicated by the arrow, the canals were clearly delineated. Additionally, compared with Figure 3.1(b), more water components can be better viewed inside the cortical bone, enclosed by the dashed curves, benefiting from the ultra-short echo time of the SWIFT sequence. For example, a bright outline surrounding the bone marrow indicated by the arrow in Figure 3.1(e), can be found, possibly due to a thin layer of fluid, but this was not shown in Figure 3.1(b). Figures 3.1(f) and 3.1(i) show the fat distribution after water suppression. The outer boundary of fat inside the cortical bone was traced by the dashed curves, and tissues consisting of water, such as the canals, were suppressed and appeared dark.

Figure 3.2 presents the original, fat- and water-suppressed MR images of the dehydrated cortical bone. Figures 3.2(a) to 3.2(c) are the coronal images acquired using the FSE sequence. A vial of water, pointed by the arrow in Figure 3.2(a), was shown as a reference. Since the bound water has a T_2 value in the scale of hundreds microsecond (14,19,20), only can the fat component and the vial of water be seen in the FSE image. In Figure 3.2(b), fat suppression was applied during the scan, and the water signal from the vial remained the same. However, there still remained little signal from the fat in the cortical bone, which was probably because the B_1 field of the saturation RF pulse was not homogeneous. The contrast-to-noise ratio (CNR) between the two rectangular boxes is about zero, which indicates that it is impossible to detect bound water in the cortical bone based on the FSE images. In Figure 3.2(c), the signal from the water vial was suppressed by using the water saturation RF pulse, and the residual fat has a similar distribution as observed in Figure 3.2(a). Figures 3.2(d) and 3.2(g) illustrate the SWIFT images of the cortical bone on coronal and axial slices, and their relative positions are indicated by the horizontal, dashed lines in the two figures. The cortical bone became visible and its

boundary was delineated from the background by the dashed curves. Bubble-like blurring caused by chemical shift is pointed by the arrows in the two images, in contrast to Figure 3.2(a). With fat saturation, Figures 3.2(e) and 3.2(h) mainly illustrate the bound water component of the cortical bone, which still allows one to depict the inner and outer boundaries of the cortical bone. The CNR between the two rectangular boxes is about 17.4, much higher compared with the FSE images. With water saturation, the signal from water vial was completely suppressed in Figure 3.2(f), and fat distribution in the cortical bone was depicted in Figures 3.2(f) and 3.2(i).

3.5 Discussion

In this study, a sample of a swine humerus bone was scanned before and after dehydration using the FSE and SWIFT sequences. Fat and water saturations were conducted to differentiate water and fat distributions in the bone and bone marrow. The results qualitatively demonstrated distribution of free water, bound water and fat. Further comparison of the images before and after dehydration indicates that most of the water component, traced by the dashed curves in Figures 3.1(b), 3.1(e) and 3.1(f), disappeared in Figures 3.2(b), 3.2(e) and 3.2(f). We hypothesize these are free water component.

The free water and fat have a relatively long T_2 and T_2* values, so that visualization of them is not beyond the capability of regular pulse sequences, such as the FSE sequence. However, by shortening the echo time, the SWIFT sequence has an additional advantage of catching signal from short T_2* materials. Furthermore, it is beyond the capability of the FSE sequence to image the bound water in the cortical bone, and the bone boundary can't even be delineated in Figures 3.2(a) and 3.2(b). In contrary, demonstrated by the CNR values, the dehydrated cortical bone can

be visualized and detected from the background by using the SWIFT sequence, whose echo time is in a few microseconds.

In addition to use the SWIFT sequence, in order to image the bound water in cortical bone, one has to suppress signals from free water and fat, otherwise the signals from free water and fat are too strong to make bound water visible, which is demonstrated by comparing Figures 3.1 and 3.2. In this work, we hydrated the cortical bone in order to investigate distribution of the bound water positively. But such an objective may also be achieved by implementation of RF pulses to suppress free water and fat simultaneously, with a drawback of suffering even lower SNR.

Another advantage of the SWIFT sequence is that it is quieter compared with the FSE sequence. Since the SWIFT sequence uses a radial k-space data sampling, thus the gradients change smoothly to sweep the entire k-space. But the raw data has to be converted into a Cartesian frame before the image reconstruction (12,21). A drawback of this procedure is to introduce some image artifacts into the SWIFT images, such as the bulleye artifact, especially when image SNR is low. An example can be found in Figures 3.1(e) and 3.2(e). This systematic error is an intrinsic property of the radial k-space data sampling, which cannot be entirely eliminated when using the SWIFT sequence.

3.6 Conclusions

Fresh and dehydrated swine humerus bone was imaged by using the FSE and SWIFT sequences, and water and fat components of the cortical bone were visualized in the MR images. The SWIFT sequence demonstrated its unique advantage over the FSE sequence on acquiring signal from materials of short T_2* values, i.e., bound water in cortical bone in this study.

3.7 References

1. Wehrli FW, Song HK, Saha PK, Wright AC. Quantitative MRI for the assessment of bone structure and function. NMR in biomedicine 2006;19(7):731-764.

2. NIH Consensus Development Panel on Osteoporosis Prevention, Diagnosis, and Therapy, March 7-29, 2000: highlights of the conference. Southern medical journal 2001;94(6):569-573.

3. Schneider EL, Guralnik JM. The aging of America. Impact on health care costs. JAMA : the journal of the American Medical Association 1990;263(17):2335-2340.

4. Kanis JA. Assessment of fracture risk and its application to screening for postmenopausal osteoporosis: synopsis of a WHO report. WHO Study Group. Osteoporosis international : a journal established as result of cooperation between the European Foundation for Osteoporosis and the National Osteoporosis Foundation of the USA 1994;4(6):368-381.

5. Reichert IL, Robson MD, Gatehouse PD, He T, Chappell KE, Holmes J, Girgis S, Bydder GM. Magnetic resonance imaging of cortical bone with ultrashort TE pulse sequences. Magnetic resonance imaging 2005;23(5):611-618.

6. Nyman JS, Ni Q, Nicolella DP, Wang X. Measurements of mobile and bound water by nuclear magnetic resonance correlate with mechanical properties of bone. Bone 2008;42(1):193-199.

7. Horch RA, Nyman JS, Gochberg DF, Dortch RD, Does MD. Characterization of 1H NMR signal in human cortical bone for magnetic resonance imaging. Magnetic resonance in medicine 2010;64(3):680-687.

8. Horch RA, Gochberg DF, Nyman JS, Does MD. Clinically compatible MRI strategies for discriminating bound and pore water in cortical bone. Magnetic resonance in medicine 2012;68(6):1774-1784.

9. Ong HH, Wright AC, Wehrli FW. Deuterium nuclear magnetic resonance unambiguously quantifies pore and collagen-bound water in cortical bone. Journal of bone and mineral research : the official journal of the American Society for Bone and Mineral Research 2012;27(12):2573-2581.

10. Robson MD, Gatehouse PD, Bydder M, Bydder GM. Magnetic resonance: an introduction to ultrashort TE (UTE) imaging. Journal of computer assisted tomography 2003;27(6):825-846.

11. Idiyatullin D, Corum C, Moeller S, Garwood M. Gapped pulses for frequency-swept MRI. Journal of magnetic resonance 2008;193(2):267-273.

12. Idiyatullin D, Corum C, Park JY, Garwood M. Fast and quiet MRI using a swept radiofrequency. Journal of magnetic resonance 2006;181(2):342-349.

13. Bae WC, Chen PC, Chung CB, Masuda K, D'Lima D, Du J. Quantitative ultrashort echo time (UTE) MRI of human cortical bone: correlation with porosity and biomechanical properties. Journal of bone and mineral research 2012;27(4):848-857.

14. Biswas R, Bae W, Diaz E, Masuda K, Chung CB, Bydder GM, Du J. Ultrashort echo time (UTE) imaging with bi-component analysis: bound and free water evaluation of bovine cortical bone subject to sequential drying. Bone 2012;50(3):749-755.

15. Du J, Bydder GM. Qualitative and quantitative ultrashort-TE MRI of cortical bone. NMR in biomedicine 2013;26(5):489-506.

16. Du J, Carl M, Bydder M, Takahashi A, Chung CB, Bydder GM. Qualitative and quantitative ultrashort echo time (UTE) imaging of cortical bone. Journal of magnetic resonance 2010;207(2):304-311.

17. Du J, Hamilton G, Takahashi A, Bydder M, Chung CB. Ultrashort echo time spectroscopic imaging (UTESI) of cortical bone. Magnetic resonance in medicine 2007;58(5):1001-1009.

18. Du J, Hermida JC, Diaz E, Corbeil J, Znamirowski R, D'Lima DD, Bydder GM. Assessment of cortical bone with clinical and ultrashort echo time sequences. Magnetic resonance in medicine 2012.

19. Kokabi N, Bae W, Diaz E, Chung CB, Bydder GM, Du J. Ultrashort TE MR imaging of bovine cortical bone: the effect of water loss on the T1 and T2* relaxation times. Magnetic resonance in medicine 2011;66(2):476-482.

20. Li S, Chang EY, Bae WC, Chung CB, Gao S, Bao S, Bydder GM, Hua Y, Du J. Ultrashort echo time bi-component analysis of cortical bone-a field dependence study. Magnetic resonance in medicine 2013.

21. Jackson JI, Meyer CH, Nishimura DG, Macovski A. Selection of a convolution function for Fourier inversion using gridding [computerised tomography application]. IEEE transactions on medical imaging 1991;10(3):473-478.

Figures

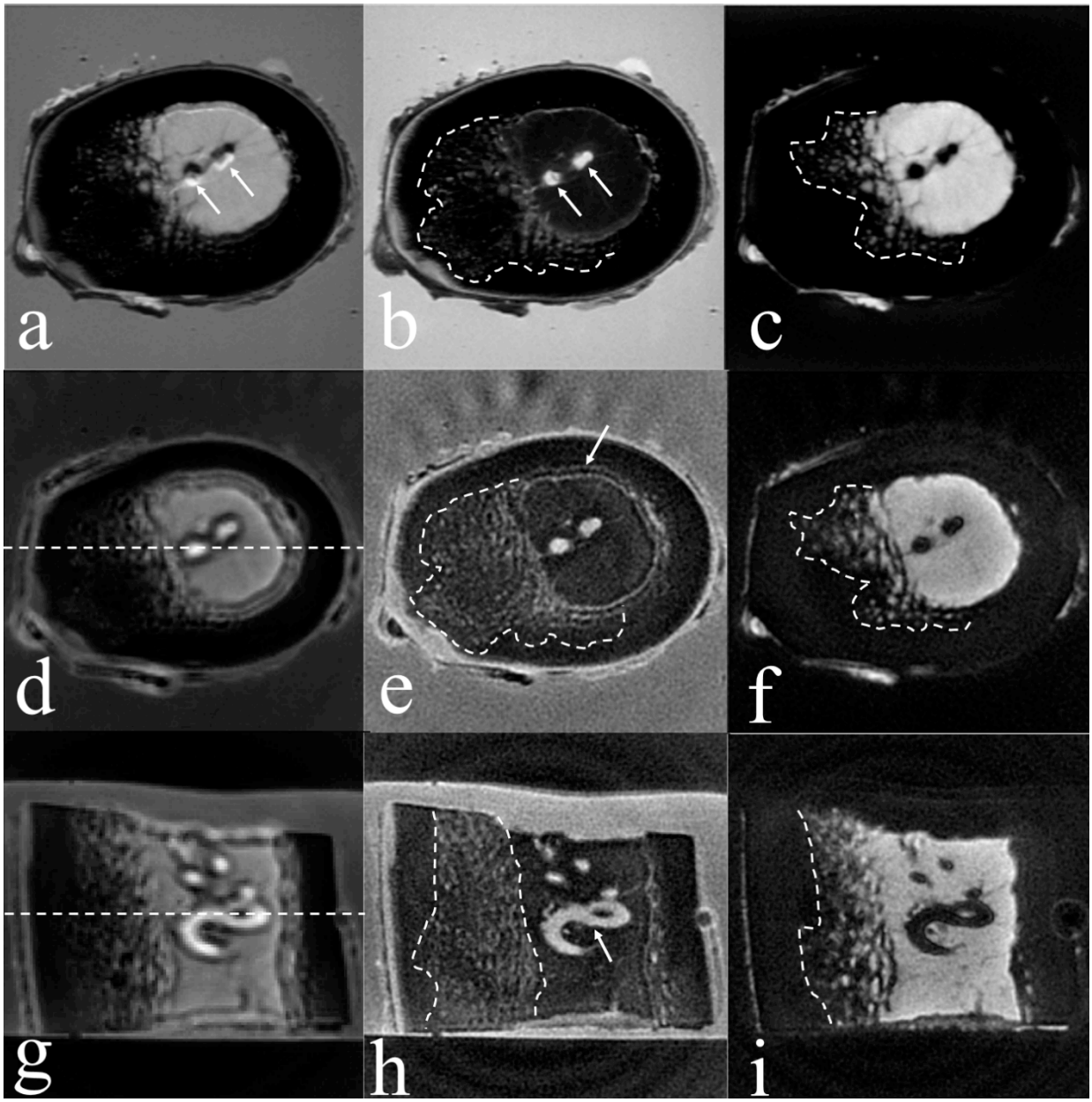

Figure 3.1. This figure shows the images of a fresh humerus bone acquired using the FSE sequence (first row) and the SWIFT sequence (second and third rows). Fat and water suppressions were applied for the images in the second and third columns, respectively.

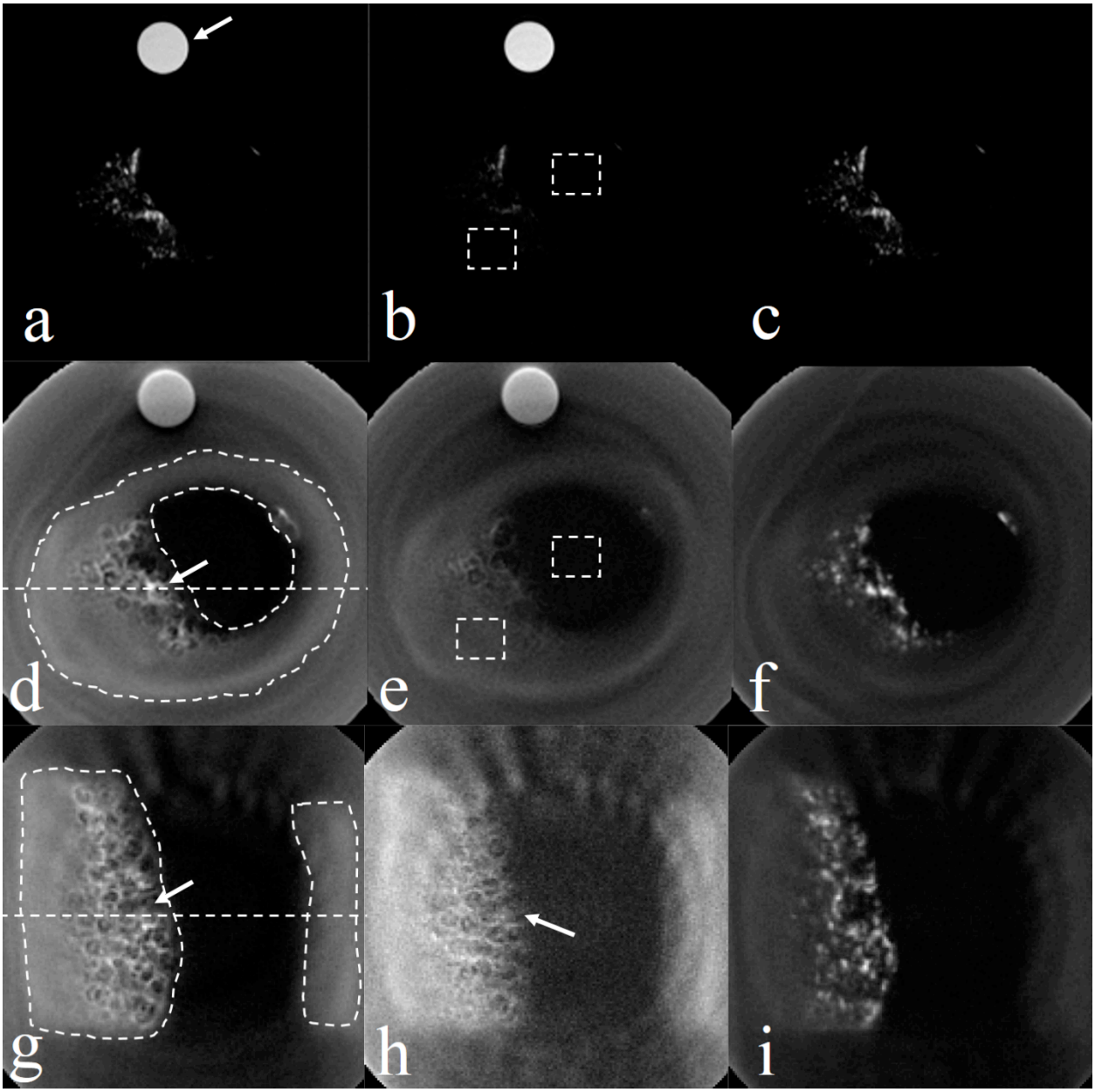

Figure 3.2. This figure shows the images of a dehydrated humerus bone and a vial of water acquired using the FSE sequence (first row) and the SWIFT sequence (second and third rows). Fat and water suppressions were applied for the images in the second and third columns, respectively.

CHAPTER 4

IN VIVO QUANTIFICATION OF SPIO NANOPARTICLES FOR CELL LABELING BASED ON MR PHASE GRADIENT IMAGES[3]

[3] Wang, L., Potter, W., and Zhao, Q. Submitted to Contrast Media & Molecular Imaging on 10/03/2013.

4.1 Abstract

Along with the development of modern imaging technologies, contrast agents play increasingly important roles in both clinical applications and scientific researches. Super-paramagnetic iron oxide (SPIO) nanoparticle, a negative contrast agent, has been extensively used in magnetic resonance imaging (MRI), such as *in vivo* labeling and tracking of cells. However, there still remain many challenges, such as *in vivo* quantification of SPIO nanoparticles. In this work, a novel MR phase gradient based method was proposed to quantify the SPIO nanoparticles. As a calibration, a phantom experiment using known concentrations (50, 75, 100, and 125 μg/ml) of SPIO was first conducted to verify the proposed quantification method. In a following *in vivo* experiment, C6 glioma cells labeled with SPIO nanoparticles were implanted into flanks of four mice, which were scanned 1 to 3 days post-injection for *in vivo* quantification of SPIO concentration. The results showed that the concentration of SPIO nanoparticles can be determined in both phantom and *in vivo* experiments using the developed MR phase gradients approach.

4.2 Introduction

Super-paramagnetic iron oxide (SPIO) nanoparticle is one of T_2 shortening contrast agents that have been widely used in magnetic resonance imaging (MRI), providing attractive benefits in both scientific researches and clinical diagnoses, such as *in vivo* cell labeling and MRI tracking (1-4). Under the strong magnetic field of MRI, the magnetic dipole field effect induced by the SPIO nanoparticles is usually much larger than the nanoparticles themselves, which enables *in vivo* tracking and molecular imaging of cells labelled with SPIO nanoparticles (1-4).

Beyond the detection of the SPIO labelled cells, quantitative studies attract a lot of attention from researchers and clinicians. At a relatively low iron concentration, a T_2* measurement is usually carried out to quantify the SPIO nanoparticles, benefiting from the linear relationship between R_2* and iron concentration. However, in the presence of a high iron concentration, MR signals will decay very fast due to incoherent phases among the excited spins, resulting in the relaxometry based approaches almost impossible when using regular pulse sequences, such as the gradient echo sequence. Recently, Wang et al developed a T_1 mapping method to quantify highly concentrated SPIO nanoparticles using the sweep imaging using Fourier transformation (SWIFT) sequence (5). However, *in vivo* applications have not been demonstrated yet.

By taking advantage of the induced phase perturbation, quantitative susceptibility mapping (QSM) method allows one to estimate the susceptibility of the SPIO nanoparticles without worrying about signal void inside the accumulated region of the SPIO nanoparticles (6-9). However, the original phase map is not continuous and has fringes, since it can only evolve in the principle range between $[-\pi, \pi)$. One common disadvantage of many proposed QSM methods is that one has to unwrap the raw phase images before any further data processing is done. But phase unwrapping algorithms are usually nontrivial and time-consuming for a three-dimensional (3D) phase image used for susceptibility quantification.

One possible solution to avoid the phase unwrapping step is to utilize the spatial gradients of the phase image, which have been demonstrated to be continuous, smooth, and without any fringe (10,11). Compared with the original phase image, phase gradient images can improve the detection specificity of the accumulated SPIO nanoparticles, as the calculation of the spatial gradients functions like a high-pass filter and enhance the image contrast of the region, where phase evolves fast (10,11).

In addition to SPIO nanoparticles, the MR phase can also be induced by many other sources, including chemical shift, physiological motion (breathing, cardiac motion, blood flow), eddy currents, Maxwell terms during the phase encoding, initial phase, etc (9,12). Here we denote these sources as the "external sources" for convenience. Although the phase induced by the external sources varies slowly in the spatial domain, they can still be propagated to the phase gradient images. However, removal or reduction of such an influence shown in the phase gradient images has not been well studied.

In this work, a novel, phase gradient based method is proposed to quantify the SPIO nanoparticles. In this method, the spherical mean value (SMV) theorem is used to reduce the phase gradients induced by the external sources. By first conducting a phantom study using four different concentrations of aqueous SPIO nanoparticle suspensions, we demonstrated the linear relationship between susceptibility and the concentration of the SPIO nanoparticles, as also reported by early studies (6,7). For an *in vivo* experiment, C6 glioma cells labeled using the SPIO nanoparticles were implanted into the flanks of four mice, which were scanned 1 to 3 days post-injection under a 3 T magnetic field. Assuming the same linearity, the SPIO nanoparticles used to label the C6 glioma cells were quantified using the *in vivo* phase gradient images. Additionally, linear regression analyses were conducted to estimate the consistency of both phantom and *in vivo* results.

4.3 Materials and method

4.3.1 Susceptibility quantification using phase gradients

For typical gradient echo sequences, the incoherently evolved phases (ϕ) is a function of echo time (TE) and magnetic field perturbation (δB), and can be expressed as $\phi(TE) = -\gamma \delta B \cdot TE + \phi_0 \pm 2n\pi$, where γ is the gyromagnetic ratio of the proton, ϕ_0 is the initial phase determined by the MR system, and n is an integer (13). Since the acquired phase can only take values in the principal interval $[-\pi, \pi)$, when it falls outside the principal interval, integer multiples of 2π are added or subtracted to the phase until it falls within the principal interval. This operation causes the phase wrapping (shown as fringes) effect in the raw phase image. Without recovering the unwrapped, continuous phase image, a wrapped phase is seldom utilized for susceptibility quantification. Here, instead of unwrapping the raw phase, we propose a novel method to generate a continuous phase gradient using the following equation:

$$\nabla_x \phi = \cos\phi FT^{-1}[k_x \cdot FT(\sin\phi)] - \sin\phi FT^{-1}[k_x \cdot FT(\cos\phi)] \quad (4.1)$$

In Equation (4.1), FT and FT^{-1} denote the forward and inverse Fourier Transforms. The function k_x is derived according to the gradient of discrete Fourier Transform (see Appendix) and given in Equation (4.2) as:

$$k_x(l) = i\sin(2\pi l / L_x) / \Delta x \quad (4.2)$$

where i is the imaginary unit, L_x is the total number of voxels along the x direction, and Δx is the voxel size along the x direction. It is worthwhile to mention that this method also applies to the y- and z-gradients.

Generally, the phase induced by the external sources is considered to be a harmonic function or harmonic phase, and can be removed or reduced using the SMV theorem from the MR phase image (9,12). As a basic property, the gradients of a harmonic function are still harmonic, so the

harmonic components in the phase gradient images can be removed or reduced using the SMV theorem as well.

According to Maxwell's equations (14), the relation between the phase gradients and the susceptibility of the SPIO nanoparticles (χ) can be expressed using the following equation:

$$\nabla_x \phi(\vec{r}, TE) = -\gamma B_0 TE \nabla_x \int \chi(\vec{r}') \frac{3\cos^2\theta - 1}{4\pi|\vec{r}' - \vec{r}|^3} d^3 r' \tag{4.3}$$

where θ is the angle between $(\vec{r}' - \vec{r})$ and the main magnetic field (B_0). Suppose there exist N regions containing SPIO nanoparticles, and their concentrations are a constant in each individual region, one can convert the convolution shown in Equation (4.3) to a direct multiplication using the Fourier transform:

$$FT(\nabla_x \phi) = -\gamma B_0 TE \sum_{n=1}^{N} \chi_n \cdot FT(V_n) \cdot [k_j \cdot (\frac{1}{3} - \frac{k_3^2}{k^2})] \tag{4.4}$$

where χ_n is the susceptibility of the n^{th} region and V_n represents the binary mask of the n^{th} region. The term $(1/3 - k_3^2/k^2)$ corresponds to the Fourier Transform of the convolution kernel, $(3\cos^2\theta - 1)/(4\pi|\vec{r}|^3)$, shown in Equation (4.3). Therefore, the susceptibilities of the SPIO nanoparticles in different regions can be quantified by solving the inverse problem of Equation (4.4) for χ_n, given that the phase gradients are derived according to Equation (4.1) and the SMV theorem.

4.3.2 Phantom experiment

A phantom experiment was first performed using aqueous suspensions of SPIO nanoparticles (FerroTec, Santa Clara, CA) with different concentrations (50, 75,100 and 125 μg/mL). The suspensions were filled into four plastic vials (0.6 cm in radius), which were then embedded into

a plastic, cylindrical container containing 1% agar gel (6 cm in radius and 20 cm in height). The phantom was imaged using an 8-leg birdcage coil on a 3 T GE Signa HDx clinical whole-body MRI scanner (GE healthcare, Waukesha, WI). The phantom was placed upright at the center of the coil Coronal images were obtained using a 3D gradient echo sequence with a TE of 4.6 ms and a flip angle of 30°. A TR of about 1 s was selected to achieve a complete recovery of the excited spins. The 3D MR images had a field-of-view (FOV) of 14 × 14 × 9 cm^3, and were reconstructed to a size of 128 × 128 × 90.

4.3.3 In vivo mice experiment

About 100 μL phosphate buffered saline (PBS) solution containing approximately 1.1 × 10^6 C6 glioma cells (ATCC, Manassas, VA), among which 1 x 10^5 cells were labeled and 1 x 10^6 were unlabeled, were subcutaneously injected into the flank of a nude mouse. This procedure was repeated for four mice. After 1 to 3 days post-injections, the *in vivo* images were acquired using a 4 cm receive-only RF coil (Phillips Research Europe, Hamburg, Germany) on 3 T whole-body Philips Achieva clinical MR scanner (Phillips Medical Systems, Best, the Netherlands). In order to obtain similar phase images to the phantom study, a 3D gradient echo sequence was applied with a TE of 4.6 ms and a 30° flip angle. The TR was set to 12.6 ms to decrease the scan time of each mouse. The FOV was set to 4 × 4 × 0.9 cm^3, and the axial images were reconstructed to the size of 256 × 256 × 16. This study was performed as part of an approved institutional animal care and use community protocol.

4.3.4 Data processing

All MR images were reconstructed using the fast Fourier transforms of the k-space raw data. The phase gradients were derived based on Equation (4.1), and then filtered using the SMV theorem. The four vials and the injected C6 glioma cells were segmented based on the MR magnitude images, represented as binary masks.

For the phantom study, the susceptibility of each vial was assumed as a constant. Therefore, the susceptibilities of the four vials were quantified by using Equation (4.4) to fit the experimental and theoretical phase gradients near the four vials. The R^2 values were estimated based on the voxels used in the fitting.

For the *in vivo* study, the susceptibilities of the injected C6 glioma cells could not be assumed as a constant. Based on the voxel intensities from low to high, the segmented region of C6 glioma cells were further divided into ten small regions, with each small region having the similar signal intensity. Then, by assuming the susceptibility of each small region was a constant, the susceptibilities of the ten small regions were calculated by fitting the experimental and theoretical phase gradients near the region of the C6 glioma cells. The averaged susceptibility of the C6 glioma cells (χ_{avg}) was derived using the following equation:

$$\chi_{avg} = \sum_{i=1}^{10} n_i \chi_i \Big/ \sum_{i=1}^{10} n_i \tag{4.5}$$

where n_i is the number of voxels in the i^{th} small region, and χ_i is the susceptibility of the i^{th} small region. The R^2 values were estimated based on the voxels used in the fitting.

4.4 Results

4.4.1 Phantom experiment

Figure 4.1 shows the MR magnitude and phase images of the phantom and a preventative mouse. Due to the signal loss caused by the SPIO nanoparticles, the four vials (as labeled in Figure 4.1(a)) and the C6 glioma cells (indicated by the rectangular box in Figure 4.1(c)) appeared darker than the surrounding agar gel and tissues, resulting in a negative image contrast in Figures 4.1(a) and (c). The phase wrapping artifacts are presented as fringes surrounding regions containing SPIO nanoparticles in Figures 4.1(b) and (d), which makes it very hard to directly use the phase images for quantification. The magnetic dipole pattern was also blurred due to the wrapped phase. The x- and y-axes were labeled at the upper-left corner of Figures 4.1(a) and (c).

Figures 4.2(a) and (b) present the experimental x- and y-gradients of the phase image shown in Figure 4.1(b), calculated by using Equation (4.1) and filtered by the SMV theorem. Unlike the wrapped phase, the phase gradients are smooth and continuous. Additionally, it is easy to recognize the blooming pattern of the magnetic dipole, which provides a better contrast enhancement for the SPIO contrast agents, compared to the magnitude and phase images in the Figure 4.1. Figures 4.2(c) and (d) show the theoretically x- and y-gradients, derived by using Equation (4.4) to fit the experiment phase gradients. The estimated susceptibilities of the four vials were listed in Table 1. The blooming patterns surrounding the vials share similarity in Figures 4.2(a) and (b), indicating a good match between the experimental and theoretical results. The regression analyses indicate that the R^2 values are about 0.955 for Figures 4.2(a) and (c), and 0.951 for Figures 4.2(b) and (d).

To further investigate the experimental and theoretical results, we plotted one dimensional (1D) profiles of the phase gradients across the centers of the four vials in Figure 4.3 along the x-

and y-axis, respectively. For example, for the vial 1, Figures 4.3(a) and (e) are the profiles of the x- and y-gradients along the arrows in Figures 4.2(a) and (b). The second to fourth columns correspond to the vials 2 through 4. The solid and dotted lines represent the experimental and theoretical data. As shown, along with increase of the concentration of the SPIO nanoparticles, the peaks become higher, indicating a stronger perturbation to the main magnetic field. One can also observe that the solid and dotted lines match quite well with each other, indicating that the proposed method can result in a relatively accurate quantification of the SPIO nanoparticles for this phantom study. But the solid lines are not as smooth as the dotted lines, possibly due to that Gaussian noise cannot be removed from the experimental data.

Based on the proposed method, the susceptibilities of the four vials were quantified and listed in Table 1. Reference values for 50, 75, 100, and 125 μg/mL SPIO nanoparticles are first provided in the third column of Table 1, which was calculated using previously published results, i.e., 1 μg/mL SPIO nanoparticles generate a susceptibility effect of about 0.0161 ppm at 1.5 T (6). The fourth and fifth columns of Table 1 show the results derived from the x- and y-gradients, which are quite consistent with each other for all the four vials. The averaged susceptibility values are 0.85, 1.46, 1.70, and 2.33 ppm, with respect to the susceptibility of water (0 ppm). Additionally, the concentration of SPIO nanoparticles was linearly fitted to the estimated susceptibility values in Figure 4.4, which shows that the susceptibility increased linearly along with the augment of the concentration. The slopes of the fitted lines (solid) for Figures 4.4(a) and (b) are 0.0188 and 0.0187 ppm·mL/μg under a 3 T magnetic field, respectively.

4.4.2. In vivo mice experiment

Experimental x- and y-gradients of the phase in the Figure 4.1(d) were calculated. The region near the injected C6 glioma cells was zoomed in and presented in Figures 4.5(a) and (b). Blooming pattern of the magnetic dipole caused by the SPIO nanoparticles can be observed surrounding the C6 glioma cells. By only considering the influence of the SPIO nanoparticles, the theoretical x- and y-gradients were calculated and illustrated in Figures 4.5(c) and (d). Since the phase was also perturbed due to the anisotropic susceptibility property of different types of tissues as well as the air-tissue boundary, mismatches between the experimental and theoretical results can be observed in the figures, and the estimated R^2 values are about 0.69 for Figures 4.5(a) and (c), and 0.70 for Figures 4.5(b) and (d). Compared to the R^2 values of the phantom study, they reduce approximately 27% for the *in vivo* result.

In order to further investigate the performance of the proposed method for this *in vivo* application, Figures 4.6(a) and (b) illustrate the 1D profiles of the experimental (solid curves) and theoretical (dotted curves) x- and y-gradients along the two arrows in Figures 4.5(a) and (b). As shown, the dotted curves generally match the solid curves in the most part of the profiles, indicating the performance of the proposed method is fairly acceptable for the *in vivo* application. However, compared with the phantom results in Figure 4.3, the mismatch between the experimental and theoretical data becomes bigger, as evidenced by the R^2 values.

For the four mice, Table 2 enumerates susceptibilities of the SPIO nanoparticles used for cell labeling. According to the phantom study, 1 μg/mL SPIO nanoparticles can induce approximately 0.01875 ppm susceptibility under 3 T magnetic field. Based on this calibration, we were able to estimate the concentrations of the SPIO nanoparticles. Table 2 shows that the quantities of SPIO nanoparticles estimated from the x- and y-gradients are close to each other for

the same mouse, but the averaged concentrations are different for each individual mouse, varying from about 150 μg/mL to 190 μg/mL.

4.5 Discussion

As an important type of contrast agents, SPIO nanoparticles have been utilized in various applications in MRI. In this study, we labeled the C6 glioma cells using the SPIO nanoparticles, and injected them into four nude mice. After 1 to 3 days' growth of the C6 glioma cells, we quantified the concentration of SPIO nanoparticles inside the regions of the C6 glioma cells by using the *in vivo* MR phase gradient images under 3 T magnetic field. For the purpose of accuracy, the *in vivo* quantification was calibrated using a phantom experiment, where data was acquired using the same echo time and magnetic field strength to generate similar phase gradients. Based on our proposed method, the experimental and theoretical results matched well with each other, with $R^2 > 0.95$, for the phantom study. And we found that 1 μg/mL SPIO nanoparticles can induce approximately 0.01875 ppm susceptibility under a 3 T magnetic field. A similar result was reported by de Rochefort et al. that the slope was around 3733 ppm·L/mol, or equivalently 0.0161 ppm·μg/mL, for the SPIO nanoparticles under 1.5 T magnetic field (6). The difference between our reported result and the published result may possibly result from the differences of the magnetic field strength, synthesis approach, and size, etc.

Based on our proposed approach that calculates 3D MR phase gradients by using the fast Fourier transforms, we are able to quantify the SPIO nanoparticles, and thus phase unwrapping, a nontrivial task especially for a three dimensional (3D) dataset, became unnecessary in this study. . Furthermore, since Equation (4.1) utilizes the triangular functions, whose periods are $2n\pi$, the raw phase can be directly implemented for calculation. Additionally, the SMV theorem was

suggested in this work to process the phase gradient images, so that influences of the external sources, as mentioned in the introduction, could be minimized, resulting in more accurate quantification of the SPIO nanoparticles. However, there are still some issues for the application of the SMV theorem. For example, the injected C6 glioma cells were very close to the air-tissue boundary for all of the four mice. According to Li et al, the SMV theorem is not able to completely eliminate the induced harmonic terms at the air-tissue boundary (8). Strong phase gradients were observed at the air-tissue boundary of the mouse body in Figures 4.5(a) and (b), and data points in these regions should not be involved. However, this issue can be ignored naturally, when the region of interest is not close to the boundary.

Based on the linear relationship between the susceptibility and the concentration, the SPIO nanoparticles used for C6 glioma cell labeling were indirectly quantified by implementing Equation (4.4) to calculate the susceptibility of the SPIO nanoparticles. By taking advantage of the negative contrast resulted from the SPIO nanoparticles, the regions, where the SPIO nanoparticles deposited, was segmented from the surrounding regions, such as agar gel and tissues in this work. Because the binary masks of the vials in the phantom experiment and the C6 glioma cells in the *in vivo* experiment behaved as a strong constraint for the inverse problem of Equation (4.4), no optimization algorithm, such as the Bayesian regularization, was involved in the proposed quantification method. One potential disadvantage of this approach is that, without considering susceptibility sources other than the SPIO nanoparticles, issues may arise when there are sources with large susceptibility near the SPIO nanoparticles. However, this problem is rare in most of cases, as the SPIO nanoparticles are usually of higher susceptibility than any normal tissues, such as muscles, bones, fat, organs, and etc. It is worth to mention that the air-boundary

issue, caused by the imperfect performance of the SMV theorem, applies to the proposed method as well as other QSM methods.

In this work, the fitting between the experimental and theoretical data was performed only using voxels closed to the SPIO nanoparticle accumulated regions, which is faster and more accurate than using all the voxels of the image. With consideration of a non-uniform distribution of the SPIO nanoparticles, we further divided the segmented region of the C6 glioma cells into ten small sub-regions based on the signal intensity, which resulted in a fairly good match between the experimental and theoretical data, as illustrated in Figures 4.5 and 4.6. However, there are limitations. When the concentration of the SPIO nanoparticles rises to a very high value, as a negative contrast agent, SPIO induced signal loss becomes so severe that the division cannot reflect the real distribution of the SPIO nanoparticles in the injected region. Fortunately, pulse sequences, like the UTE sequence and the SWIFT sequence, have been developed to image short T_2 materials (15-17). With the help of these pulse sequences, such an issue can be resolved. Additionally, if a small sub-region only consists of few voxels, according to Cheng et al, the calculated phase and phase gradients for that sub-region will become inaccurate when using the fast Fourier transforms (18). Therefore, sub-regions that are too small should be combined to increase the number of voxels in a single sub-region.

Based on the quantification results for the *in vivo* study, the SPIO nanoparticles still existed with a detectable amount in the flanks of the four mice, after 1 to 3 days of the injections. Such a fact potentially allows a longitudinal monitoring (more than 3 days) of different types of cells that are labeled by SPIO nanoparticles. However, the fluctuation of the amount of SPIO nanoparticles among different mice indicates that many biological effects, such as migration and death of labeled cells, blood diffusions, aggregation of the labeling nanoparticles, may probably

contribute to the dynamic change of the concentrations of both the injected cells and the SPIO nanoparticles (19). Although this work reasonably quantified the residual SPIO nanoparticles in the mouse bodies, more details of the above-mentioned dynamic changes and the corresponding explanations need to be studied in future work.

It is worthwhile to mention that in this work, motions of the animals were not considered, as the mice were under anesthesia and the scanned regions of the mouse were not close to the chest area, where respiratory or cardiac motion was prominent. For applications when there exists motions that prevent one to derive an accurate quantification, motion corrections of the MR images should be performed.

4.6 Conclusions

In summary, a quantification method for SPIO nanoparticles was developed by using the MR phase gradients. A phantom study with four different concentrations of SPIO nanoparticles was conducted to calibrate a linear relationship between susceptibility and concentration of SPIO nanoparticles under a 3 T magnetic field. By assuming the same linearity of SPIO susceptibility versus concentration under the same magnetic field, *in vivo* quantification of SPIO nanoparticles used for labeling C6 glioma cells was investigated by using MR phase images acquired from four mice at 1 to 3 days post-injections. Results of both experiments showed that the concentration of SPIO nanoparticles can be determined in fair consistency using the developed MR phase gradient approach.

4.7 Appendix

Assuming *g* and *G* are a discrete Fourier pair with a length scale *L*, we define the discrete Fourier Transforms as

$$G(n\Delta k) = \sum_{m=-N/2}^{N/2-1} g(m\Delta x) e^{-i2\pi mn/N} \qquad n \in [-N/2, N/2-1]$$

$$g(m\Delta x) = \frac{1}{N} \sum_{n=-N/2}^{N/2-1} G(n\Delta k) e^{i2\pi mn/N} \qquad m \in [-N/2, N/2-1]$$

where N is an even number, and the step size of the x-space and k-space are given by $\Delta x = L/N$ and $\Delta k = 1/L$, respectively. Thus, the gradient of *g(x)* in terms of discrete Fourier Transform is given by:

$$\begin{aligned}
\frac{\partial}{\partial x} g(x) &= \frac{g[(m+1)\Delta x] - g[(m-1)\Delta x]}{2\Delta x} \\
&= \frac{1}{2\Delta x}\left[\frac{1}{N} \sum_{n=-N/2}^{N/2-1} G(n\Delta k) e^{i2\pi(m+1)n/N} - \frac{1}{N} \sum_{n=-N/2}^{N/2-1} G(n\Delta k) e^{i2\pi(m-1)n/N}\right] \\
&= \frac{1}{2\Delta x N} \sum_{n=-N/2}^{N/2-1} G(n\Delta k) e^{i2\pi mn/N} (e^{i2\pi n/N} - e^{-i2\pi n/N}) \\
&= \frac{1}{N} \sum_{n=-N/2}^{N/2-1} i \frac{\sin(2\pi n/N)}{\Delta x} G(n\Delta k) e^{i2\pi mn/N} \\
&= FT^{-1}\left[i \frac{\sin(2\pi n/N)}{\Delta x} G(n\Delta k)\right]
\end{aligned}$$

Therefore, the gradient of *g(x)* can be calculated by a multiplication of $i\sin(2\pi n/N)/\Delta x$ and *G(k)* for the discrete Fourier transform.

4.8 References

1. van Tiel ST, Wielopolski PA, Houston GC, Krestin GP, Bernsen MR. Variations in labeling protocol influence incorporation, distribution and retention of iron oxide nanoparticles into human umbilical vein endothelial cells. Contrast media & molecular imaging 2010;5(5):247-257.
2. Smirnov P, Gazeau F, Beloeil JC, Doan BT, Wilhelm C, Gillet B. Single-cell detection by gradient echo 9.4 T MRI: a parametric study. Contrast media & molecular imaging 2006;1(4):165-174.
3. Kustermann E, Himmelreich U, Kandal K, Geelen T, Ketkar A, Wiedermann D, Strecker C, Esser J, Arnhold S, Hoehn M. Efficient stem cell labeling for MRI studies. Contrast media & molecular imaging 2008;3(1):27-37.
4. McFadden C, Mallett CL, Foster PJ. Labeling of multiple cell lines using a new iron oxide agent for cell tracking by MRI. Contrast media & molecular imaging 2011;6(6):514-522.
5. Wang L, Corum CA, Idiyatullin D, Garwood M, Zhao Q. T(1) estimation for aqueous iron oxide nanoparticle suspensions using a variable flip angle SWIFT sequence. Magnetic resonance in medicine 2013;70(2):341-347.
6. de Rochefort L, Brown R, Prince MR, Wang Y. Quantitative MR susceptibility mapping using piece-wise constant regularized inversion of the magnetic field. Magnetic resonance in medicine 2008;60(4):1003-1009.
7. de Rochefort L, Liu T, Kressler B, Liu J, Spincemaille P, Lebon V, Wu J, Wang Y. Quantitative susceptibility map reconstruction from MR phase data using bayesian

regularization: validation and application to brain imaging. Magnetic resonance in medicine 2010;63(1):194-206.

8. Li W, Wu B, Liu C. Quantitative susceptibility mapping of human brain reflects spatial variation in tissue composition. NeuroImage 2011;55(4):1645-1656.

9. Schweser F, Deistung A, Lehr BW, Reichenbach JR. Quantitative imaging of intrinsic magnetic tissue properties using MRI signal phase: an approach to in vivo brain iron metabolism? NeuroImage 2011;54(4):2789-2807.

10. Zhao Q, Langley J, Lee S, Liu W. Positive contrast technique for the detection and quantification of superparamagnetic iron oxide nanoparticles in MRI. NMR in biomedicine 2011;24(5):464-472.

11. Bakker CJ, de Leeuw H, Vincken KL, Vonken EJ, Hendrikse J. Phase gradient mapping as an aid in the analysis of object-induced and system-related phase perturbations in MRI. Physics in medicine and biology 2008;53(18):N349-358.

12. Li L. Magnetic susceptibility quantification for arbitrarily shaped objects in inhomogeneous fields. Magnetic resonance in medicine 2001;46(5):907-916.

13. Haacke EM. Magnetic resonance imaging : physical principles and sequence design. New York: Wiley; 1999. xxvii, 914 p. p.

14. Jackson JD. Classical electrodynamics. New York: Wiley; 1999. xxi, 808 p. p.

15. Robson MD, Gatehouse PD, Bydder M, Bydder GM. Magnetic resonance: an introduction to ultrashort TE (UTE) imaging. Journal of computer assisted tomography 2003;27(6):825-846.

16. Idiyatullin D, Corum C, Park JY, Garwood M. Fast and quiet MRI using a swept radiofrequency. Journal of magnetic resonance 2006;181(2):342-349.

17. Idiyatullin D, Corum C, Moeller S, Garwood M. Gapped pulses for frequency-swept MRI. Journal of magnetic resonance 2008;193(2):267-273.

18. Cheng YC, Neelavalli J, Haacke EM. Limitations of calculating field distributions and magnetic susceptibilities in MRI using a Fourier based method. Physics in medicine and biology 2009;54(5):1169-1189.

19. Kotek G, van Tiel ST, Wielopolski PA, Houston GC, Krestin GP, Bernsen MR. Cell quantification: evolution of compartmentalization and distribution of iron-oxide particles and labeled cells. Contrast media & molecular imaging 2012;7(2):195-203.

Tables

Table 4.1: Estimated susceptibilities for the phantom

Vial Number	Concentration [µg/mL]	Susceptibility [ppm]			
		Reference	x-gradient	y-gradient	Average
1	50	0.81	0.85	0.85	0.850
2	75	1.21	1.45	1.46	1.455
3	100	1.61	1.71	1.69	1.700
4	125	2.01	2.32	2.33	2.325

Table 4.1 lists the concentrations and the estimated susceptibilities of the SPIO nanoparticles.

Table 4.2: Estimated susceptibilities and concentrations for the *in vivo* mice

Subject number	From x-gradient		From y-gradient		Average
	Susceptibility [ppm]	Concentration [μg/mL]	Susceptibility [ppm]	Concentration [μg/mL]	Concentration [μg/mL]
Mouse #1	3.12	167	3.18	170	168.5
Mouse #2	3.60	192	3.51	188	190.0
Mouse #3	2.73	146	2.97	159	152.5
Mouse #4	3.51	188	3.46	185	186.5

Table 4.2 lists the *in vivo* estimated susceptibilities and concentrations of the SPIO nanoparticles used for labeling the C6 glioma cells. The concentrations were derived based on the phantom result that the susceptibility of 1 μg/mL SPIO nanoparticles is about 0.0188 ppm at 3 T.

Figures

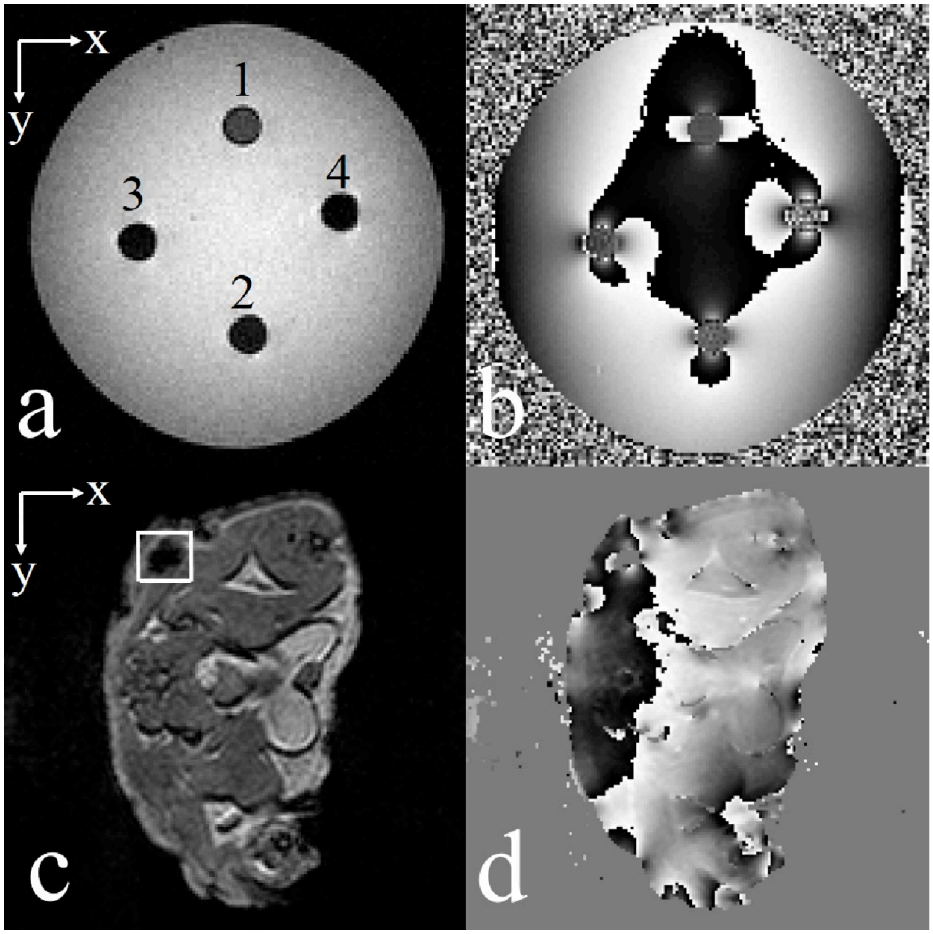

Figure 4.1. The magnitude and phase images of the phantom are shown in (a) and (b). The vials containing SPIO nanoparticles are labeled as vials 1 to 4 in (a), corresponding to the concentrations of 50, 75,100 and 125 μg/mL, respectively. The magnitude and phase images of a representative mouse are shown in (c) and (d). The region containing C6 glioma cells labeled with SPIO nanoparticles is indicated by the rectangular box in (c). Phase fringes can be observed in both (b) and (d) for the phantom and *in vivo* datasets. The coordinates of the figures are labeled at the upper-left corners of (a) and (c).

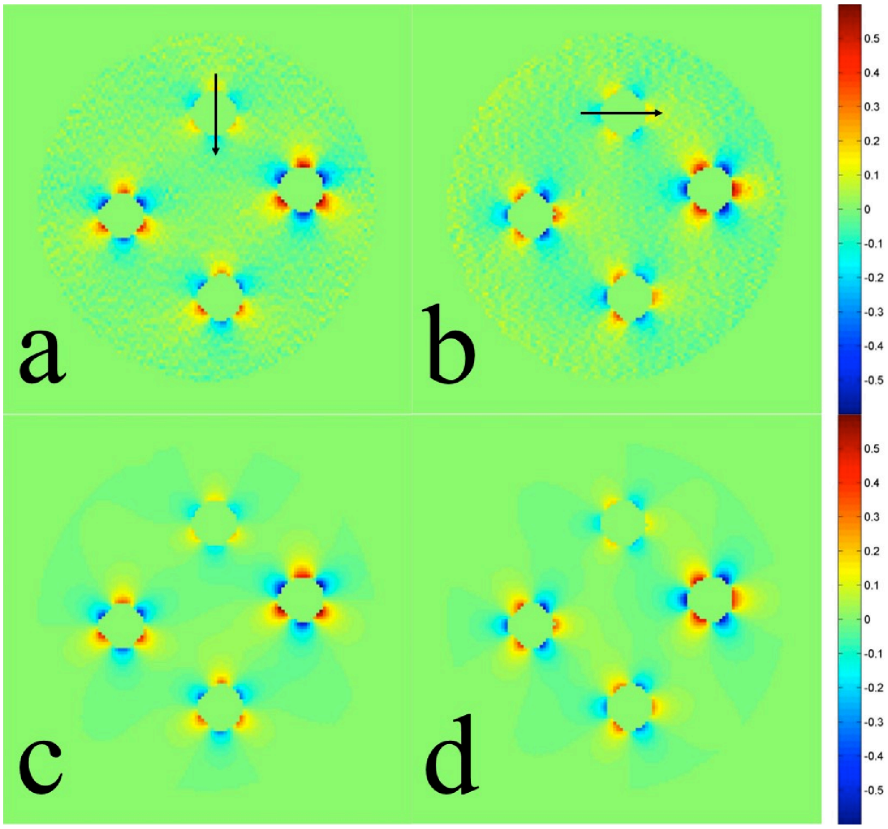

Figure 4.2. The experimental x- and y-gradients of the phase in Figure 1(b) were calculated using the proposed method, and are illustrated in (a) and (b), respectively. The theoretical x- and y-gradients were derived from the estimated susceptibilities of the four vials, and are shown in (c) and (d). By comparing the experimental and theoretical results, the R^2 values are about 0.955 for (a) and (c), and 0.951 for (b) and (d). The unit of the scale bars is in [rad/mm].

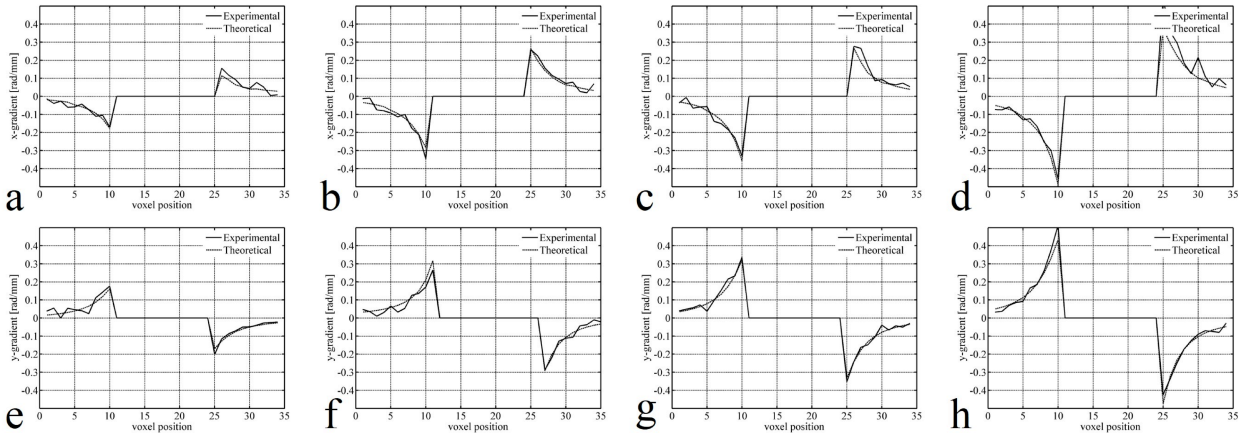

Figure 4.3. For vial 1, the profiles of the x- and y-gradients along the arrows in Figures 2(a) and (b) were plotted in (a) and (e), respectively. The solid and dotted lines correspond to the experimental and theoretical results, and the unit of the phase gradients is in [rad/mm]. Similar profiles of the x- and y-gradients across the centers of vials 2, 3 and 4 are illustrated in the second, third and fourth columns of this figure.

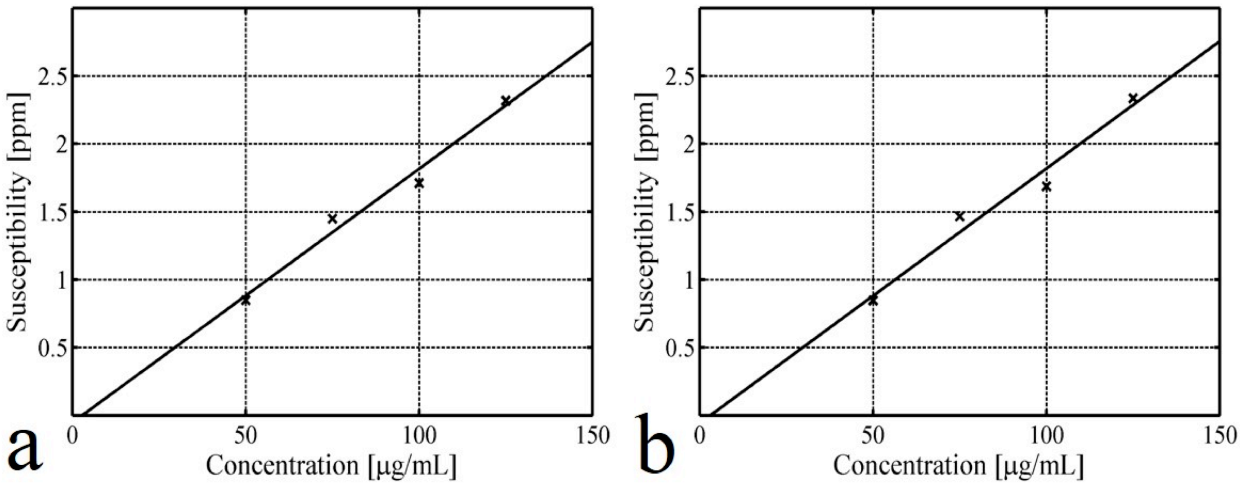

Figure 4.4. For the SPIO nanoparticles in the vials 1 to 4, the corresponding concentrations (x axis) are plotted versus the susceptibilities (y axis) derived from the (a) x- and (b) y-gradients of the phase. A linear fitting was performed and indicates that the slopes are 0.0188 and 0.0187 ppm·mL/μg for (a) and (b).

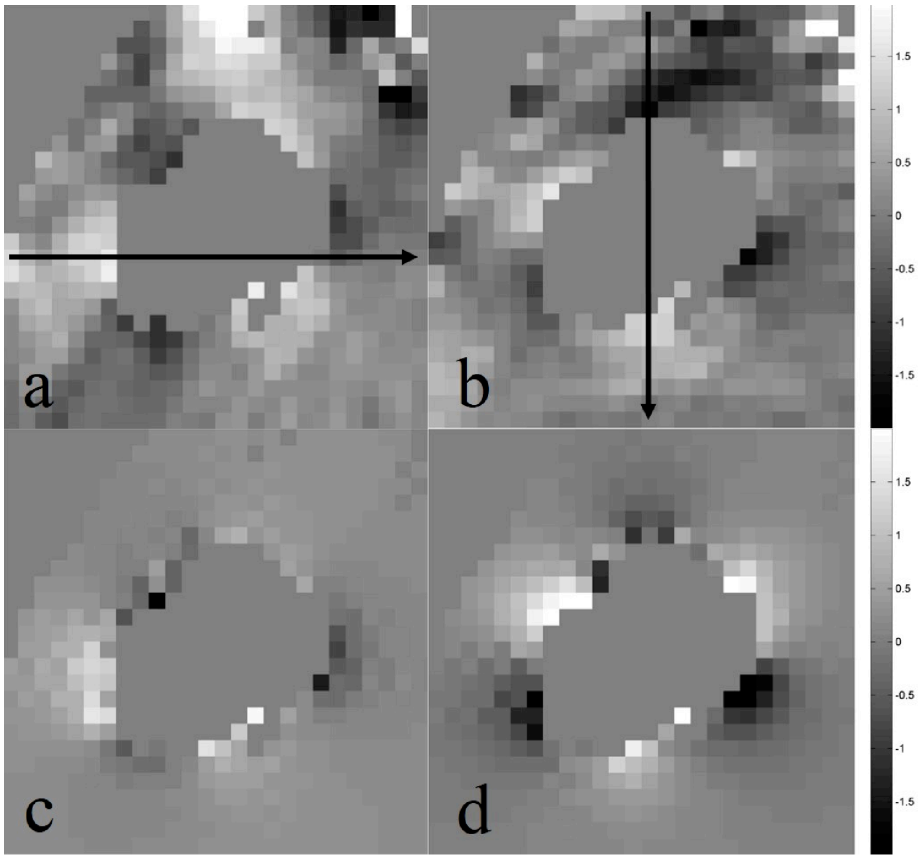

Figure 4.5. Experimental x- and y-gradients of the phase of the mouse shown in Figure 1(d) were calculated using the proposed method, and the results near the injected C6 glioma cells were zoomed in and are illustrated in (a) and (b), respectively. By fitting to the voxels close to the regions of the injected C6 glioma cells, the theoretical x- and y-gradients were derived and are shown in (c) and (d). The R^2 values of the fitting are 0.69 for (a) and (c), and 0.70 for (b) and (d). The unit of the scale bars is in [rad/mm].

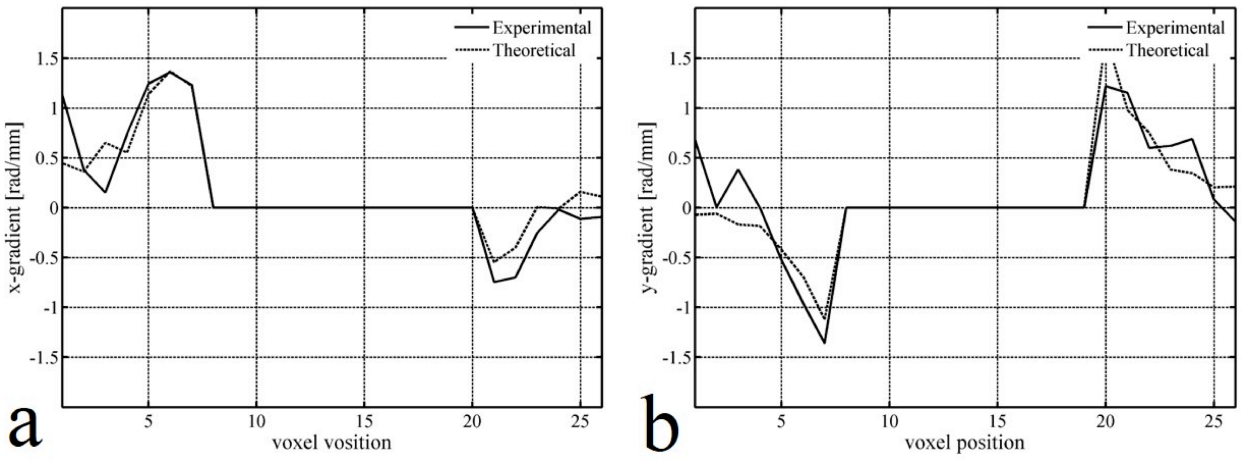

Figure 4.6. The profiles of the x- and y-gradients along the arrows in Figures 5(a) and (b) were plotted in (a) and (b), respectively. The solid and dotted lines correspond to the experimental and theoretical results, and the unit of the phase gradients is in [rad/mm].

CHAPTER 5

T_1 ESTIMATION FOR AQUEOUS IRON OXIDE NANOPARTICLE SUSPENSIONS USING A VARIABLE FLIP ANGLE SWIFT SEQUENCE[4]

[4] Wang, L., Corum, C., Idiyatullin, D., Garwood, M., and Zhao, Q. Magnetic Resonance in Medicine 70:341–347 (2013)
Reprinted here with permission of the publisher

5.1 Abstract

Purpose:

T_1 quantification of contrast agents, such as superparamagnetic iron oxide nanoparticles, is a challenging but important task inherent to many in vivo applications in magnetic resonance imaging. In this work, a sweep imaging with Fourier transformation using variable flip angles (VFAs-SWIFT) method was proposed to measure T_1 of aqueous superparamagnetic iron oxide nanoparticle suspensions.

Methods:

T_1 values of various iron concentrations (from 1 to 7 mM) were measured using VFA-SWIFT and three-dimensional spoiled gradient-recalled echo with VFAs (VFA-SPGR) sequences on a 7 T MR scanner. For validation, T_1 values were also measured using a spectroscopic inversion-recovery sequence on a 7 T spectrometer.

Results:

VFA-SWIFT demonstrated its advantage for quantifying T_1 of highly concentrated aqueous super-paramagnetic iron oxide nanoparticle suspensions, but VFA-SPGR failed at the higher end of iron concentrations. Both VFA-SWIFT and VFA-SPGR yielded linear relationships between the relaxation rate and iron concentrations, with relaxivities of 1.006 and 1.051 s^{-1} mM^{-1} at 7 T, respectively, in excellent agreement with the spectroscopic measurement of 1.019 s^{-1} mM^{-1}.

Conclusion:

VFA-SWIFT is able to achieve accurate T_1 quantification of aqueous super-paramagnetic iron oxide nanoparticle suspensions up to 7 mM.

5.2 Introduction

Super-paramagnetic iron oxide (SPIO) nanoparticles have been widely used as T2 or T_2* contrast agents in magnetic resonance imaging. Various applications including visualization of vasculature, macrophage uptake, and cell labeling have been demonstrated (1–3). Recently studies demonstrated that SPIO nanoparticles could be applied to hyperthermia treatment of cancer (4,5). However, as the SPIO concentration increases, MR signal loss and image distortions become more prominent in the regions near the SPIO nanoparticles.

In recent years, ultrashort echo time (UTE) (6,7) and sweep imaging with Fourier transformation (SWIFT) (8,9) sequences have been designed to shorten the time interval between signal excitation and acquisition, down to several microseconds. Therefore, short T_2* signal loss can be minimized. For example, the UTE sequence was applied to visualize short T_2* materials (10). The T_1 estimation of low concentrations (up to 1.2 mM) of SPIO nanoparticles was conducted by using the UTE sequence (11). Springer et al. assessed T1 values in materials and tissues (e.g., cortical bones) with extremely fast signal decay using the UTE sequence combined with a variable flip angle (VFA) method (12).

Similarly, the SWIFT sequence was implemented for detection of calcifications in rat brain and SPIO-labeled stem cells grafted in the myocardium (13,14). Recently, Chamberlain et al. (15) proposed a Look-Locker saturation recovery method integrated with SWIFT to measure T_1 with an adiabatic half passage followed by a spoiler gradient to achieve saturation. Despite the breakdown of the linear relationship at ultrahigh concentrations (above 1 mg Fe/mL), they demonstrated that SWIFT could be used to measure T_1 at iron concentrations (0.3 to 1.5mg Fe/mL) previously almost impossible by magnetic resonance imaging.

With SWIFT, the signal is measured in the steady state; thus, image contrast can be optimized by properly adjusting the flip angle close to the Ernst angle, the ideal condition at which the signal intensity reaches its peak for a given T_1 (8,16). The spoiled steady state nature of the SWIFT technique provides an opportunity to derive a T_1 map through measurements conducted with VFAs.

In many in vivo applications of SPIO nanoparticles, such as cell tracking and therapeutic response evaluation, the iron concentration is at low or medium levels. In this work we hypothesize that the VFA-SWIFT sequence is able to measure T_1 of ferrofluids, consisting of SPIO nanoparticle solutions with higher range of iron concentrations than usually encountered (from 1 to 7 mM).

When attempting to measure T_1 using VFA methods, an ambiguous solution for T_1 can sometimes result when using an inhomogeneous radiofrequency field B_1 for excitation. To overcome this difficulty, we utilize a birdcage coil that provides a better B_1 field homogeneity (i.e., more uniform spin excitation and reception) compared to a surface coil. In addition, we use a scheme of small step-size, multiple flip angles for accuracy of estimation. For the purpose of comparison, T_1 values were also quantified using the three-dimensional (3D) spoiled gradient-recalled echo at VFAs (VFA-SPGR) sequence. In order to verify the obtained results, relaxation data were also acquired with a spectroscopic inversion recovery (IR) sequence and resulting T_1 values are compared with those measured by VFA-SWIFT and VFA-SPGR.

5.3 Theory

For a general steady state MR scan, the signal intensity is theoretically given by (16):

$$s(\theta) = M_0 \sin\theta \frac{1 - E_1}{1 - E_1 \cos\theta} e^{-TE/T_2^*} \quad [5.1]$$

where $E_1 = e^{-TR/T_1}$, and M_0 and θ represent proton density and flip angle, respectively. With fixed echo time (TE) and repetition time (TR), T_1 can be measured through scans at multiple flip angles (16,17):

$$\frac{s(\theta)}{\sin\theta} = E_1 \frac{s(\theta)}{\tan\theta} + M_0(1 - E_1)e^{-TE/T_2^*} \quad [5.2]$$

The terms E_1 and $M_0(1 - E_1)e^{-TE/T_2^*}$ can be numerically solved as the slope and coordinate intercept of Eq. [5.2] through a linear least-squares fit, and T_1 can then be estimated from the natural logarithm of E_1. However, for materials with short T_2* values, the signal intensity, s(θ), given by Eq. [5.1] will decay exponentially and result in a poor signal-to-noise ratio (SNR) when TE is close to or longer than T_2*, which could dramatically influence the accuracy of the derived T_1 using Eq. [5.2].

For the SWIFT sequence, the magnetic field variation resulting from the applied gradient field is generally large compared to other potential perturbations, such as magnetic field inhomogeneity and magnetic susceptibility differences, and these effects are minimal in acquired images (8) due to the simultaneous high bandwidth excitation and acquisition. Additionally, SWIFT images are minimally influenced by transverse relaxation, since the dead time between signal excitation and acquisition is usually much shorter than T_2* values (8). Under these circumstances, a region-of-interest in a SWIFT image is immune to signal loss due to T_2* values of the scanned subject if signal pileup artifacts are included in the region-of-interest (14). This leads to T_2* independent signal intensity for the region-of-interest in the following form (8):

$$s(\theta) = M_0 \sin\theta \frac{1 - E_1}{1 - E_1 \cos\theta} \quad [5.3]$$

Therefore, VFA-SWIFT provides a method for T_1 estimation that can ignore the influence of signal loss caused by the fast T_2* decay and allow for quantification of ferrofluid with high iron concentrations.

5.4 Methods

Data acquisition

Commercially available ferrofuild (EMG 509, FerroTec, Santa Clara, CA) was diluted into seven different iron concentrations: 1, 2, 3, 4, 5, 6, and 7 mM Fe, where 1mM Fe is about 0.056 mg Fe/mL. The diluted ferrofluid was then filled into plastic vials (0.3 mL in volume). All vials together with a vial of purified water (labeled as 0) were then embedded into a rectangular container, which was filled with 1 % agar gel. The MR experiment was performed on a 7 T Varian Magnex small animal scanner (Agilent Technologies, Santa Clara, CA) that provides a maximum gradient strength of 440 mT/m. The phantom was vertically placed in the center of a transmit/receive birdcage coil with a diameter of 7.2 cm.

First, 3D radial SWIFT images were obtained using a hyperbolic secant pulse with the dimensionless shape factor n = 1 and truncation factor β = 7.6, respectively (8,9). The pulse had a spectral width of 62.5 kHz and included 256 gaps. The length of the pulse elements and gaps were 4 and 12 ms, respectively. The dead time between the end of each pulse element and the beginning of signal acquisition was set to 3.9 ms, referred to as the effective TE. Complex data in the radial k-space consisted of 64,000 spokes, which covered a spherical field-of-view of 80^3 mm^3. The TR was equal to 6 ms, including a 1.9 ms interval between two sequential hyperbolic secant pulses. Before actual data acquisition, 512 dummy scans were implemented to generate a

steady state. Multiple flip angles, from 4° to 36° with a step size of 2°, were applied for T_1 estimation.

Next, for comparison purposes, a general steady state scan of the phantom was performed using a 3D SPGR sequence. To minimize signal loss caused by the T_2* decay, the shortest TE achievable for the 7 T scanner was selected. The scan parameters were: TE/TR = 2.95/6 ms, spectral width = 62.5 kHz, field-of-view = 80^3 mm^3, matrix size = 256^3, and 512 dummy scans were performed to reach a steady state. Both RF and gradient spoils were implemented to enhance the T_1 weighted contrast and eliminate any residual signal. As in the SWIFT scan, the flip angles were varied from 4° to 36° with a step size of 2°.

To verify the estimated T_1 values derived by the magnetic resonance imaging-based approaches, spectroscopic data were acquired using a vertical 7 T Varian NMR spectrometer (Agilent Technologies, Santa Clara, CA). An IR pulse sequence was implemented, and the IR delays (TI) were varied from 10 to 690 ms with an increment of 20 ms for vials 1 to 7. Between two IR scans, a 3 s time interval was inserted after the data acquisition to allow a full recovery of the magnetization.

Furthermore, in order to estimate how T2 influences the flip angles of SWIFT, T2 of the highest iron concentration solution (vial 7) was measured using a Carr-Purcell Meiboom-Gill sequence on the 7 T spectrometer, with 40 different TE values varied uniformly from 0.1 to 4 ms, and with TR ≈ 1 s.

Data processing

The k-space data of the SWIFT sequence were processed using signal processing and gridding code written in LabVIEW (National Instruments, Austin, TX) and interpolated with a Kaiser-

Bessel function onto a Cartesian grid (18) utilizing compiled Matlab mex code (MathWorks, Natick, MA). Complex images were then obtained by using the Fourier transforms of the 3D k-space data in a Cartesian coordinate frame.

Least-square fits were implemented based on Eqs. [5.2] and [5.3] for every voxel of the VFA-SWIFT images to derive the T_1 map of different concentrations of aqueous SPIO nanoparticle suspensions. As a comparison, the T_1 map was also calculated using the 3D SPGR images at different flip angles. For the spectroscopic IR data, T_1 values of the vials 1 to 7 were obtained by fitting Eq. [5.4]:

$$s(TI) = A(1 - 2e^{-TI/T_1}) \qquad [5.4]$$

where A is a scaling factor. To minimize errors, the largest measurable T_1 for the various concentrations of ferrofluid was cut off at 2.5 s in this work. T_1 mapping and data fitting codes were implemented in Matlab (MathWorks, Natick, MA).

T_2 of the vial 7 was obtained using the spectroscopic Carr-Purcell Meiboom-Gill data by fitting Eq. [5.5]:

$$s(TE) = Ae^{-TE/T_2} \qquad [5.5]$$

For SWIFT and SPGR, the average SNR of vial 7 was derived experimentally by dividing the mean signal intensity inside the vial by the noise standard deviation.

5.5 Results

Figure 5.1 displays the magnitude images acquired with SWIFT (first row) and SPGR (second row) sequences at flip angles of 10° (first column), 20° (second column), and 30° (third column). Vials with different iron concentrations were labeled in Figure 5.1a, where vial 0 only contained purified water and vials 1 through 7 corresponded to iron concentrations ranging from 1 to 7 mM

(see Table 5.1 for details). As shown for the SWIFT images, signal intensity of the water and agar gel decayed as the flip angle increased. The vials with higher concentrations of SPIO nanoparticles appeared brighter than those with lower concentrations. As can be seen in Figure 5.1a, line-broadening and off-resonance artifacts become more apparent as the concentration increases beyond 5 mM (vials 5 through 7). In the SPGR images, signal from background agar gel was also decreased at larger flip angles, similar to that seen in the SWIFT images. However, for vials containing more than 3 mM iron (vial 3 through 7), T_2* decay becomes strong and dominant with SPGR, resulting in significant signal loss, image distortions, and negative contrast. Conversely, the SWIFT sequence provided positive contrast for the SPIO nanoparticle solutions.

Further analyses of these imaging data are shown in Figure 5.2. The plots show the normalized (with respect to its maximum value) and averaged signal intensity of vials 1, 4, and 7 (representing a low, medium, and high concentration) as a function of flip angles for the VFA-SWIFT (first row) and VFA-SPGR (second row), and as a function of TI for the spectroscopic measurement (third row). A linear least-squares fitting was done first using Eq. [5.2] to estimate the slope and coordinate intercept, and then the two quantities were plugged back into Eq. [5.1] for SPGR and Eq. [5.3] for SWIFT to re-plot the signal intensity (shown as the solid line) as a function of flip angles. Along with the increment in iron concentration, the standard deviation (shown as error bars) increased accordingly. The Ernst angle for vials 1, 4, and 7 were at approximately 7°, 13°, and 17°; thus, the corresponding signal peak at the Ernst angle could be observed in Figures 5.2a-e. However, the iron concentration in vial 7 was so high that the signal was degraded significantly because of the fast T_2* decay for the SPGR images, resulting a flatter plot than that of vials 1 and 4 and large error bars. Thus, Figure 5.2f failed to match the fitting

curve because the signal at different flip angles was contaminated by noise. As shown in Figures 5.2g-i, the spectroscopic IR data were well fitted to Eq. [5.4]. The signal null points, which were decreased as the iron concentrations increased, were noticed at TI of 500, 170, and 90 ms for vials 1, 4, and 7, respectively.

Figure 5.3 shows the estimated T_1 maps resulting from the (a) VFA-SWIFT and (b) VFA-SPGR acquisitions. According to the figure, both sequences resulted in a good T_1 estimation when concentrations were lower than 5 mM (vial 0 through 5). T_1 of ferrofluid in vials 6 and 7 could only be obtained from Figure 5.3a, but not from Figure 5.3b. This indicates that the SWIFT sequence is more suitable for measuring T_1 of ferrofluid at high concentrations, compared to the 3D SPGR sequence. As seen from the two T_1 maps, T_1 was decreased and the line-broadening and off-resonance artifacts become significant along with the increase of concentrations. Furthermore, two shaded regions can be observed at both the left and right sides of Figure 5.3b, indicating the estimated T_1 of agar gels at these regions was influenced by the magnetic field inhomogeneity.

Figures 5.4a-c presents the linear fitting of the relaxation rate R_1 to the various iron concentrations for the VFA-SWIFT, VFA-SPGR, and spectroscopic based methods. Figure 5.4a shows that a linear relationship between R1 and the iron concentration is valid for all concentrations up to 7 mM. According to the fit, the specific relaxivity (r_1) of the ferrofluid was 1.006 s^{-1} mM^{-1} under a 7 T magnetic field. Figure 5.4b presents a similar fit as that of Figure 5.4a, but without considering the last two data points (not shown) due to the significant signal loss caused by the T_2* effect. By using the first five data points, the resulting relaxivity was equal to 1.051 s^{-1} mM^{-1}. In Figure 5.4c, a nearly perfect linear fitting is shown and the relaxivity derived by the spectroscopic IR approach was equal to 1.019 s^{-1} mM^{-1}. The corresponding R^2

values were 0.996, 0.989, and 0.997 for Figures 5.4a-c, respectively. However, for the VFA-SPGR result in the Figure 5.4b, standard deviations of the estimated R_1 increased significantly at 5 mM compared to that at low concentrations and the corresponding SWIFT result.

Table 5.1 summarizes the quantitative T_1 estimates for the various iron concentrations using the VFA-SWIFT, VFA-SPGR, and spectroscopic methods. The first two columns list the vial numbers and their iron concentrations, while the estimated T_1 are given in the last three columns. Note that the VFA-SPGR method was unable to estimate T_1 for high iron concentrations. Additionally, standard deviations of the T_1 values measured by VFA-SWIFT are slightly smaller than that measured by VFA-SPGR, especially at higher concentrations. The highest concentration at which the VFA-SPGR method can reliably measure T_1 is about 5 mM. By comparing with the spectroscopic measurements, it can be seen that both VFA-SWIFT and VFA-SPGR provide accurate estimates of T_1 when the iron concentration is in the low to medium range, but only VFA-SWIFT reliably measures T_1 at high iron concentrations.

Based on Eq. [5.5], the estimated T_2 of the vial 7 is about 1.04 ms by fitting data acquired at all the TEs in the Carr-Purcell Meiboom-Gill measurement. For the vial 7, the averaged experimental SNR of the SWIFT images is about three to five times bigger than that of the SPGR images.

5.6 Discussion

In the past, T_1 estimation of highly concentrated ferrofluid has usually suffered from signal loss caused by the rapid T_2* decay. This study presents the VFA-SWIFT method to map T_1 of aqueous suspensions containing SPIO contrast agents, along with comparisons with two other common approaches: VFA-SPGR and spectroscopic IR. Here, the SWIFT sequence was applied

to scan the SPIO sample vials using multiple flip angles. As the dead time between the signal excitation and acquisition is shortened to 3.9 ms, signal loss caused by T_2* decay is minimized. Consequently, the signal intensity is dependent on proton density, flip angle, T_1, and TR values. Furthermore, the vials filled with ferrofluid displayed T_1-weighted positive contrast, where the SNR of these vials was higher than that of the agar gel alone in the SWIFT images (Figure 5.1). As T_2* decay has minimal influence on the SWIFT images, the theoretical model (Eq. [3]) for T_1 measurement and the experimental data agreed reasonably well (as seen in Figures 5.2a-c). As a result, relatively small error bars were obtained for the estimated R_1 values of ferrofluid even at high concentrations (as shown in Figure 5.4a).

Measurements obtained with VFA-SPGR and spectroscopic IR methods were compared with those measured by VFA-SWIFT. In the SPGR sequence, a minimally allowed TE of 2.95 ms was utilized, aiming to minimize T_2* signal loss caused by high iron concentration. By using this short TE, MR signals resulting from SPIO concentrations up to 4 mM (vial 4) were still comparable to the background signal of agar gel (as shown in the second row of Figure 5.1). Based on the SPGR images, we were able to measure the T_1 of the first five vials (with concentrations up to 5 mM), although the standard deviations increased with concentration (as shown in the Figure 5.4b). However, compared to the VFA-SWIFT, this method was more susceptible to T_2* signal loss. The spectroscopic IR measurement was used as a reference in this work, and it demonstrated that VFA-SWIFT and VFA-SPGR allowed accurate estimations of T_1 for ferrofluid at iron concentrations up to 7 and 5 mM, respectively.

SWIFT has demonstrated advantages over SPGR in detecting materials with short T_2* values. However, with the modest acquisition bandwidth (62.5 kHz) used in the present SWIFT experiments, it was not possible to entirely eliminate influences from the strong magnetic field

inhomogeneity caused by SPIO nanoparticles. The 3D Fourier transform of the T_2 decay in time results in a blurring function in the image space, as line-broadening and off-resonance artifacts appeared in the area surrounding the vials of high iron concentrations (19). Additionally, with the same noise standard deviation, the relative SNR ratio of SWIFT and SPGR can be estimated by the ratio of Eqs. [5.3] and [5.1] with the consideration of the receiver duty cycles, or explicitly $e^{(TE^{SPGR}-TE^{SWIFT})/T_2}\sqrt{T_{acq}^{SWIFT}/T_{acq}^{SPGR}}$, where T_{acq} is the total acquisition time. Although both sequences had the same acquisition bandwidth, the gaps in the SWIFT pulse introduce a 50% deduction of T_{acq} in this work. Furthermore, only half of the acquired data points were used for image reconstruction in SWIFT, introducing an additional 50% deduction of T_{acq}. Hence, the theoretically estimated ratio of SNRs of SWIFT and SPGR should approximate to $e^{2.95/1.04}\sqrt{0.5\times 0.5}\approx 0.85$, which is slightly higher than the experimental ratio.

Furthermore, with the currently used acquisition bandwidth, the flip angle will be smaller than the expected value when T_2 is extremely short due to significant decay during the pulse. With VFA-SWIFT, this effect would result in greater T_1 error as the SPIO concentration increases. However, depending on the excitation bandwidth and T_2 value, this error may be mitigated (9,20). An excitation performance could be estimated by the coefficient $e^{-1/(bwT_2)}$ (9). The largest effect will occur with vial 7, which has the shortest T_2 (1.04 ms) among all the vials. However, with the RF bandwidth used in this work (62.5 kHz), the coefficient is equal to 0.998, implying that the effect of T_2 could be ignored during the RF transmission of SWIFT in this work. Therefore, despite these potential sources of error, this study clearly demonstrates that the proposed VFA-SWIFT method is valid for iron concentrations up to 7 mM at 7 T, when the flip angles are selected to be between 4° to 36°.

According to Figures 5.4a and 5.4c, T_1 changes proportionally with the iron concentration up to 7 mM. This suggests that iron quantification, from low to high concentrations, can be performed using our proposed method. This is potentially crucial for cell labeling, cell tracking, and hyperthermia treatment of cancer when using SPIO nanoparticles. In addition, due to the unique image contrast, T_1 maps of short T_2* materials (such as cortical bone and teeth) might eventually be utilized in clinical diagnoses.

It was recently reported that the Look-Locker saturation recovery method was combined with SWIFT to measure T_1 of ferrofluid at ultrahigh concentrations (15). Additionally, the UTE sequence is another approach that can shorten the effective TE down to a few microseconds, allowing for T_1 measurement of short T_2* materials (11,12). The difference between SWIFT and UTE is that in SWIFT encoding gradients are always on, whereas in 3D UTE a hard pulse is used to excite signal first and then the gradient is ramped on. Because of this difference, in the presence of short T_2* that is comparable with the ramping time, UTE images are expected to be more blurry (19). Recently, a continuous SWIFT was designed to eliminate the T_2* decay even more than the current version of SWIFT (21). An MR approach with zero echo time was achieved to measure short T_2 samples (e.g., human teeth) and yielded detailed depictions with very good delineation of the mineralized dentin and enamel layers (22). However, comparisons with UTE, zero echo time, and continuous SWIFT on T_1 mapping are beyond the scope of this work.

In conclusion, a VFA-SWIFT sequence was implemented to successfully quantify T_1 of SPIO nanoparticle solutions up to 7 mM. The result was compared with the T_1 values derived by VFA-SPGR and spectroscopic IR approaches. Although the VFA-SPGR sequence failed to estimate the T_1 at high concentrations, both VFA-SWIFT and VFA-SPGR presented good linear

relationships between the relaxation rate R_1 and iron concentrations, with relaxivities of approximately 1.006 and 1.051 s^{-1} mM^{-1} at 7 T, which is close to the spectroscopic IR result of 1.019 s^{-1} mM^{-1}. The proposed method in this work is potentially useful for quantification of low to high concentrations of SPIO nanoparticles for in vivo magnetic resonance imaging applications.

5.7 References

1. Cromer Berman SM, Kshitiz, Wang CJ, Orukari I, Levchenko A, Bulte JW, Walczak P. Cell motility of neural stem cells is reduced after SPIO-labeling, which is mitigated after exocytosis. Magn Reson Med 2013; 69:255–262.
2. Richards JM, Shaw CA, Lang NN, et al. In vivo mononuclear cell tracking using superparamagnetic particles of iron oxide: feasibility and safety in humans. Circ Cardiovasc Imaging 2012; 5:509–517.
3. Ramaswamy S, Schornack PA, Smelko AG, Boronyak SM, Ivanova J, Mayer JE Jr, Sacks MS. Superparamagnetic iron oxide (SPIO) labeling efficiency and subsequent MRI tracking of native cell populations pertinent to pulmonary heart valve tissue engineering studies. NMR Biomed 2012; 25:410–417.
4. Gneveckow U, Jordan A, Scholz R, Bruss V, Waldofner N, Ricke J, Feussner A, Hildebrandt B, Rau B, Wust P. Description and characterization of the novel hyperthermia- and thermoablation-system MFH 300F for clinical magnetic fluid hyperthermia. Med Phys 2004; 31:1444–1451.

5. Zhao Q, Wang L, Cheng R, Mao L, Arnold RD, Howerth EW, Chen ZG, Platt S. Magnetic nanoparticle-based hyperthermia for head & neck cancer in mouse models. Theranostics 2012; 2:113–121.

6. Tyler DJ, Robson MD, Henkelman RM, Young IR, Bydder GM. Magnetic resonance imaging with ultrashort TE (UTE) PULSE sequences: technical considerations. J Magn Reson Imaging 2007; 25:279–289.

7. Robson MD, Gatehouse PD, Bydder M, Bydder GM. Magnetic resonance: an introduction to ultrashort TE (UTE) imaging. J Comput Assist Tomogr 2003; 27:825–846.

8. Idiyatullin D, Corum C, Park JY, Garwood M. Fast and quiet MRI using a swept radiofrequency. J Magn Reson 2006; 181:342–349.

9. Idiyatullin D, Corum C, Moeller S, Garwood M. Gapped pulses for frequency-swept MRI. J Magn Reson 2008; 193:267–273.

10. Goto H, Fujii M, Iwama Y, Aoyama N, Ohno Y, Sugimura K. Magnetic resonance imaging (MRI) of articular cartilage of the knee using ultrashort echo time (uTE) sequences with spiral acquisition. J Med Imag Radiat Oncol 2012; 56:318–323.

11. Zhang LJ, Zhong XD, Wang LY, Chen HW, Wang YA, Yeh JL, Yang L, Mao H. T1 weighted ultrashort echo time method for positive contrast imaging of magnetic nanoparticles and cancer cells bound with the targeted nanoparticles. J Magn Reson Imaging 2011; 33:194–202.

12. Springer F, Steidle G, Martirosian P, Syha R, Claussen CD, Schick F. Rapid assessment of longitudinal relaxation time in materials and tissues with extremely fast signal decay

using UTE sequences and the variable flip angle method. Invest Radiol 2011; 46:610–617.

13. Lehto LJ, Sierra A, Corum CA, Zhang J, Idiyatullin D, Pitkanen A, Garwood M, Grohn O. Detection of calcifications in vivo and ex vivo after brain injury in rat using SWIFT. Neuroimage 2012; 61:761–772.

14. Zhou R, Idiyatullin D, Moeller S, Corum C, Zhang H, Qiao H, Zhong J, Garwood M. SWIFT detection of SPIO-labeled stem cells grafted in the myocardium. Magn Reson Med 2010; 63:1154–1161.

15. Chamberlain R, Etheridge M, Idiyatullin D, Corum C, Bischof J, Garwood M. Measuring T1 in the presence of very high iron concentrations with SWIFT. In Proceedings of the 20th Annual Meeting of ISMRM, Melbourne, Australia, 2012. p. 4368.

16. Haacke EM. Magnetic resonance imaging: physical principles and sequence design. New York: Wiley; 1999. xxvii, 914 pp.

17. Treier R, Steingoetter A, Fried M, Schwizer W, Boesiger P. Optimized and combined T1 and B1 mapping technique for fast and accurate T1 quantification in contrast-enhanced abdominal MRI. Magn Reson Med 2007; 57:568–576.

18. Jackson JI, Meyer CH, Nishimura DG, Macovski A. Selection of a convolution function for fourier inversion using gridding. IEEE Trans Med Imaging 1991; 10:473–478.

19. Rahmer J, Bornert P, Groen J, Bos C. Three-dimensional radial ultrashort echo-time imaging with T2 adapted sampling. Magn Reson Med 2006; 55:1075–1082.

20. Larson PE, Gurney PT, Nayak K, Gold GE, Pauly JM, Nishimura DG. Designing long T2 suppression pulses for ultrashort echo time imaging. Magn Reson Med 2006; 56:94–103.

21. Idiyatullin D, Suddarth S, Corum CA, Adriany G, Garwood M. Continuous SWIFT. J Magn Reson 2012; 220:26–31.

22. Weiger M, Pruessmann KP, Bracher AK, Kohler S, Lehmann V, Wolfram U, Hennel F, Rasche V. High-resolution ZTE imaging of human teeth. NMR Biomed 2012; 25:1144–1151.

Table

Table 5.1: Estimated T_1 values of the vials

Vial Numbers	Concentrations [mM]	Estimated T_1 Values [ms]		
		VFA-SWIFT	VFA-SPGR	IR
1	1	733.2 ± 29	679.9 ± 26	714.7
2	2	446.7 ± 23	412.4 ± 24	435.4
3	3	296.5 ± 18	289.6 ± 17	306.7
4	4	212.9 ± 12	233.8 ± 18	242.1
5	5	183.1 ± 15	167.8 ± 21	183.2
6	6	153.1 ± 13	−	152.2
7	7	137.8 ± 14	−	132.9

Table 5.1. Iron concentrations (1 mM Fe is approximately 0.056 mg Fe/mL) of the different vials are listed in the second column. The T_1 values estimated by the VFA-SWIFT, VFA-SPGR and spectroscopic IR based methods are presented in the last three columns.

Figures

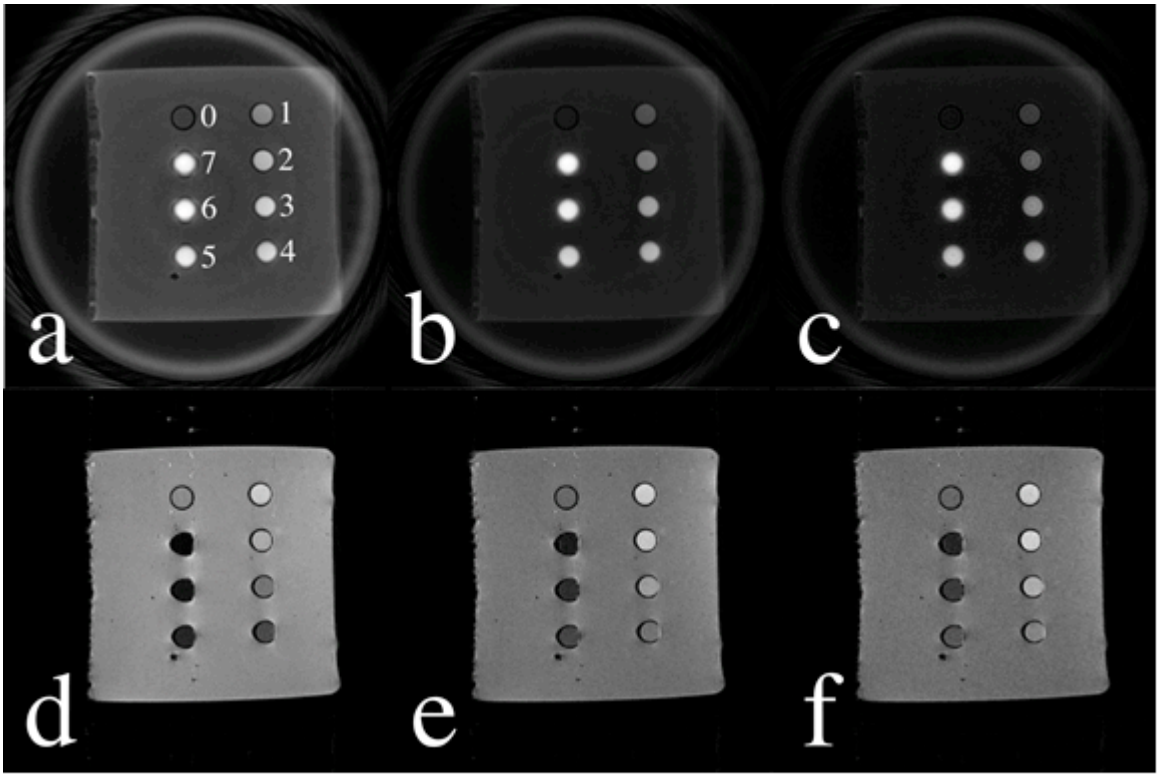

Figure 5.1. SWIFT and SPGR images acquired at flip angles of 10° (1st column), 20° (2nd column), and 30° (3rd column) are illustrated in the first and second row, respectively. In Figure 1(a), vials with purified water and different iron concentrations are labeled from 0 to 7 (see the Table 5.1 for details).

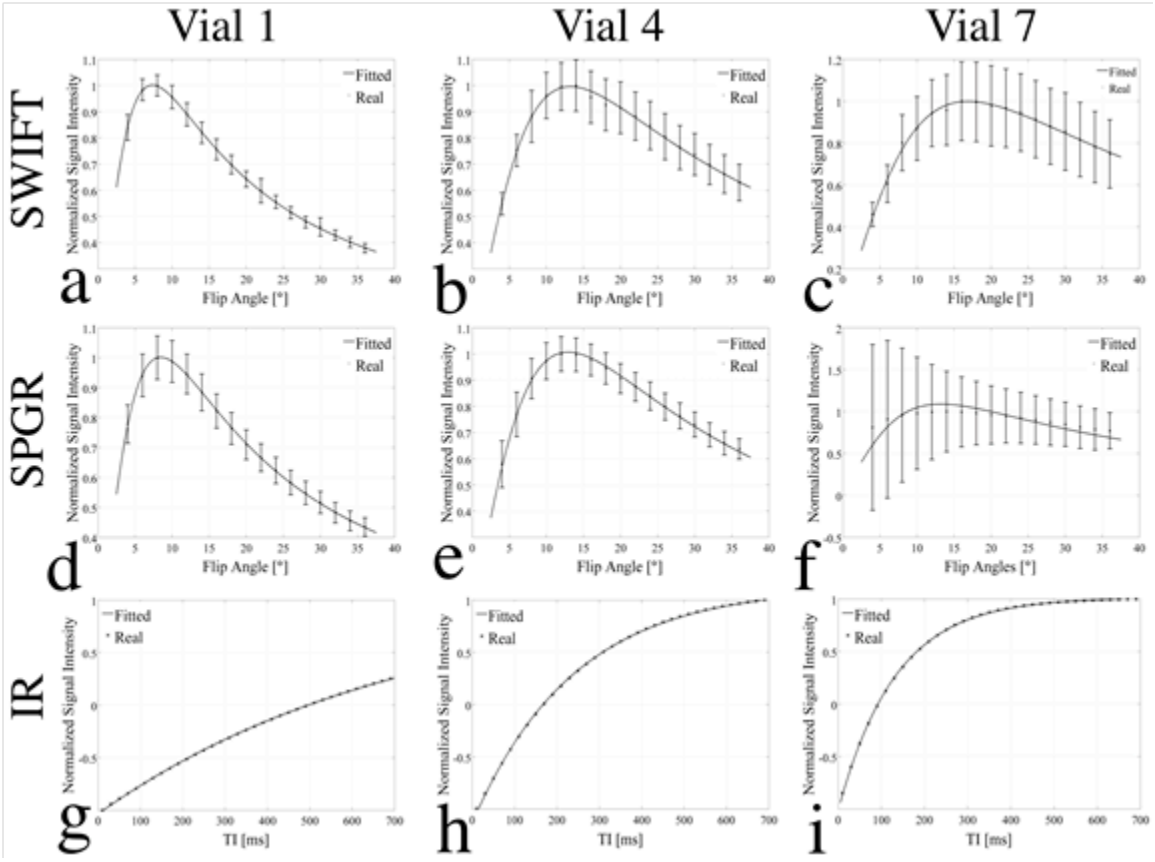

Figure 5.2. Plots of normalized signal intensity (averaged within each vial) of vials 1 (1st column), 4 (2nd column) and 7 (3rd column), representing a low, medium, and high concentration, as a function of flip angles for SWIFT (1st row) and SPGR (2nd row), and of inverse recovery decays (TI) for spectroscopic IR method (3rd row). For the SWIFT and SPGR studies, the flip angle was fitted to the normalized signal using Eqs. [5.1-5.3]. For the spectroscopic IR method, TI was fitted to the normalized signal using Eq. [5.4].

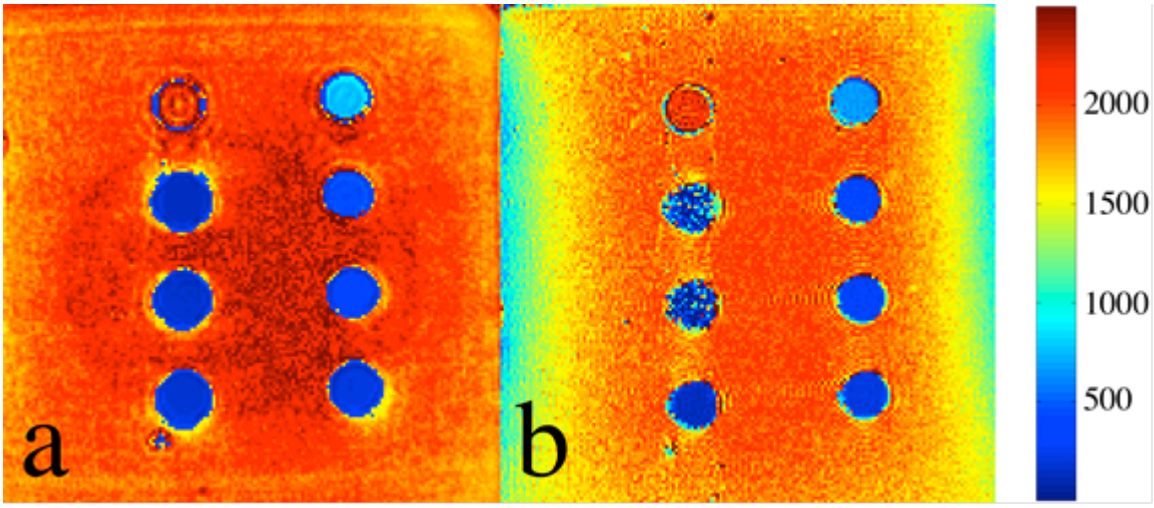

Figure 5.3. T_1 maps of the SPIO phantom estimated by using the (a) VFA-SWIFT and (b) VFA-SPGR based approaches. The unit of the color bar is in [ms].

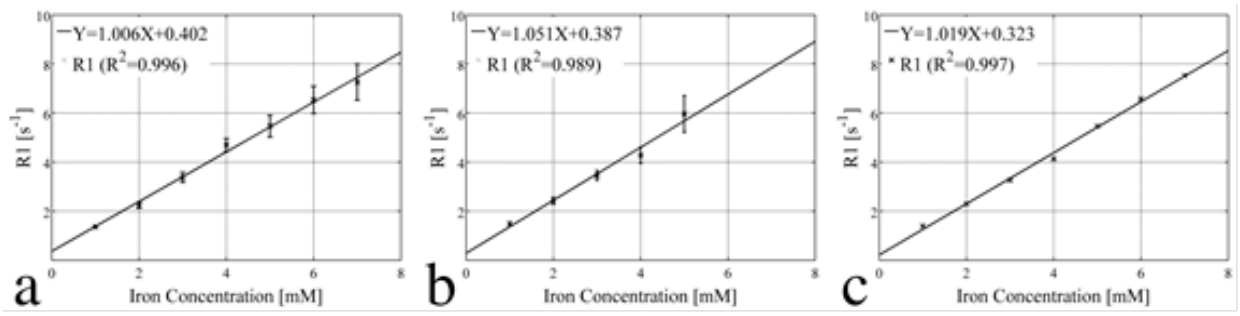

Figure 5.4. Concentrations of the different vials are linearly fitted to their R_1 values estimated by the (a) VFA-SWIFT, (b) VFA-SPGR and (c) spectroscopic IR based methods. Notice that data from vials 6 and 7 were not included in the fitting due to the signal loss caused by fast T_2^* decay. The r_1 values (slope) of the fits in (a), (b) and (c) are equal to 1.006, 1.051, and 1.019 s^{-1} mM^{-1}. The R^2 values of the three fits are equal to 0.996, 0.989 and 0.997.

CHAPTER 6

CONCLUSIONS

MR imaging of short T2 (in the scale of a few or tens of microseconds) materials remains a great challenge when traditional pulse sequences are applied. The short T_2 materials cover a variety of matter, such as T2 contrast agents or tissues like cortical bone, teeth, or tendon, etc. As an important category of T_2 contrast agents, iron oxide nanoparticles have been used for tumor cell targeting and labeling in many published works, as well as in the present work. Similarly, studies of cortical bone are attracting more attentions from scientists and clinicians, resulting in increasing numbers of the related publications, due to rapidly increasing bone diseases caused by aging, obesity, and etc. To overcome these challenges, new approaches in magnetic resonance imaging have been proposed in this dissertation to conduct qualitative and quantitative studies of iron oxide nanoparticles and cortical bone.

6.1 Qualitative studies

Chapter 2 aimed to use the SWIFT sequence to suppress long T_2 tissues and fat to improve the detection specificity of iron oxide nanoparticles delivered to tumors. The Bloch equation simulations provided a theoretical support for designing the saturation RF pulses. Specifically, a shorter Gaussian pulse is more capable of flipping short T_2 spins to the transverse plane. Therefore, in order to successfully suppress tissues, like long T2 tumor tissue, muscle, and fat, different pulse lengths (ranging from 2ms to 32ms) have been tested in the in vivo and ex vivo MR experiments. The experimental results showed that a shorter Gaussian pulse generated a

better suppression of long T_2 signal as well as showed a better tolerance of magnetic field inhomogeneity, which was consistent with the simulations. However, a short Gaussian pulse also resulted in lower SNR and CNR values, according to the images of the ex vivo experiments. Following the MR experiments, Prussian blue staining and murine β_3 staining also confirmed success of the delivery of the iron oxide nanoparticles into the tumors. In general, this work demonstrated a feasibility to implement the SWIFT sequence with long T_2 suppression to image short T_2 materials, such as iron oxide nanoparticles, with improved detection specificity. However, this work can be improved in the future. For example, the number of mice involved in the experiments could be increased for better statistical significance.

In order to image free water, bound water and fat in a bone, Chapter 3 presented a preliminary study of a piece of swine humerus bone using both the SWIFT sequence and the conventional FSE sequence. Because of the chemical shift between water and fat, there were artifacts associated with the acquired images, such as image blurring, when imaging water and fat components simultaneously. Therefore, water and fat saturations had to be implemented in order to improve the image quality. For the fresh humerus bone, free water components were clearly illustrated in the porous structure of the cortical bone and the canals of bone marrow, with the help of fat suppression. Compared with the FSE sequence, the SWIFT sequence allowed a much shorter echo time, so that structures which was not detected in the FSE images, became clearly visible in the SWIFT images. With water suppression, fat was also observed in the porous structure and the bone marrow. In the fresh bone, bound water was shown as relatively low signal intensity. After the humerus bone was dehydrated, only bound water and fat were supposed to remain in the cortical bone. Both the SWIFT and FSE sequences were able to visualize fat in the porous structure, but only could the SWIFT sequence successfully acquire the

signal from bound water. This preliminary study showed that distributions of water and fat components have been localized in the humerus bone. The results suggested that the SWIFT sequence would be more suitable to image short T_2 materials for bone scans, compared to the FSE sequence.

6.2 Quantitative studies

Following the qualitative studies, additional two works were conducted for quantitative imaging of the iron oxide nanoparticles. In Chapter 4, iron oxide nanoparticles were used to label C6 glioma cells grafted in mice. A new approach was proposed to calculate concentration and susceptibility of iron oxide nanoparticles from MR phase gradient images. To verify and demonstrate this novel method, a phantom experiment consisting of four different concentrations of iron oxide nanoparticle suspensions were conducted using a 3 T MR scanner. The result showed that the concentration of iron oxide nanoparticles was linearly proportional to their susceptibility. The statistical analysis also indicated the theoretical calculations were consistent with the experimental data. For the in vivo experiment, the susceptibilities of the iron oxide nanoparticles, which were used for cell labeling, were estimated from the MR phase gradient images, and then converted into the concentrations of the oxide nanoparticles, using the linear relationship estimated in the phantom experiment between the two quantities. Due to several factors, such as possible cell migrations and aggregations of iron oxide nanoparticles, the estimated concentrations fluctuated among tested mice, but the result of statistical analysis was still fairly stable.

A novel method proposed in Chapter 5 was designed to quantify highly concentrated aqueous iron oxide nanoparticle suspensions, which was a very challenging problem in MRI. This work

consisted of both MR imaging experiment and an inversion recovery spectroscopic experiment as a gold standard. For the MRI experiment, the SWIFT and SPGR sequences were implemented to scan the phantom with multiple flip angles. Because the MR scans were conducted at a steady state, the signal intensity was a function of flip angles. Hence, the T_1 values of the iron oxide nanoparticle suspensions could be derived according to the resulted signal variation at variable flip angles. However, since the echo time was too long for acquisition of fast-decaying signals, the SPGR sequence was unable to quantify T_1 for highly concentrated iron oxide nanoparticle suspensions. On the other hand, the SWIFT sequence was of the advantage of utilizing very short echo time, so the T_1 values of all of the suspensions have been quantified, and results were consistent with that of the inversion recovery spectroscopic measurements. Based on the estimated T_1 values, the relaxation rate ($1/T_1$) was found to be linearly proportional to the concentration, and the slope is the intrinsic property of the iron oxide nanoparticles, namely relaxivity.

Although both of the two chapters focused on quantification of iron oxide nanoparticles, they have different advantages and drawbacks. First, the phase gradient mapping method makes use of the gradient echo sequence, which is available for clinical applications on all of the commercial scanners, while the T_1 mapping method makes use of the SWIFT sequence, which is currently not available on most of the clinical scanners; Second, the phase gradient mapping method may not be suitable for quantification of highly concentrated iron oxide nanoparticle solutions, since the strong dipole field, which is induced by the iron oxide nanoparticles, generates image artifacts and distorts the MRI images. In contrast, implementation of the T_1 mapping method is based on the SWIFT sequence, and it has been demonstrated to be able to quantify iron oxide nanoparticles up to 7 mM. However, the T_1 mapping method is sensitive to

B_1 field inhomogeneity, since inaccurate flip angles will result in errors for T_1 mapping without an appropriate calibration process. Lastly, the phase gradient mapping method only needs data acquisition with a single TE, while the T_1 mapping method usually involves multiple scans with variable flip angles, which takes a longer scan time and is potentially more sensitive to the motion of the patient in between these scans.

6.3 Summary

This dissertation has been concentrated on improving magnetic resonance imaging of short T_2 materials for both qualitative and quantitative studies. The results presented in these studies were demonstrated and verified through various approaches: simulations, phantom experiments, in vivo and ex vivo MRI experiments, and spectroscopic experiments. However, the author also recognized the potential drawbacks and limitations in this dissertation, and aims to improve them in future works. For example, although it is important and necessary, the SWIFT sequence has not been well compared with the UTE sequences, to the best of the author's knowledge. Because the development of both pulse sequences is highly dependent on the development of MRI devices, such as the transmission-reception switch and gradient coils, so they are still relatively new and not implemented as widely as some conventional pulse sequences, such as spin echo and gradient echo based pulse sequences. Additionally, the performance of the methods proposed here is also dependent on many factors, such as shimming, gradient coils, and etc. Therefore, for a better performance it is necessary to involve the most cutting-edge technologies in future work.

In summary, magnetic resonance imaging of short T_2 materials is an important yet difficult topic. Overcoming of these challenges will promote our understanding of science, and allow us

to perform more accurate diagnoses of diseases, design more efficient treatments, and make our knowledge to serve people better.